ABSTRACT

Title of dissertation: BARELY IMPLICIT CORRECTION ALGORITHM FOR LOW-MACH-NUMBER FLOWS AND ITS APPLICATION TO VORTEX BREAKDOWN UNDERGOING HEAT ADDITION AND EXTRACTION

Xiao Zhang
Doctor of Philosophy, 2020

Dissertation directed by: Professor Elaine S. Oran
Department of Aerospace Engineering

This thesis presents a new Barely Implicit Correction (BIC) algorithm combined with a modified flux-corrected transport (FCT) algorithm for the simulation of three-dimensional (3D), low-Mach-number flows and then proceeds to apply it to the study of vortex breakdown undergoing heat addition and heat extraction. This new algorithm is based on the original, introduced by a prior work in 1987, which was a solution procedure including an explicit predictor step to solve the convective portion of the Navier-Stokes equations and an implicit corrector step to remove the acoustic limit on the integration time-step. The explicit predictor uses the flux-corrected transport (FCT) algorithm while the implicit corrector solves an elliptic equation for a pressure correction to equilibrate acoustic waves. This thesis introduces a procedure for stabilizing and implementing FCT for 3D flows and extends BIC for 3D with physical diffusion processes. A new filter is introduced to further stabilize the algorithm and the solution procedure is clarified for the inclusion of the

diffusion fluxes. The new BIC-FCT algorithm is examined in four test problems with successively increased difficulty. The test problems culminate with calculations of vortex breakdown in 3D swirling flows. All the test problems demonstrate that the algorithm is able to predict accurate and robust solutions using time steps varying from near the explicit stability limit to tens and hundreds of times larger. Excellent agreement is also obtained when compared with results from other algorithms. The algorithm is then used to study how vortex breakdown is affected when heat is extracted from or added to the flow. Two heat release rates are applied to a flow with a bubble mode of breakdown upstream and double-helix mode downstream. The simulations show that heat release causes the double-helix structure to become narrower. With more heat release, the double-helix mode transitions to a columnar vortex. In addition, a lower heat extraction rate causes the columnar vortex to first transition to a spiral mode and then to a double-helix mode. With a higher heat extraction rate, the columnar vortex transitions to a double-helix mode, bypassing the spiral mode. Further investigation show that the density gradient formed by heat addition and extraction is the dominant effect in the transitions. The transition is promoted by changes in viscosity due to temperature changes from heat addition and extraction. The new algorithm presented in this thesis provides a new way to calculate low-Mach-number flows. Such vortex breakdown simulations with heat changes serve as a base for understanding the dynamics of a precessing vortex core in swirl combustors and other vortex flows with changes in heat input.

BARELY IMPLICIT CORRECTION ALGORITHM FOR LOW-MACH-NUMBER FLOWS AND ITS APPLICATION TO VORTEX BREAKDOWN UNDERGOING HEAT ADDITION AND EXTRACTION

by

Xiao Zhang

Dissertation submitted to the Faculty of the Graduate School of the
University of Maryland, College Park in partial fulfillment
of the requirements for the degree of
Doctor of Philosophy
2020

Advisory Committee:
Professor Elaine S. Oran, Chair/Advisor
Professor Johan Larsson, Dean's Representative
Professor Michael J. Gollner
Professor James D. Baeder
Professor Norman M. Wereley
Research Associate Professor Carolyn R. Kaplan

Acknowledgments

First, I would like to express my sincere gratitude to my advisor, Dr. Elaine S. Oran, for the continuous support, motivation, and expertise for my graduate studies and for allowing me to grow as a better researcher throughout these four years. Her passion and enthusiasm for research were motivational for me, especially during the difficult times in the Ph. D pursuit.

I would like to thank my committee members (listed in alphabetical order by last name) Dr. James D. Baeder, Dr. Michael J. Gollner, Dr. Carolyn R. Kaplan, Dr. Johan Larsson, and Dr. Norman M. Wereley, for their encouragement and insightful comments which enriched my research from many perspectives. I thank Dr. Baeder for his excellent course in computational fluid dynamics, which gave me the knowledge to solve some of my most difficult challenges in the algorithm development. I thank Dr. Gollner for his detailed course on flames which built my foundation to understand the physics of my research and explore new ideas. I am highly appreciative of the many discussions that we had about the physics of vortex breakdown and fire whirls. I am truly grateful to Dr. Kaplan who was always available to discuss the problems I encountered in the algorithms, simulations, or anything else. I thank Dr. Larrson for his insightful suggestions which led to a clearer understanding of my results. I thank Dr. Wereley for his help in obtaining the computer resources which were critical to the work performed in my thesis.

I am appreciative of the many people who have helped me solve critical problems and provided helpful suggestions throughout my research. Dr. Ryan W. Houim

spent countless hours teaching me how to code in FORTRAN and helping debug the code. I am deeply appreciative of his willingness to help, his invaluable suggestions, and his course on combustion which proved to be extremely helpful during the past four years. Dr. C. Richard DeVore's guidance and suggestions helped solve the stability issues in the algorithms used in this work. Discussions with Dr. Huahua Xiao led to new ideas in my research. I thank Dr. Jay P. Boris for our discussions on the design of the algorithms used in this work.

I am grateful for the many friends that I made during my time here as a graduate student and for all of their help. Praveen Honhar's deep insight and interesting humor helped solve many of my most challenging problems. Utkarsh Aggarwal provided guidance and help when I first joined the group and also during the development of the code. Sriram Hariharan was always around to discuss the physics, results, and to have fun at the many conferences we attended together. I thank Dr. Paul M. Anderson for our insightful discussions on my research. I thank Dr. Shuyue Lai, Dr. Weilin Zheng, Rui Xu, Grant Dube, Jason Burr, and Alvin Pee for their friendship and guidance. Finally, I thank my labmate, friend, and husband, Joseph Chung, who was with me from the start and to the end of this work. He was with me through the most difficult times and shared the most joyous moments we had together.

I am deeply thankful to my mother, father, and others in my family for their guidance through my career and unending support through my life. I would not have made it this far without their loving help and support.

I am thankful for the funding given by the Army Research Office (grant

W911NF1710524) and by the National Science Foundation under award CBET 1839510. Computations were performed using the Deepthought2 HPC cluster here at the University of Maryland and Stampede2 at the Texas Advanced Computing Center.

Table of Contents

[1] This section is a slightly modified version of what has been published in [1] and has been reproduced here with the permission of the copyright holder.

List of Tables

List of Figures

List of Abbreviations

BIC	Barely Implicit Correction
FCT	Flux-Corrected Transport
CFL	Courant-Friedrichs-Lewy
PVC	Precessing Vortex Core
NS	Navier Stokes
DNS	Direct Numerical Simulation
QCA	Quasi-Cylindrical Approximation
CIVB	Combustion Induced Vortex Breakdown

Chapter 1: Introduction

1.1 Background and Motivation

1.1.1 Blue Whirl

The recent discovery of a new flame, the blue whirl, has garnered significant interest from both academics and the media since its discovery in 2016. The blue whirl, which is shown in Fig. 1.1, appears as a stable, quiet, strongly swirling hydrocarbon flame sitting on a water surface. The blue burning state, which implies nearly soot-free combustion of heavy hydrocarbon liquid fuels, indicates its potential of contributing to highly efficient, low-emission combustion with no harm to humans or to the natural environment. Despite the interest, its fundamental structure has remained unknown due to limitations in experimental diagnostics and simulation capabilities. A work [3] parallel to this thesis has revealed the flame and flow structure of the blue whirl using the algorithms described in this thesis. This work focuses on the algorithm development and a fundamental study on the transitional processes that may occur during the blue whirl formation.

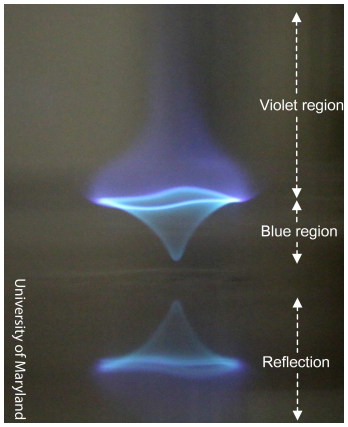

Figure 1.1: Photograph of a blue whirl burning n-heptane stably on a water surface. Figure reprinted from [4]

The blue whirl evolved spontaneously during experimental studies of fire whirls burning liquid hydrocarbon fuels on a water surface [4]. A fire whirl is a strongly swirling flow comprised of a standing vortex that combines wind and fire. Fire whirls can exist in all sizes, ranging from centimeters high to kilometers high [5], and in environments ranging from controlled laboratory experiments to urban and wildland areas [6, 7, 8]. The initial experiments in [4] were designed to study the potential of using controlled fire whirls for practical purposes, for example oil-spill remediation. In the initial experiments [4], the system undergoes a transition naturally from a liquid hydrocarbon pool fire to a fire whirl, and then from a fire whirl to a blue whirl, as shown in Fig. 1.2.

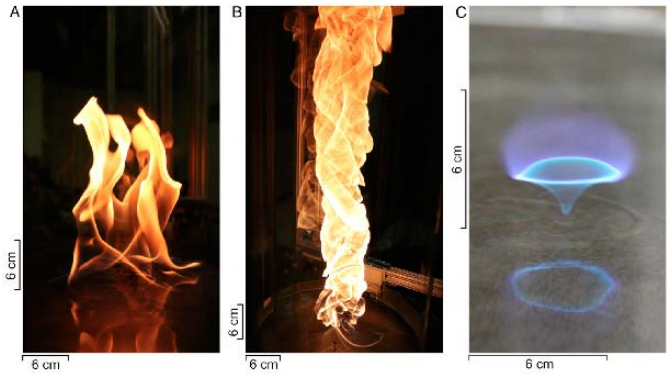

Figure 1.2: Evolution from a pool fire to a blue whirl over water in a whirl generator. (A) Pool fire forms following ignition. (B) Canonical fire whirl develops subsequent to the pool fire. (C) Previously unobserved laminar blue whirl evolves from the yellow fire whirl. The vertical scale marked on the side of each image starts at the water surface. Figure taken from [4]

Although the blue whirl seems to show a way to achieve clean combustion, many questions need to be answered to determine whether it can be used for practical purposes. For example, what is the flame structure and dynamics of the blue whirl? Can it scale to larger sizes? Can it be produced at different Mach numbers? Can multiple blue whirls be made and work together? These questions are not easily answered in experiments, and probably can be addressed by simulations.

The first objective of this work is to build a numerical tool that serves as a fundamental base for the numerical study of blue whirl. The numerical tool should be able to, in the short term, help answer the most fundamental question of the blue whirl, that is its flow and flame structure. In the long run, we also want to study the scalability of the blue whirl. Therefore, the algorithm should also work for both low and high Mach numbers. Since the blue whirl is inherently a three-dimensional (3D) problem and the flow develops over many seconds or even

minutes of physical time, the numerical tool needs to be computationally efficient to perform parametric studies with large matrices. Also, the flow is turbulent which covers a range of scales, and the vortex field may have strong gradients. Resolving these features with affordable resources requires the algorithm to be low dissipation. All of these questions lead to algorithm development for, but not limited to, the blue-whirl study. This is the first motivation of the present work.

1.1.2 Relationship between Vortex Breakdown and Heat Release

In the experiments on the blue whirl [4, 9], glowing streaks of remnant soot created during the transition process help visualize the flow structure and the change in flame shape. The helical structure as shown in Fig. 1.3a is observed at an early stage during the transition from a yellow fire whirl to a blue whirl. The recirculating soot patterns shown in Fig. 1.3b suggests a bubble-like structure at a later time during the transition. These features suggest that the flow undergoes vortex breakdown, which is an abrupt and drastic change of flow structure that occurs in swirling flows.

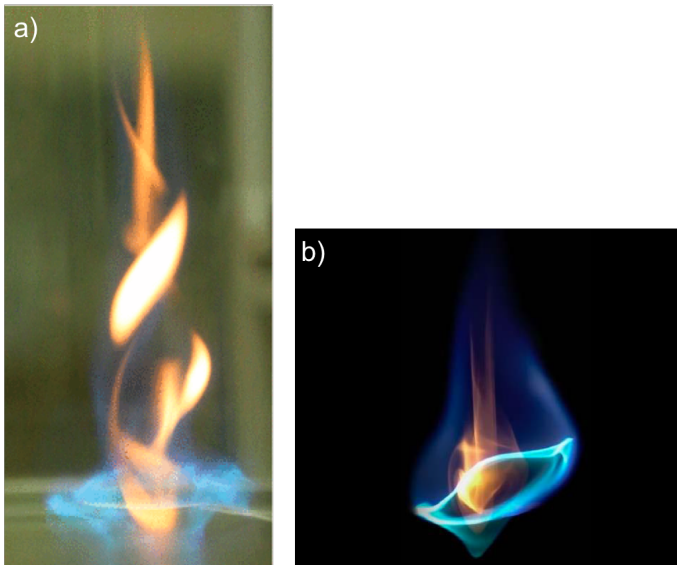

Figure 1.3: Transitional stages during the evolution process from a fire whirl to a blue whirl. (A) A cup-like blue whirling flame on water holds a yellow whirling flame with a helical structure. Figure taken from [4]. (B) Recirculating soot patterns inside the blue whirl show a bubble-like structure. Figure taken from [9].

Vortex breakdown occurs in swirling jet flows when disturbances in the flow field cause the columnar vortex to suddenly collapse and expand into a highly fluctuating structure. The axial velocity decreases drastically with a stagnation point forming on the centerline of the jet axis and a recirculation zone around it. This new state arising due to vortex breakdown has a strong effect on the ensuing fluid dynamics.

Vortex breakdown is categorized into different types based on distinctive flow structures, which includes the double-helix mode suggested in Fig. 1.3a and the bubble mode suggested in Fig. 1.3b. Despite numerous theoretical, numerical and experimental research over the past few decades, the mechanism that leads to vortex breakdown and the mechanism that causes the transition between different modes

are still not well understood. In the blue-whirl experiment, the transition from a fire whirl to a blue whirl suggests change of modes of vortex breakdown, and indicates heat release from combustion processes could play an important role in the mode change. Therefore, understanding the relationship between vortex breakdown and the heat release effect is important in understanding the transition from a fire whirl to a blue whirl. Furthermore, understanding this relationship can help answer whether we can bypass the dangerous fire whirl, sooty transitional stage, and create the blue whirl in a direct, controlled way. The second motivation of the present work is to use the newly developed algorithm to study the relationship between vortex breakdown and heat inputs.

Understanding the relationship between vortex breakdown and thermal effects is not only critical to the blue whirl study, but also beneficial to many other applications related to the vortex breakdown phenomenon. Vortex breakdown was initially discussed for aeronautical flows and is of significance in aeronautical applications (Fig. 1.4a), as it can have both beneficial and detrimental effect on flight. When leading-edge vortices shedding from a delta wing undergo vortex breakdown, the sudden and drastic change in the vortex structure can cause performance loss and dangerous vibrations [10]. On the other hand, vortex breakdown in trailing wing-tip vortices is desirable as it weakens the vortices that are hazardous to smaller aircraft in dense air traffic [10]. Therefore, the ability to control vortex breakdown in aeronautical applications is important. Understanding the relationship between vortex breakdown and thermal effects can, therefore, suggest ways of controlling vortex breakdown in aeronautical applications.

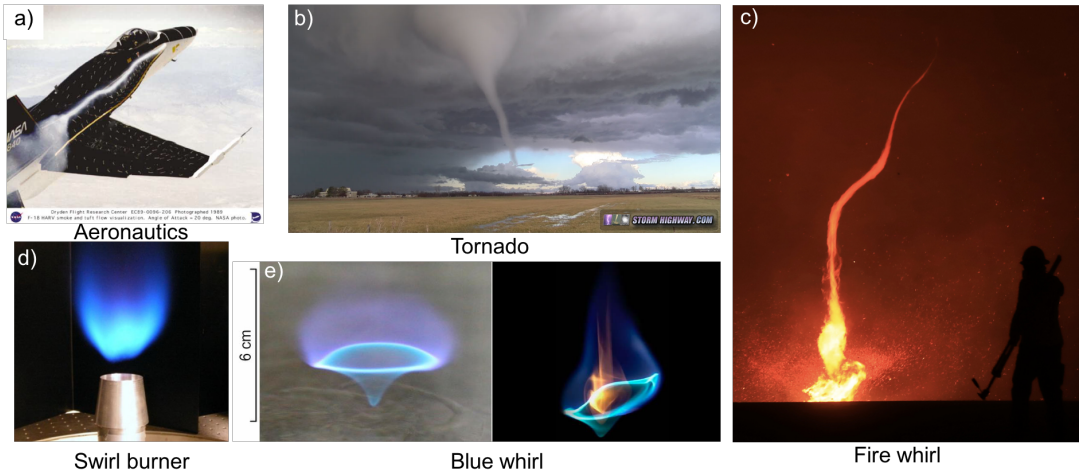

Figure 1.4: Vortex breakdown in different flows. (A) Vortex breakdown around NASA's F-18 High Angle of Attack Research Vehicle (HARV). Credits: NASA Photo. (B) Vortex breakdown in a tornado. Photo credits: Dan Robinson. (C) Vortex breakdown in a fire whirl. Proto credits: Kent Porter. (D) Lifted flame of a swirl burner. Figure taken from [11]. (E) Blue whirl. Figure taken from [4, 9].

Vortex breakdown has also been observed in nature, for example in tornadoes (Fig. 1.4b) and fire whirls (Fig. 1.4c). Fire whirls can be extremely dangerous in wildland areas as it can be kilometers tall, and contain wind speeds over 200 km/h. Forcing fire whirls to transition to the bubble mode of vortex breakdown may help reduce its size and therefore reduce its impact on the environment and people. Understanding the relationship between vortex breakdown and thermal effects may help firefighters better control and extinguish fire whirls.

Vortex breakdown is also used in combustion systems where the recirculation zone of vortex breakdown can be used to stabilize the flame and enhance fuel and air mixing, thereby reducing pollution and increasing combustion efficiency [12, 13]. The applications include power station burners, gas turbine combustors, and internal combustion engines. One example of the swirl combustor is shown in Fig. 1.4d.

Despite the benefits gained from vortex breakdown, stability is an associated problem in swirl combustors at certain operation conditions [14, 15, 16]. The oscillatory flow structures that result from vortex breakdown could cause acoustic excitation of the flame from sound waves. If the fluctuations of heat release resonate with any geometrical components of the combustor, self-excited instabilities can be triggered and cause severe damage. Despite numerous experimental and numerical investigations, how combustion affects the oscillatory mode of vortex breakdown is still not clear. A fundamental study on the relationship between vortex breakdown and heat release effect can help understand how to avoid combustion instabilities and control oscillatory modes in swirl combustors.

1.2 Technical Objectives

The technical objectives of this work were as follows:

1. Develop a numerical algorithm that serves as a base for the numerical study of the blue whirl.

   (a) Develop an algorithm which can solve 3D, unsteady, Navier-Stokes equations in the low-Mach number regime.

   (b) Using this algorithm, build a computational fluid dynamics code which has capabilities of parallelization and mesh refinement.

   (c) Test the code and algorithm for steady and unsteady mutidimensional swirling flows with successively increasing difficulty.

2. Apply the developed algorithm to perform a fundamental study of vortex breakdown undergoing heat addition and extraction.

   (a) "Find" a numerical configuration that can produce different modes of vortex breakdown with well-defined controlling parameters and without the influence of a confining geometry.

   (b) Using numerical simulations, apply heat release and heat extraction to different modes of vortex breakdown and assess how the modes are affected.

1.3 Scope of Present Work

Part one of this work focuses on developing an algorithm which is capable of computing low-Mach-number vortex flows such as seen in the blue whirl. The flux-corrected transport (FCT) algorithm is selected as the base fluid solver for the compressible 3D Navier-Stokes (NS) equations due to many of its desired features, for example the low numerical dissipation and monotonicity. The version of FCT used in this work was initially designed for one-dimensional problems[17]. Extension to multidimensional simulations were introduced in later work [18, 19]. Simulations based on this version of FCT, however, were only reported in two dimensions (2D) in previous work [19]. In this work, while extending this FCT to 3D, unexpected numerical instability was encountered initially. To solve this issue, a Fourier stability analysis is first performed in this work for both 2D and 3D FCT, which revealed an inherent instability in 3D. One method for stabilizing FCT in 3D is then introduced

and demonstrated.

After stabilizing FCT in 3D, a low-Mach number correction, the barely implicit correction (BIC), is then applied to FCT. Although FCT is well tested for computing high-speed, compressible flows, explicitly integrating the NS equations using FCT for low-Mach number flows can be prohibitively expensive as the time steps are mainly restricted by the sound speed. BIC removes the sound-speed limit by solving the governing equations at a large time step determined by the fluid velocity (predictor step), and then applying a pressure correction that effectively equilibrates the acoustic waves. The BIC algorithm was originally introduced in [20]. When it was used for one-dimensional (1D) and 2D problems [21, 22], there were numerical issues such as growing pressure oscillations that had to be damped. Suggestions and methods to address these issues were provided in a recent document of BIC [23], but some ambiguity and inconsistency in the document introduced difficulties in solving the numerical issues completely. In this work, we fix the inconsistency in the previous BIC document and clarify the path towards the solution by introducing a new procedure. We describe how to apply BIC to multidimensional viscous flows and present the integration procedure. We also introduce a new filter to further stabilize the algorithm. The new BIC-FCT and explicit FCT algorithm are then both implemented in 2D and 3D based on the BoxLib adaptive mesh refinement library. The code is parallelized with shared (OpenMP) and distributed memory (MPI).

The performance of the algorithm and code was then examined for four test problems with successively increasing difficulty. First, a sinusoidal density profile

was convected in 1D and the solution was compared against an exact solution to assess BIC's spatial and temporal order of convergence. A 2D lid-driven cavity flow was simulated to demonstrate the ability of BIC on solving steady-state swirling flows. The results are compared with a numerical solution using a vorticity-stream-function formulation of the incompressible NS equations [24]. A 2D doubly periodic shear layer flow was simulated to examine the algorithm on solving a transient flow with strong vorticity gradients. The results are qualitatively compared with a Numerical Acoustic Relaxation (NAR) method [25] and quantatively compared with a pseudospectral method [26]. Finally, vortex breakdown in 3D swirling flows were used to further test the stability and performance of the new BIC algorithm. The results are qualitatively comparable with a previous direc numerical simulation [27].

Part two of this work focuses on using the newly developed algorithm and code to perform a fundamental study of sensitivity of vortex breakdown to thermal effects. The "Grabowski vortex" profile [28] was selected as the numerical configuration to simulate vortex breakdown as it has well-defined controlling parameters and no geometrical confinement. Both heat release and heat extraction effects were studied in this work by introducing or extracting energy through a source term in the energy conservation equation. Both heat release and heat extraction effects were introduced separately in a defined region into flow fields which already have fully developed vortex breakdown. For the heat release cases, a baseline flow with a bubble mode upstream and a double-helix mode downstream is calculated. For the heat extraction cases, a baseline flow with a bubble mode upstream and a columnar

vortex downstream is calculated. Two heat release rates and two heat extraction rates are tested respectively. The effect of viscosity change due to its temperature dependence on the mode change was examined.

In this dissertation, the literature is reviewed in Chapter 2 on current research about the blue whirl, vortex breakdown, and low-Mach-number algorithms. In Chapter 3, the flux-corrected transport algorithm is described and Fourier stability analysis for both 2D and 3D FCT is included. A new method for stabilizing FCT in 3D is introduced. Chapter 4 describes the original BIC procedure and introduces a new solution procedure for multidimensional flows with diffusion processes. Chapter 5 presents 2D and 3D test cases for the new BIC-FCT algorithm. Chapter 6 studies the sensitivity of vortex breakdown to thermal effects using BIC-FCT. Finally, Chapter 7 summarizes the findings and contribution of this work.

Chapter 2: Literature Review

This chapter first reviews the prior work performed on the blue whirl and then reviews vortex breakdown in both nonreactive and reactive systems. To study the blue whirl and vortex breakdown, a low-Mach-number algorithm which is computationally efficient for 3D flows is needed. A review of low-Mach-number algorithms is included at the end of this chapter.

2.1 Blue Whirl

The first observation of blue whirl is originally published in [4]. The blue whirl evolves from an initial large yellow fire whirl to a small blue spinning flame. The blue whirl has three distinct regions, which are the lower blue cone, a bright blue ring at the edge, and a purple haze region on the top. Hariharan et al. [9, 29, 30] measured the thermal structure of the blue whirl using thermocouples and thin-filament pyrometry, which showed that the blue whirl has a peak temperatures of 2000 K in the purple haze region, a higher temperature than that of a fire whirl. Hariharan et al. [30] also found that blue whirl only forms on a smooth unobstructed surface. Their OH^* chemiluminescence measurements indicates that the blue ring is the region that has the maximum combustion. Hu et al. [31] constructed a map

of circulation level and fuel consumption rates at which the blue whirl forms, which shows distinctive regions in the parameter map the between blue whirl and the fire whirl. All of these experiments above used a fixed-frame self-entraining apparatus. In a recent experimental study [32], a set of vertically oriented thin rectangular vanes were placed at an adjustable angle to control the level of air circulation entrained by the pool fire. As the level of air circulation is increased, the flame recedes from the edge of the liquid-fuel pool and eventually detaches and lifts up into the blue whirl. So far, the experimental measurements provided considerable information about the final state of the blue whirl. The fundamental flame and flow structure of the blue whirl and the transition dynamics are, however, still not clear.

2.2 Vortex Breakdown

Swirling flows are observed in nature as tornadoes, dust devils, hurricanes, and fire whirls. They are also used for technical applications such as the micro-bubble generator, swirl fuel injector, and gas turbine swirl burner. In these swirling flows, the swirl level (measured by the ratio of the azimuthal to axial velocity intensities) has significant effects on the vortex stability. When the swirl level is increased to a critical point, the adverse pressure gradient, which forms along the vortex axis, can be strong enough to overcome the axial momentum. The flow field then adjusts and reaches a new state with a stagnation point and a finite recirculation zone forming downstream around the jet centerline. This new state arising due to vortex breakdown has a strong effect on the ensuing fluid dynamics.

The types and result of vortex breakdown is described by flow structures seen in early experimental investigations. Sarpkaya's flow visualization [33, 34] shows three types of vortex breakdown, each with a distinctive internal structure. These modes are the bubble, spiral, and the double-helix modes, which are shown in Figs. 2.1 to 2.3. They were identified visually by injecting dye into the center of the jet flow. A fourth mode, an open conical sheet, was recognized by Billant et al. [35] through experiments.

Modes of vortex breakdown

1. Spiral mode

Figure 2.1: Spiral mode of vortex breakdown (from [33]). Flow goes from left to right and a dye is injected into the center of the flow.

The spiral mode is characterized by a deceleration and thereby stagnation of the dye filament along the centerline of the vortex with twisting and breaking up of the dye downstream, as shown in Fig. 2.1. The winding of the spiral has been observed to occur in the same direction of the outer flow [33, 34, 36], or in the opposition direction [37, 38].

2. Double-helix mode

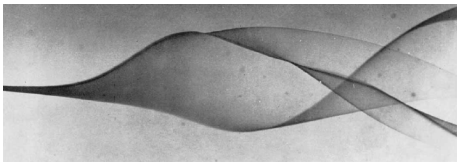

Figure 2.2: Double-helix mode of vortex breakdown (from [33]). Flow goes from left to right and a dye is injected into the center of the flow.

The double-helix mode is observed with the dye filament expanding into a slightly curved triangular sheet. The sheet divides from the centerline of the vortex and each half is wrapped by the other. The two helical sheets rotate in the same direction. This type of breakdown is highly sensitive to disturbances and it gradually breaks up into mild turbulence.

3. Axisymmetric mode or bubble mode

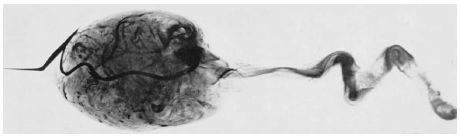

Figure 2.3: Bubble breakdown with a loose spiral downstream (from [33]). Flow goes from left to right and a dye is injected into the center of the flow.

The bubble mode is characterized by a stagnation point on the swirl axis leading to an abrupt expansion that forms a recirculation zone with an open end downstream. The recirculation zone forms a smooth, nearly symmetric bubble. The bubble is simultaneously filled and emptied by a toroidal vortex ring at the downstream half of the bubble [34]. The toroidal ring sometimes gyrates around its axis, which creates precession in the downstream vortex. The fluid in the bubble has a low-frequency motion and a long residence time.

The flow around the outside of the bubble remains relatively unaffected by this disturbance [34].

4. Cone mode

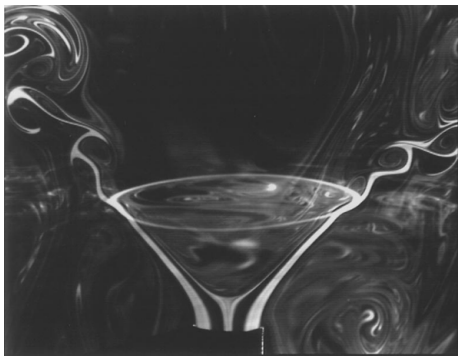

Figure 2.4: Cone mode of vortex breakdown (from [35]). Flow is from bottom to top. Fluorescein dye was introduced at the flow inlet. Two laser sheets were simultaneously produced, one in a meridional plane and the other in a plane slanted from the horizontal.

The cone mode takes the form of a conical sheet flowing over an open region of stagnant fluid. Here, in constrast to the bubble mode,the flow does not close towards the vortex axis and enclose a recirculation zone. There is recirculation inside the cone, but it is much weaker and slower than in the case of the bubble [35].

Faler and Leibovish reported flow visualizations [39] that showed seven types of changes in the vortex core. They were done in water. Some of the modes are intermediate stages that appear between the three predominant modes described above. An early stage of spiral mode is included as a different type. The bubble mode is also divided into three modes, which are a smooth bubble mode, a ragged

bubble mode, and a bubble mode with all the dye filament recirculating within the bubble.

2.2.1 Vortex Breakdown in Nonreactive Systems

Studies of vortex breakdown were initially performed in uncompressible, non-reactive, liquid systems. Early experimental research focused on the evolutionary pattern, the controlling parameters, and the flow structure resulting from vortex breakdown. Examples include experiments using delta wings ([40, 41]), in confined tubes ([33, 36, 38, 42, 43, 44]), in a cylindrical container with a rotating endwall ([45]), or in a free swirl jet ([35, 46]). Subsequent numerical simulations investigated the internal structure and flow field of vortex breakdown. Examples include axisymmetric incompressible simulations by Grabowski & Berger [28] and Krause, Shi & Hartwich [47], and three-dimensional simulations by Spall, Gatski & Ash[48] and Ruith et al. [27]. There was also theoretical analyses that attempted to explain vortex breakdown. The theories will be described further on. Although extensive experimental, numerical, and theoretical research has been undertaken for almost 50 years, there is no generally accepted theoretical explanation for the mechanism of vortex breakdown and the states that evolve.

2.2.1.1 Evolutionary Pattern

A map of vortex breakdown modes and mean axial position as a function of Reynolds number and circulation level was developed by Sarpkaya [33] and is shown

in Fig. 2.5. In this experiment, average Reynolds numbers varied from around $1,000$ to $10,000$, and only the bubble and spiral modes were recorded. Figure 2.5 shows that there is a pattern in the flow evolution that emerges as the flow parameters vary. For fixed Reynolds number and as the circulation level was increased, the spiral mode occurred before the bubble mode. When the circulation level was sufficiently large, the spiral mode transitioned into the bubble mode. The axial position of the bubble mode was always downstream of the origin of the spiral mode. For fixed circulation level and as the Reynolds number was increased, the same order of progression applied.

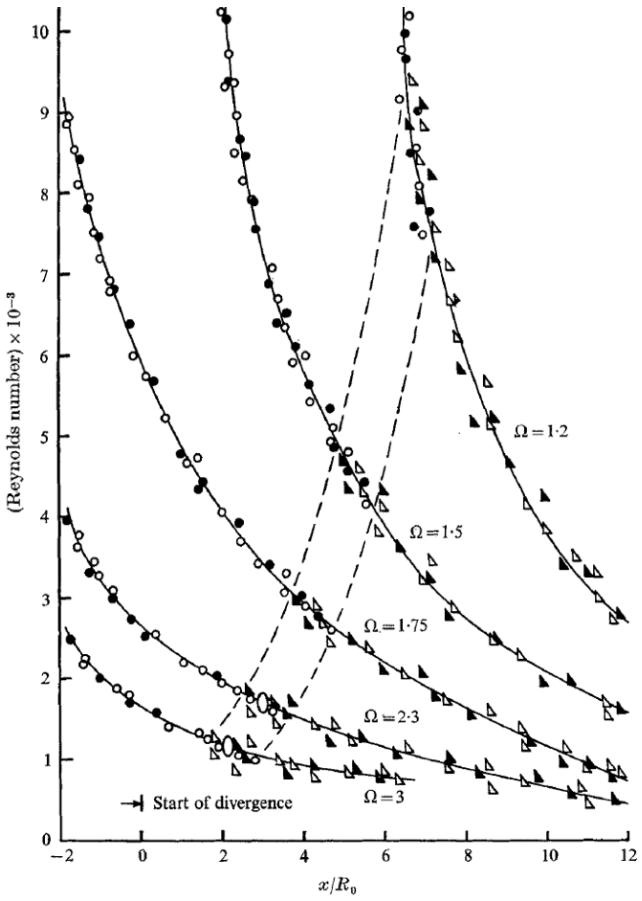

Figure 2.5: Axial position of vortex breakdown as a function of Reynolds number and different levels of circulation. Figure taken from [33]. Circles denote bubble mode and the triangles denote the spiral mode. Open and close markers corresponds to two different experimental conditions to adjust the circulation level. The observed vortex breakdown hysteresis is in the region between the two dashed lines.

A hysteresis effect was observed where both spiral and bubble modes can exist and transition spontaneously into each other in a range of flow parameters. In the region bordered by dash lines in Fig. 2.5, if the experiments were started at a lower Reynolds number with the initial form being the spiral mode, increasing the Reynolds number made the spiral mode move upstream but maintain its form. If starting at a higher Reynolds number with the initial form being the bubble mode, decreasing Reynolds number makes the bubble move downstream but also maintain

its form. In the hysteresis region, both forms are highly unstable and transition into each other under small disturbances from upstream [33].

An adverse pressure gradient is critical for vortex breakdown to occur. Increasing adverse pressure gradient results in lower critical values of Reynolds number and circulation level at which initial formation of vortex breakdown or transition between different modes occurs. This was observed by Sarpkaya and details can be found in [43].

Multiple modes of vortex breakdown can exist at the same time. Evolution of multiple modes as a function of controlling parameters was numerically investigated by Ruith et al. [27] through a series of 3D direct numerical simulations (DNS). In his numerical configuration, the controlling flow parameters are the Reynolds number and swirl number (level of circulation). The influence of swirl number was studied by only varying the swirl number and keeping the other parameters constant. As shown in Fig. 2.6, the case with lowest swirl number remained axisymmetric and formed a steady bubble mode upstream. As the swirl number was increased, the bubble upstream remained quasi-steady axisymmetric while the downstream became helically unstable. Eventually the downstream settled into a double-helix mode at a higher swirl number.

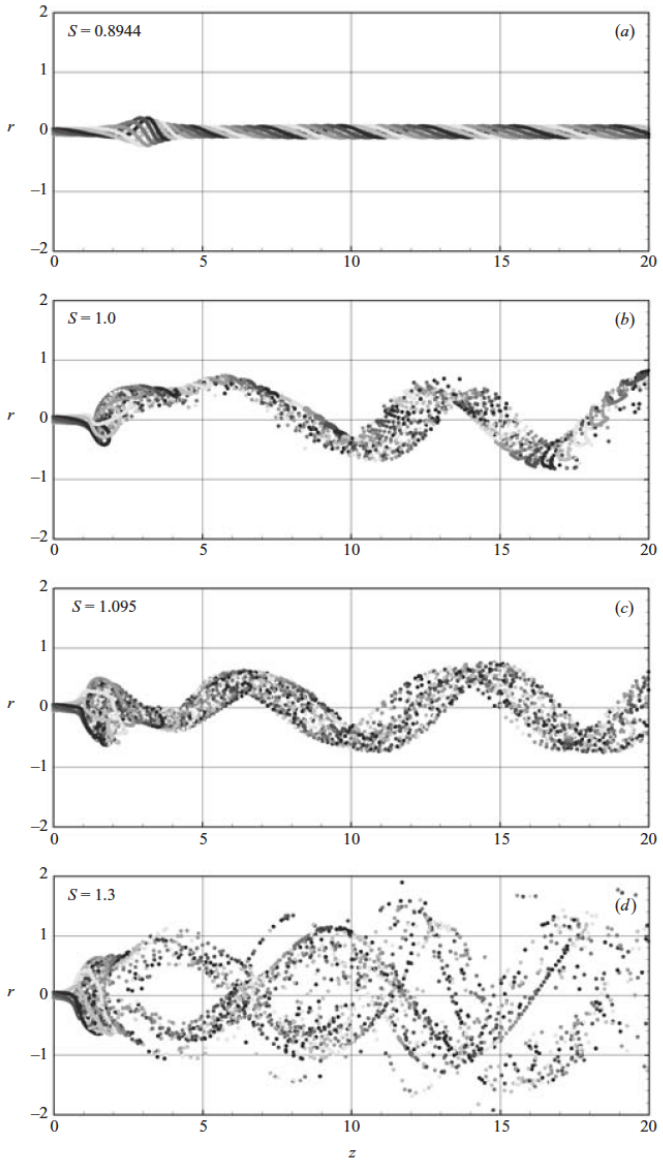

Figure 2.6: Streaklines of simulations with different swirl numbers at one instant of time. Figure taken from [27].

Figure 2.7 from Ruith et al. [27] shows the influence of Reynolds number by only varying the Reynolds number and keeping the other parameters constant. As shown in Fig. 2.7, the case with lowest Reynolds number remained axisymmetric and formed a steady bubble mode upstream. As the Reynolds number was increased,

the downstream became helically unstable. The downstream eventually developed into a double-helix mode at larger Reynolds numbers.

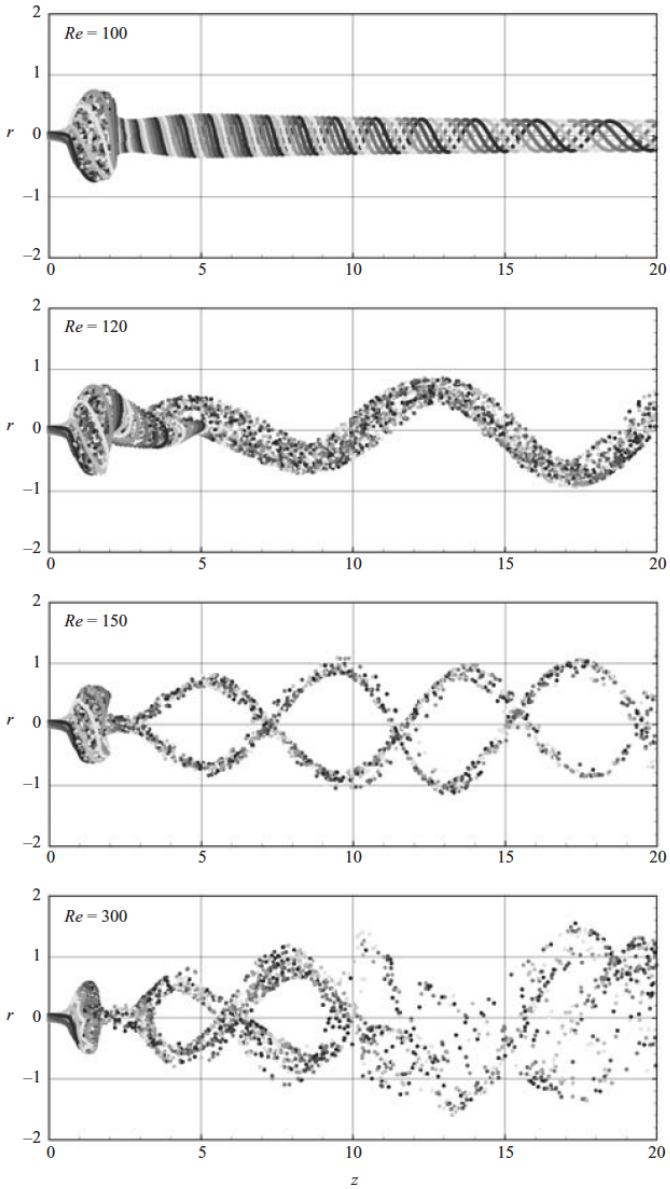

Figure 2.7: Streaklines of simulations with different Reynolds numbers at one instant of time. Figure taken from [27].

2.2.1.2 Structure of Vortex Breakdown

The structure of vortex breakdown was first quantitatively described by Faler & Leibovich [49] for a bubble mode of vortex breakdown. A two-celled structure in the interior of the recirculation zone was revealed through time-averaged axial velocity measurements under the axisymmetric assumption, as shown in Fig. 2.8. The inner cell has positive velocities near the axis, which are oriented downstream. The outer ring-like structure has a reversed flow near the axis.

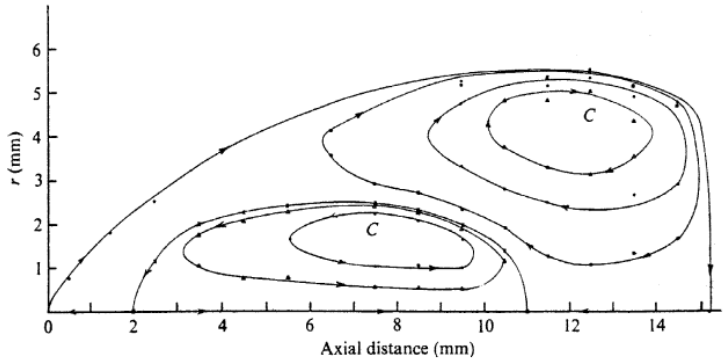

Figure 2.8: Double ring structure of a bubble mode. Figure taken from [49].

A 3D schematic was presented later by Uchida et al. [50] through LDV(Laser Doppler Velocimetry) measurements, as shown in Fig. 2.9. In this configuration, the axisymmetric bubble mode has a spiral mode downstream. The flow is reversed and trapped into the bubble through the outer region of the bubble. The flow near the axis in the upstream region of the bubble approaches a positive and low value, and then abruptly increases in the downstream half before decreasing again when reaching the second spiral mode. The bubble exchanges fluid with the outer flow through its downstream end.

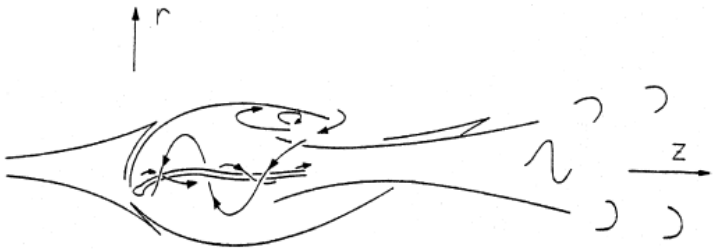

Figure 2.9: Three-dimensional schematic diagram of the flow pattern in a bubble mode. Figure taken from [50].

2.2.1.3 Theories and Explanations for Vortex Breakdown

The theories that attempt to describe vortex breakdown can be categorized into three types of explanations, the existence of a critical state [51, 52]; a failure of the quasi-cylindrical approximation (QCA) [53, 54]; and a hydrodynamic instability [55, 56, 57]. Earlier theories focused on predicting the location of the occurrence of vortex breakdown while the later ones attempted to explain the whole physical process and the flow structure.

The explanation of the existence of a critical state was proposed independently by Squire [51] and Benjamin [52]. They suggested that vortex breakdown is associated with a wave phenomenon, for which vortex breakdown is a critical state separating the supercritical state upstream from the subcritical state downstream. In a subcritical flow, disturbances can propagate both upstream and downstream, whereas in a supercritical flow, only downstream propagation is allowed. Squire [51] viewed vortex breakdown as an accumulation of upstream disturbances at a critical state, which is analogous to a shock wave. Benjamin [52] understood vortex

breakdown as an abrupt change between two conjugate flow state, more like a hydraulic jump. The consistency between these two understandings was demonstrated by Bossel [58]. Breuer [59], however, found that the transition from a supercritical to subcritical flow state is a necessary but not sufficient condition for vortex breakdown.

The QCA was used to estimate the position and occurrence of vortex breakdown [60, 61]. One feature of vortex breakdown is the stagnation point near the vortex axis. Based on this feature, the location where the calculations using the QCA fails to converge should be related to the occurrence and position of vortex breakdown. The failure of QCA and critical state are related [62]. For viscous flows, the point of failure of QCA precedes the critical point due to viscosity [63]. For inviscid flows, the point where the QCA fails corresponds exactly to the critical state [60]. The method of QCA is limited as it cannot account for upstream influences and cannot predict the flow downstream of the stagnation point.

The stability of vortex flows has also been studied to explain vortex breakdown. The first important stability criterion for inviscid circular flow was proposed by Rayleigh [64]. Later, generalised Rayleigh's criteria for stability to axisymmetric disturbances [56] and spiral disturbances [65] were proposed. Lessen el al. [66] performed a linearized inviscid stability analysis considering different modes of disturbance. The result was applied to experimental data by Garg and Leibovich [67] and there was good agreement. The instability explanation, however, does not explain vortex breakdown completely. Harvey [42] argued that the perturbation would have grown unchecked and thus the flow would have developed into an unsteady,

random motion if vortex breakdown had been due to the instability. Escudier [68] also argued that the breakdown appears as a sudden transition instead of a gradual transition, and there is no reason for the origin of the instability to always have the same rotating characteristics. From all of the investigations, it seems that instabilities play a secondary role in vortex breakdown.

2.2.2 Vortex Breakdown in Reactive Systems

Vortex breakdown is useful in combustion systems that use a recirculation zone to stabilize the flame and enhance fuel and air mixing. Vortex breakdown in combustion systems also introduces reliability problems arising from flame flashback due to combustion induced vortex breakdown (CIVB) [69, 70, 71] and precessing vortex core (PVC) [15, 72]. The studies on vortex breakdown in reactive systems mainly focus on these two areas. CIVB is due to the bubble mode of vortex breakdown and PVC is related to the helical modes.

2.2.2.1 Flame Flashback - Combustion Induced Vortex Breakdown (CIVB)

Flame flashback is a reliability problem in lean premixed combustion where the flame propagates upstream when the burning velocity exceeds the local flow velocity. The flame flashback into the mixing section can cause overheating and lead to failure of the entire combustion system. In general, flashback can arise from flame propagation in the boundary layer or combustion instabilities [73]. In swirl-stabilized

combustors, flame flashback can be triggered by CIVB [70, 73, 74] (show in Fig. 2.10). CIVB was first observed as a form of flashback in experiments by Fritz, Kröner & Sattelmayer [75]. Kröner [70, 76] developed a correlation of the flashback limits for a wide range of methane-hydrogen mixtures, which reveals that quenching of the chemical reaction is the governing factor of the flashback limit and the heat release in the propagating bubble is balanced by the turbulent mixing and flame quenching. The root cause for CIVB driven flashback was investigated by Kiesewetter, Konle & Sattelmayer [69] using numerical simulations. They found out that the baroclinic torque in the flame generates negative vorticity inside the bubble and is responsible for CIVB driven flash back. Konle & Sattelmayer [71] further studied the interaction of heat release and the bubble mode of vortex breakdown. They concluded that the bubble propagates upstream when the flame tip is downstream of the stagnation point of the bubble. The propagation is prohibited if the flame is close or upstream of the stagnation point. All of the studies on CIVB driven flashback, however, only focused on the heat release effects on the bubble mode of vortex breakdown.

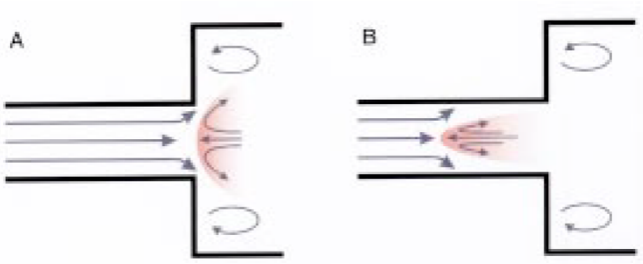

Figure 2.10: Schematic of flame in a swirl combustor. (A) A stable flame; (B) A flashback due to CIVB. Figure taken from [70]

2.2.2.2 Precessing Vortex Core (PVC)

In swirl combustors, a central recirculation zone is generated at sufficient swirl level to stabilize the flame [12, 13]. At certain operation conditions, an off-axis precession of the vortex core (shown in Fig. 2.11) arises with a periodic motion [15, 77, 78, 79]. On one hand, the precession can help enhance mixing and increase combustion efficiency [80]. On the other hand, the oscillation in pressure and velocity can cause acoustic excitation of the flame and resonate with the vibration of the combustor, which imposes potential danger to the operation [81].

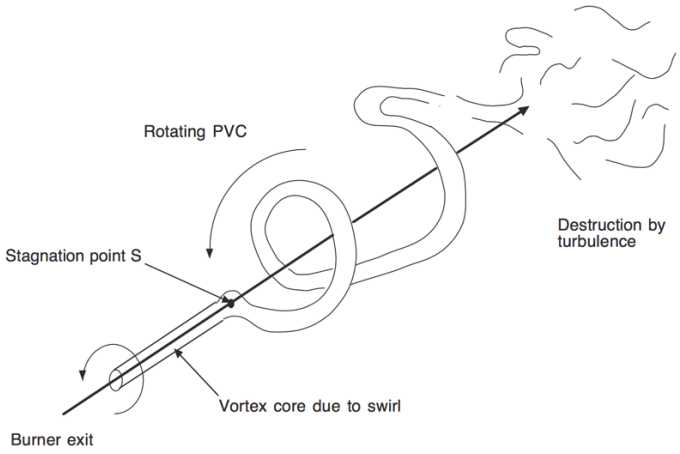

Figure 2.11: Structure of PVC. Figure taken from [82]

PVC in a combustion system was first identified by Syred & Beer [13]. The occurence of PVC in a combustion system was reviewed in [15], which summarized that the PVC amplitude is a function of the mode of fuel entry, equivalence ratio and level of confinement . Axial or tangential fuel entry can suppress the amplitude of PVC [83]. Premixed or partially premixed combustion promotes PVC [12, 13].The

precession frequency grows linearly with the mass flow rate [12] and changes non-monotonically with the swirl level [77, 84, 85]. The amplitude of PVC is supressed strongly in reactive flows compared with isothermal conditions [13, 79, 86]. The amplitude of PVC is affected by the flame location. If the flame front is close to the burner inlet, the PVC is supressed [87]. The amplitude of PVC is also affected by the flame shape, Oberleithner et al. [72, 88] found that a detached M-flame promotes PVC while an attached V-flame suppresses PVC. Over the past few decades, although experimental and numerical research was performed on PVC, its occurrence, development, and intensity are still not well understood and documented.

Early studies on PVC in reactive flows were performed using industrial-type swirl stabilized burners or electric discharge chambers. The complex geometry may impose extra difficulty on studying the combustion effects on PVC. Moreover, the heat release region and intensity are always connected to the flame shape and cannot be adjusted freely. Some recent studies adopted simplied configuiration of swirling flows to study the heat release impact on PVC in a more controlled way. The experiment by Rukes et al. [89, 90] applied heating to a swirling flow by a curled heating wire. They found that mild heating of the bubble mode increases the amplitude of PVC and strong heating suppresses the PVC. The PVC is suppressed if the density gradient is within the inner shear layer of the axial velocity and promoted otherwise. A numerical study on the impact of heat release on PVC was performed by Gorbunova et al. [91] where a simplified configuration of swirling flow is adopted with a source of heat around the vortex axis. They concluded that when the heat-source power increases, the PVC frequency increases while the amplitude decreases.

Most studies of PVC in swirl combustors focused on the occurrence and frequency of PVC. PVC was not explicitly related to vortex breakdown until 2016. Vanierschot, Percin & Oudheusden [92] and Gorbunova et al. [91] related PVC to the spiral mode of vortex breakdown. Recent discovery of a double structure in PVC [79] (shown in Fig. 2.12) added more evidence that PVC could be related to the modes of vortex breakdown, as the double structure is analogous to the double-helix mode.

Figure 2.12: Double helical PVC structures. Figure taken from [79]

Therefore, the topic of interest on the combustion impact on PVC leads to a broader and more fundamental topic that is the thermal impact on vortex breakdown. A fundamental study on the thermal effects on vortex breakdown is needed using a simplified and controlled configuration for swirling flows that undergoes different modes of vortex breakdown. This study could help understand how heat release and extraction influences the vortex breakdown structure and mode changes, which could then serve as a base and further help understand the PVC structure

and its frequency and amplitude changes in combustion systems under different operation conditions.

2.3 Low-Mach-Number Algorithms[1]

The motivation of the algorithm described in this work is the need to calculate low-speed flows accurately and economically. In this flow regime, fluid velocities range from centimeters to tens of meters per second, which could be hundreds of times smaller than the sound speed. If the sound speed restriction in the stability limit could be removed, the computational cost would be at least one or two order of magnitude lower. This has been the motivation for developing low-Mach number, implicit algorithms.

One way to remove the sound speed limit is to make the time integration implicit, such as MacCormack method [93], semi-implicit ICE method [94], implicit nonlinear PPM [95] and TVD methods [96]. These implicit calculations are accurate but very expensive. Improvements on reducing the computational cost are reported in recent works, including the methods developted by Wall, Pierce & Moin [97] and Degond & Tang [98]. Another technique is the perturbation or asymptotic approach. The physical acoustic waves are decoupled from the system of equations by using regular perturbation theory and applying Taylor series expansion on the variables in power terms of the Mach number. Examples of this approach include the methods developed by Jones & Boris [99], Rehm & Baum [100], Paolucci [101], Pember et al.

[1]This section is a slightly modified version of what has been published in [1] and has been reproduced here with the permission of the copyright holder.

[102], Nicoud [103] and Thornber et al. [104]. The asymptotic approximation still allows compression and rarefaction over time as long as the Mach number is small enough. The spatial variations in pressure, however, are filtered out, which means acoustic wave effects are eliminated.

The barely implicit correction (BIC), originally proposed by Patnaik et al. [20], eliminated the sound speed restriction by solving the governing equations at a large time step determined by the fluid velocity (predictor step), and then applying a pressure correction that effectively equilibrates the acoustic waves. More specifically, at each time step, a pressure correction is applied to the momentum and energy equations (corrector step). Patnaik et al. used the flux-corrected transport (FCT) for the predictor step value, although in principle, any monotone algorithm should work just as well.

The original BIC algorithm [20] was used for one-dimensional and two-dimensional problems, and, in particular, for reactive flows. Examples include computations of a premixed cellular flame structure (Patnaik et al. [21]), and simulations of axisymmetric methane-air diffusion flames (Kaplan et al. [22]). These multidimensional reactive-flow computations produced quantitative results when compared to experiments. Nonetheless, there were numerical issues that caused some problems in the execution, such as small, sometimes growing pressure oscillations that had to be damped. Patnaik et al. [21] filtered these oscillations from the solutions by using a high-frequency pressure filter. Kaplan et al. [22] reduced oscillations to an acceptable level by using a control algorithm for the outflow boundary condition.

Chapter 3: Numerical Algorithm - Flux-Corrected Transport (FCT)

3.1 Overview

FCT [17] is one of the earliest monotonocity-preserving algorithms that avoids numerical oscillations in regions of the solution that are not smooth while minimizing error from numerical diffusion. Its idea is to apply numerical diffusion to the solution so that the solution remains monotonic without numerical oscillations and then remove the numerical diffusion from regions of the solution that do not require the diffusion. This idea was proposed by Boris in 1971 [105] and initially used by an algorithm called SHASTA [17, 105]. It computed gasdynamic shock waves with sharp resolution and non-oscillitory results. More refinements were then applied to this idea such as the extension of FCT to a fully multidimensional form by Zalesak [18], an improved flux limiter for multidimensions by DeVore [19], and an algorithm called LCPFCT [106] which solves the generalized continuity equations with fourth-order phase accuracy and minimal residual diffusion. Since its original publication, FCT has been applied in many areas of science, from aerodynamics and shock physics, to astrophysics, magnetohydrodynamics, and computational biology. A summary of FCT can be found in the book by Oran and Boris [107].

In this work, we use the LCPFCT version [106] of FCT to solve the convec-

tion processes in the conservation equations. In the original document [106], the solution procedure was outlined for a 1D continuity equation. For multidimensional calculations, direction splitting was suggested [106], which treats the x-direction and y-direction terms separately and sequentially using a general 1D continuity equation. This approach requires small time steps for accuracy and bias is often introduced depending on which direction is integrated first. Here, we use the fully multidimensional FCT form developed by Zalesak [18] to avoid these issues. The original fully multidimensional FCT [18], however, was only positivity preserving but not monotonicity preserving [19]. Devore [19] proposed an improvement to solve this issue. Calculation examples in 2D and 3D using this improved algorithm are shown in [19] with good results. The solution procedure shown in [19], however, is only in 2D. In the following section, we outline the complete solution procedure using LCPFCT as the base solver with Zalesak's multidimensional form and Devore's improvement for 3D problems.

3.2 Governing Equations and Solution Steps

The generalized 3D continuity equations are

$$\frac{\partial \mathbf{R}}{\partial t} = -\frac{\partial \mathbf{K_1}}{\partial x} - \frac{\partial \mathbf{K_2}}{\partial y} - \frac{\partial \mathbf{K_3}}{\partial z} - \frac{\partial \mathbf{D_1}}{\partial x} - \frac{\partial \mathbf{D_2}}{\partial y} - \frac{\partial \mathbf{D_3}}{\partial z} + \mathbf{D_4}, \tag{3.1}$$

with

$$\mathbf{R} = \begin{bmatrix} \rho \\ \rho u \\ \rho v \\ \rho w \\ E \end{bmatrix}, \quad \mathbf{K_1} = \begin{bmatrix} \rho u \\ \rho u^2 \\ \rho uv \\ \rho uw \\ Eu \end{bmatrix}, \quad \mathbf{K_2} = \begin{bmatrix} \rho v \\ \rho uv \\ \rho v^2 \\ \rho vw \\ Ev \end{bmatrix}, \quad \mathbf{K_3} = \begin{bmatrix} \rho w \\ \rho uw \\ \rho vw \\ \rho w^2 \\ Ew \end{bmatrix},$$

$$\mathbf{D_1} = \begin{bmatrix} 0 \\ P \\ 0 \\ 0 \\ Pu \end{bmatrix}, \quad \mathbf{D_2} = \begin{bmatrix} 0 \\ 0 \\ P \\ 0 \\ Pv \end{bmatrix}, \quad \mathbf{D_3} = \begin{bmatrix} 0 \\ 0 \\ 0 \\ P \\ Pw \end{bmatrix}, \quad \mathbf{D_4} = \begin{bmatrix} 0 \\ 0 \\ 0 \\ 0 \\ 0 \end{bmatrix}. \tag{3.2}$$

Here t is time, ρ is density, P is pressure, and E is the total energy

$$E = \rho(\frac{1}{2}\mathbf{V^2} + \mathbf{e}), \tag{3.3}$$

where e is the specific internal energy. The variables u, v, and w are velocities in the x, y, and z directions. D_4 is an additional source term which, for example, could be a mass production rate in the continuity equation or an energy production rate in the energy equation. This source term is initialized as zero here and is shown to demonstrate how to include additional source terms.

FCT in general has two major steps to preserve positivity and monotonicity while minimizing numerical dissipation. The first step is to convect and numerically

diffuse the solution to guarantee monotonicity. This is done by calculating a low-order, numerically diffused solution. The low-order solution can be written in a finite difference approximation form as

$$\begin{aligned}\widetilde{\mathbf{R}}_{i,j,k} = \mathbf{R}^{o}_{i,j,k} &- (\mathbf{F}^{L}_{i+\frac{1}{2},j,k} - \mathbf{F}^{L}_{i-\frac{1}{2},j,k}) \\ &- (\mathbf{G}^{L}_{i,j+\frac{1}{2},k} - \mathbf{G}^{L}_{i,j-\frac{1}{2},k}) \\ &- (\mathbf{H}^{L}_{i,j,k+\frac{1}{2}} - \mathbf{H}^{L}_{i,j,k-\frac{1}{2}}) \\ &+ \Delta t \mathbf{D_4}.\end{aligned} \tag{3.4}$$

Here $\mathbf{F}^L$, $\mathbf{G}^L$, and $\mathbf{H}^L$ are the low-order fluxes in the x, y, and z directions, respectively. Notation 'o' refers to values at the beginning of the time step. The second step adds a corrected flux (antidiffuion) to the low-order solution $\widetilde{\mathbf{R}}$ to reduce numerical diffusion while avoiding introducing new extrema. The final solution can be written as

$$\begin{aligned}\mathbf{R}^{n}_{i,j,k} = \widetilde{\mathbf{R}}_{i,j,k} &- (\mathbf{F}^{C}_{i+\frac{1}{2},j,k} - \mathbf{F}^{C}_{i-\frac{1}{2},j,k}) \\ &- (\mathbf{G}^{C}_{i,j+\frac{1}{2},k} - \mathbf{G}^{C}_{i,j-\frac{1}{2},k}) \\ &- (\mathbf{H}^{C}_{i,j,k+\frac{1}{2}} - \mathbf{H}^{C}_{i,j,k-\frac{1}{2}}).\end{aligned} \tag{3.5}$$

Here $\mathbf{F}^C$, $\mathbf{G}^C$, and $\mathbf{H}^C$ are the corrected fluxes in the x, y, and z directions, respectively. The superscript 'n' refers to values at the new time step. The details of how to calculate the low-order and corrected fluxes are explained as follows.

The low-order flux contains two parts, which are the convection (transport) flux and the numerical diffusion flux. Using the fluxes at the cell edge ($+\frac{1}{2}$) as an

example, we can then write the low-order fluxes as

$$\mathbf{F}^{L}_{i+\frac{1}{2},j,k} = \mathbf{F}^{T}_{i+\frac{1}{2},j,k} + \mathbf{F}^{D}_{i+\frac{1}{2},j,k}, \tag{3.6}$$

$$\mathbf{G}^{L}_{i,j+\frac{1}{2},k} = \mathbf{G}^{T}_{i,j+\frac{1}{2},k} + \mathbf{G}^{D}_{i,j+\frac{1}{2},k}, \tag{3.7}$$

$$\mathbf{H}^{L}_{i,j,k+\frac{1}{2}} = \mathbf{H}^{T}_{i,j,k+\frac{1}{2}} + \mathbf{H}^{D}_{i,j,k+\frac{1}{2}}. \tag{3.8}$$

Here we use the superscript 'T' to denote the convection (transport) fluxes to be consistent with [106]. The transport fluxes at the cell edge ($+\frac{1}{2}$) can be written as

$$\mathbf{F}^{T}_{i+\frac{1}{2},j,k} = \frac{\Delta t}{\Delta x}\left(\mathbf{K_1}_{i+\frac{1}{2},j,k} + \mathbf{D_1}_{i+\frac{1}{2},j,k}\right) = \frac{\Delta t}{\Delta x}\left(\mathbf{R}^{o}_{i+\frac{1}{2},j,k} u_{i+\frac{1}{2},j,k} + \mathbf{D_1}_{i+\frac{1}{2},j,k}\right), \tag{3.9}$$

$$\mathbf{G}^{T}_{i,j+\frac{1}{2},k} = \frac{\Delta t}{\Delta y}\left(\mathbf{K_2}_{i+\frac{1}{2},j,k} + \mathbf{D_2}_{i+\frac{1}{2},j,k}\right) = \frac{\Delta t}{\Delta y}\left(\mathbf{R}^{o}_{i,j+\frac{1}{2},k} v_{i,j+\frac{1}{2},k} + \mathbf{D_2}_{i,j+\frac{1}{2},k}\right), \tag{3.10}$$

$$\mathbf{H}^{T}_{i,j,k+\frac{1}{2}} = \frac{\Delta t}{\Delta z}\left(\mathbf{K_3}_{i+\frac{1}{2},j,k} + \mathbf{D_3}_{i+\frac{1}{2},j,k}\right) = \frac{\Delta t}{\Delta z}\left(\mathbf{R}^{o}_{i,j,k+\frac{1}{2}} w_{i,j,k+\frac{1}{2}} + \mathbf{D_3}_{i,j,k+\frac{1}{2}}\right), \tag{3.11}$$

where

$$\mathbf{R}^o_{i+\frac{1}{2},j,k} = \frac{1}{2}(\mathbf{R}^o_{i+1,j,k} + \mathbf{R}^o_{i,j,k}), \tag{3.12}$$

$$\mathbf{R}^o_{i,j+\frac{1}{2},k} = \frac{1}{2}(\mathbf{R}^o_{i,j+1,k} + \mathbf{R}^o_{i,j,k}), \tag{3.13}$$

$$\mathbf{R}^o_{i,j,k+\frac{1}{2}} = \frac{1}{2}(\mathbf{R}^o_{i,j,k+1} + \mathbf{R}^o_{i,j,k}), \tag{3.14}$$

$$u_{i+\frac{1}{2},j,k} = \frac{1}{2}(u_{i+1,j,k} + u_{i,j,k}), \tag{3.15}$$

$$v_{i,j+\frac{1}{2},k} = \frac{1}{2}(v_{i,j+1,k} + v_{i,j,k}), \tag{3.16}$$

$$w_{i,j,k+\frac{1}{2}} = \frac{1}{2}(w_{i,j,k+1} + w_{i,j,k}), \tag{3.17}$$

$$\mathbf{D_1}_{i+\frac{1}{2},j,k} = \frac{1}{2}(\mathbf{D_1}_{i+1,j,k} + \mathbf{D_1}_{i,j,k}), \tag{3.18}$$

$$\mathbf{D_2}_{i,j+\frac{1}{2},k} = \frac{1}{2}(\mathbf{D_2}_{i,j+1,k} + \mathbf{D_2}_{i,j,k}), \tag{3.19}$$

$$\mathbf{D_3}_{i,j,k+\frac{1}{2}} = \frac{1}{2}(\mathbf{D_3}_{i,j,k+1} + \mathbf{D_3}_{i,j,k}). \tag{3.20}$$

The fluxes at the $(-\frac{1}{2})$ cell edge are computed by simply subtracting 1 from the cell indices shown for the $(+\frac{1}{2})$ terms.

The convection (transport) solutions in the x, y, and z directions are then

$$\mathbf{R}^{Tx}_{i,j,k} = \mathbf{R}^o_{i,j,k} - (\mathbf{F}^T_{i+\frac{1}{2},j,k} - \mathbf{F}^T_{i-\frac{1}{2},j,k}), \tag{3.21}$$

$$\mathbf{R}^{Ty}_{i,j,k} = \mathbf{R}^o_{i,j,k} - (\mathbf{G}^T_{i,j+\frac{1}{2},k} - \mathbf{G}^T_{i,j-\frac{1}{2},k}), \tag{3.22}$$

$$\mathbf{R}^{Tz}_{i,j,k} = \mathbf{R}^o_{i,j,k} - (\mathbf{H}^T_{i,j,k+\frac{1}{2}} - \mathbf{H}^T_{i,j,k-\frac{1}{2}}). \tag{3.23}$$

After convection, oscillations can arise in the convection solutions near steep gradients. Therefore, a calculated amount of numerical diffusion needs to be added

to the convection (transport) solution to ensure monotonicity. The diffusion fluxes can be written as

$$\mathbf{F}^D_{i+\frac{1}{2},j,k} = \nu^{(1)}_{i+\frac{1}{2},j,k}(\mathbf{R}^o_{i+1,j,k} - \mathbf{R}^o_{i,j,k}), \tag{3.24}$$

$$\mathbf{G}^D_{i,j+\frac{1}{2},k} = \nu^{(1)}_{i,j+\frac{1}{2},k}(\mathbf{R}^o_{i,j+1,k} - \mathbf{R}^o_{i,j,k}), \tag{3.25}$$

$$\mathbf{H}^D_{i,j,k+\frac{1}{2}} = \nu^{(1)}_{i,j,k+\frac{1}{2}}(\mathbf{R}^o_{i,j,k+1} - \mathbf{R}^o_{i,j,k}). \tag{3.26}$$

Here the value of the diffusion coefficient $\nu^{(1)}$ can be chosen to achieve a desired amplitude and phase accuracy [106]. The value in [106] was optimized for 1D. For 3D, we found that stability should also be considered when choosing the value for $\nu^{(1)}$. In this work, we set the value of $\nu^{(1)}$ for stability in 3D while maintaining the accuracy of the original LCPFCT algorithm. To do this, we separate the numerical diffusion into two parts, $\nu^{(1)}$ and $\nu^{(2)}$. We add $\nu^{(1)}$ here at the diffusion stage and add $\nu^{(2)}$ at the antidiffusion stage which is described later. The value of $\nu^{(1)}$ is listed below and the details of how we choose the value are described in the following stability section.

$$\nu^{(1)}_{i+\frac{1}{2},j,k} = \frac{1}{12} + \frac{1}{3}\epsilon^2_{i+\frac{1}{2},j,k}, \tag{3.27}$$

$$\nu^{(1)}_{i,j+\frac{1}{2},k} = \frac{1}{12} + \frac{1}{3}\epsilon^2_{i,j+\frac{1}{2},k}, \tag{3.28}$$

$$\nu^{(1)}_{i,j,k+\frac{1}{2}} = \frac{1}{12} + \frac{1}{3}\epsilon^2_{i,j,k+\frac{1}{2}}, \tag{3.29}$$

where

$$\epsilon_{i+\frac{1}{2},j,k} = \frac{1}{2}(u_{i,j,k} + u_{i+1,j,k})\frac{\Delta t}{\Delta x}, \tag{3.30}$$

$$\epsilon_{i,j+\frac{1}{2},k} = \frac{1}{2}(v_{i,j,k} + v_{i,j+1,k})\frac{\Delta t}{\Delta y}, \tag{3.31}$$

$$\epsilon_{i,j,k+\frac{1}{2}} = \frac{1}{2}(w_{i,j,k} + w_{i,j,k+1})\frac{\Delta t}{\Delta z}. \tag{3.32}$$

With the convection and diffusion fluxes, we can now calculate the low-order solution based on Eq. 3.4 and Eqs. 3.6 - 3.8. We can also write the interim low-order solution in one-dimensional form for the x, y, and z directions separately. We need this one dimensional form for the antidiffusion stage which is shown later.

$$\widetilde{\mathbf{R}}^{x}_{i,j,k} = \mathbf{R}^{Tx} + \mathbf{F}^{D}_{i+\frac{1}{2},j,k} - \mathbf{F}^{D}_{i-\frac{1}{2},j,k} + \Delta t\mathbf{D_4}, \tag{3.33}$$

$$\widetilde{\mathbf{R}}^{y}_{i,j,k} = \mathbf{R}^{Ty} + \mathbf{G}^{D}_{i,j+\frac{1}{2},k} - \mathbf{G}^{D}_{i,j-\frac{1}{2},k} + \Delta t\mathbf{D_4}, \tag{3.34}$$

$$\widetilde{\mathbf{R}}^{z}_{i,j,k} = \mathbf{R}^{Tz} + \mathbf{H}^{D}_{i,j,k+\frac{1}{2}} - \mathbf{H}^{D}_{i,j,k-\frac{1}{2}} + \Delta t\mathbf{D_4}. \tag{3.35}$$

After calculating the low-order solution, we then focus on the second major step, which is calculating the corrected fluxes. The idea of the corrected fluxes is to make the solution as accurate as possible by correcting the low-order solution while limiting the correction at the same time to prevent the formation of new extrema in the final solution. The calculation of the corrected fluxes consists of the following steps:

1. First, calculate the antidiffusive fluxes in the x, y, and z directions

$$\mathbf{F}^{ad}_{i+\frac{1}{2},j,k} = \mu_{i+\frac{1}{2},j,k}(\mathbf{R}^{Tx}_{i+1,j,k} - \mathbf{R}^{Tx}_{i,j,k}) - \nu^{(2)}(\mathbf{R}^{o}_{i+1,j,k} - \mathbf{R}^{o}_{i,j,k}), \tag{3.36}$$

$$\mathbf{G}^{ad}_{i,j+\frac{1}{2},k} = \mu_{i,j+\frac{1}{2},k}(\mathbf{R}^{Ty}_{i,j+1,k} - \mathbf{R}^{Ty}_{i,j,k}) - \nu^{(2)}(\mathbf{R}^{o}_{i,j+1,k} - \mathbf{R}^{o}_{i,j,k}), \tag{3.37}$$

$$\mathbf{H}^{ad}_{i,j,k+\frac{1}{2}} = \mu_{i,j,k+\frac{1}{2}}(\mathbf{R}^{Tz}_{i,j,k+1} - \mathbf{R}^{Tz}_{i,j,k}) - \nu^{(2)}(\mathbf{R}^{o}_{i,j,k+1} - \mathbf{R}^{o}_{i,j,k}). \tag{3.38}$$

Here, μ is the antidiffusion coefficient and $\nu^{(2)}$ is the residual of the diffusion coefficient. The residual $\nu^{(2)}$ is added here because of the stability issue in 3D and further details can be found in the following stability analysis section. In this work, we set μ and $\nu^{(2)}$ as

$$\mu_{i+\frac{1}{2},j,k} = \frac{1}{6} - \frac{1}{6}\epsilon^2_{i+\frac{1}{2},j,k}, \tag{3.39}$$

$$\mu_{i,j+\frac{1}{2},k} = \frac{1}{6} - \frac{1}{6}\epsilon^2_{i,j+\frac{1}{2},k}, \tag{3.40}$$

$$\mu_{i,j,k+\frac{1}{2}} = \frac{1}{6} - \frac{1}{6}\epsilon^2_{i,j,k+\frac{1}{2}}, \tag{3.41}$$

$$\nu^{(2)} = \frac{1}{12}. \tag{3.42}$$

Here, the value of μ is same as provided in [106].

2. Then, calculate the signed quantities $S_{i+\frac{1}{2}}$, $S_{j+\frac{1}{2}}$, and $S_{k+\frac{1}{2}}$ as

$$|S_{i+\frac{1}{2}}| = 1, \text{ and sign } S_{i+\frac{1}{2}} \equiv \text{sign}(\widetilde{\mathbf{R}}^{x}_{i+1,j,k} - \widetilde{\mathbf{R}}^{x}_{i,j,k}), \tag{3.43}$$

$$|S_{j+\frac{1}{2}}| = 1, \text{ and sign } S_{j+\frac{1}{2}} \equiv \text{sign}(\widetilde{\mathbf{R}}^{y}_{i,j+1,k} - \widetilde{\mathbf{R}}^{y}_{i,j,k}), \tag{3.44}$$

$$|S_{k+\frac{1}{2}}| = 1, \text{ and sign } S_{k+\frac{1}{2}} \equiv \text{sign}(\widetilde{\mathbf{R}}^{z}_{i,j,k+1} - \widetilde{\mathbf{R}}^{z}_{i,j,k}), \tag{3.45}$$

3. Prelimit the antidiffusive fluxes along the x, y, and z directions respectively to prevent the creation and enhancement of directional extrema. This step essentially applies the limiter as Eq. (3.21) in [106] in each coordinate direction.

$$\mathbf{F}^{ad'}_{i+\frac{1}{2},j,k} = S_{i+\frac{1}{2}} \max\left[0,\ \min\left(\left|\mathbf{F}^{ad}_{i+\frac{1}{2},j,k}\right|, S_{i+\frac{1}{2}}\left(\widetilde{\mathbf{R}}^{x}_{i,j,k} - \widetilde{\mathbf{R}}^{x}_{i-1,j,k}\right), S_{i+\frac{1}{2}}\left(\widetilde{\mathbf{R}}^{x}_{i+2,j,k} - \widetilde{\mathbf{R}}^{x}_{i+1,j,k}\right)\right)\right], \quad (3.46)$$

$$\mathbf{G}^{ad'}_{i,j+\frac{1}{2},k} = S_{j+\frac{1}{2}} \max\left[0,\ \min\left(\left|\mathbf{G}^{ad}_{i,j+\frac{1}{2},k}\right|, S_{j+\frac{1}{2}}\left(\widetilde{\mathbf{R}}^{y}_{i,j,k} - \widetilde{\mathbf{R}}^{y}_{i,j-1,k}\right), S_{j+\frac{1}{2}}\left(\widetilde{\mathbf{R}}^{y}_{i,j+2,k} - \widetilde{\mathbf{R}}^{y}_{i,j+1,k}\right)\right)\right], \quad (3.47)$$

$$\mathbf{H}^{ad'}_{i,j,k+\frac{1}{2}} = S_{k+\frac{1}{2}} \max\left[0,\ \min\left(\left|\mathbf{H}^{ad}_{i,j,k+\frac{1}{2}}\right|, S_{k+\frac{1}{2}}\left(\widetilde{\mathbf{R}}^{z}_{i,j,k} - \widetilde{\mathbf{R}}^{z}_{i,j,k-1}\right), S_{k+\frac{1}{2}}\left(\widetilde{\mathbf{R}}^{z}_{i,j,k+2} - \widetilde{\mathbf{R}}^{z}_{i,j,k+1}\right)\right)\right]. \quad (3.48)$$

4. Calculate the total incoming and outgoing antidiffusive fluxes in each cell by combining the prelimited antidiffusive fluxes in each direction in step 3.

$$\begin{aligned}\mathbf{F}^{\text{in}}_{i,j,k} = &\ \max\left(\mathbf{F}^{ad'}_{i-\frac{1}{2},j,k}, 0\right) - \min\left(\mathbf{F}^{ad'}_{i+\frac{1}{2},j,k}, 0\right) \\ + &\ \max\left(\mathbf{G}^{ad'}_{i,j-\frac{1}{2},k}, 0\right) - \min\left(\mathbf{G}^{ad'}_{i,j+\frac{1}{2},k}, 0\right) \\ + &\ \max\left(\mathbf{H}^{ad'}_{i,j,k-\frac{1}{2}}, 0\right) - \min\left(\mathbf{H}^{ad'}_{i,j,k+\frac{1}{2}}, 0\right)\end{aligned} \quad (3.49)$$

$$\begin{aligned}\mathbf{F}^{\text{out}}_{i,j,k} = &\ \max\left(\mathbf{F}^{ad'}_{i+\frac{1}{2},j,k}, 0\right) - \min\left(\mathbf{F}^{ad'}_{i-\frac{1}{2},j,k}, 0\right) \\ &+ \max\left(\mathbf{G}^{ad'}_{i,j+\frac{1}{2},k}, 0\right) - \min\left(\mathbf{G}^{ad'}_{i,j-\frac{1}{2},k}, 0\right) \\ &+ \max\left(\mathbf{H}^{ad'}_{i,j,k+\frac{1}{2}}, 0\right) - \min\left(\mathbf{H}^{ad'}_{i,j,k-\frac{1}{2}}, 0\right)\end{aligned} \tag{3.50}$$

5. Calculate allowed extrema $\mathbf{R}^{\min}$ and $\mathbf{R}^{\max}$ in each cell by comparing with the neighboring cells,

$$\mathbf{R}^{\min} = \min\left(\widetilde{\mathbf{R}}_{i-1,j,k}, \widetilde{\mathbf{R}}_{i,j-1,k}, \widetilde{\mathbf{R}}_{i,j,k-1}, \widetilde{\mathbf{R}}_{i,j,k}, \widetilde{\mathbf{R}}_{i+1,j,k}, \widetilde{\mathbf{R}}_{i,j+1,k}, \widetilde{\mathbf{R}}_{i,j,k+1}\right), \tag{3.51}$$

$$\mathbf{R}^{\max} = \max\left(\widetilde{\mathbf{R}}_{i-1,j,k}, \widetilde{\mathbf{R}}_{i,j-1,k}, \widetilde{\mathbf{R}}_{i,j,k-1}, \widetilde{\mathbf{R}}_{i,j,k}, \widetilde{\mathbf{R}}_{i+1,j,k}, \widetilde{\mathbf{R}}_{i,j+1,k}, \widetilde{\mathbf{R}}_{i,j,k+1}\right). \tag{3.52}$$

6. Compute the ratio of the incoming and outgoing antidiffusive fluxes that are allowed to be applied to each cell versus the total incoming and outgoing antidiffusive fluxes computed in step 4.

$$\mathbf{f}^{\text{in}}_{i,j,k} = \left(\mathbf{R}^{\max}_{i,j,k} - \widetilde{\mathbf{R}}_{i,j,k}\right) / \mathbf{F}^{\text{in}}_{i,j,k}, \tag{3.53}$$

$$\mathbf{f}^{\text{out}}_{i,j,k} = \left(\widetilde{\mathbf{R}}_{i,j,k} - \mathbf{R}^{\min}_{i,j,k}\right) / \mathbf{F}^{\text{out}}_{i,j,k}. \tag{3.54}$$

7. Correct the antidiffusive fluxes in each direction computed in step 3 using the ratio in step 6 so that it does not create either an undershoot in the cell it is

leaving from or an overshoot in the cell it is entering.

$$\mathbf{F}^{\mathrm{C}}_{i+\frac{1}{2},j,k} = \mathbf{F}^{ad'}_{i+\frac{1}{2},j,k} \times \begin{cases} \min\left(\mathbf{f}^{\mathrm{out}}_{i,j,k}, \mathbf{f}^{\mathrm{in}}_{i+1,j,k}, 1\right), & \text{if } \mathbf{F}^{ad'}_{i+\frac{1}{2},j,k} \geq 0; \\ \min\left(\mathbf{f}^{\mathrm{in}}_{i,j,k}, \mathbf{f}^{\mathrm{out}}_{i+1,j,k}, 1\right), & \text{otherwise;} \end{cases} \tag{3.55}$$

$$\mathbf{G}^{\mathrm{C}}_{i,j+\frac{1}{2},k} = \mathbf{G}^{ad'}_{i,j+\frac{1}{2},k} \times \begin{cases} \min\left(\mathbf{f}^{\mathrm{out}}_{i,j,k}, \mathbf{f}^{\mathrm{in}}_{i,j+1,k}, 1\right), & \text{if } \mathbf{F}^{ad'}_{i,j+\frac{1}{2},k} \geq 0; \\ \min\left(\mathbf{f}^{\mathrm{in}}_{i,j,k}, \mathbf{f}^{\mathrm{out}}_{i,j+1,k}, 1\right), & \text{otherwise;} \end{cases} \tag{3.56}$$

$$\mathbf{H}^{\mathrm{C}}_{i,j,k+\frac{1}{2}} = \mathbf{H}^{ad'}_{i,j,k+\frac{1}{2}} \times \begin{cases} \min\left(\mathbf{f}^{\mathrm{out}}_{i,j,k}, \mathbf{f}^{\mathrm{in}}_{i,j,k+1}, 1\right), & \text{if } \mathbf{F}^{ad'}_{i,j,k+\frac{1}{2}} \geq 0; \\ \min\left(\mathbf{f}^{\mathrm{in}}_{i,j,k}, \mathbf{f}^{\mathrm{out}}_{i,j,k+1}, 1\right), & \text{otherwise;} \end{cases} \tag{3.57}$$

With the corrected fluxes, the final solution can now be calculated by Eq. 3.5.

The FCT algorithm described so far uses first-order, Euler explicit for time integration to update the solution. This is so that the FCT algorithm can be coupled with the implicit time integration described in the following chapter. If only explicit time integration is needed, we recommend using the second-order time integration described in Section 3 of [106].

3.3 Stability Analysis

In the original LCPFCT [106], the diffusion and antidiffusion coefficients were given in a 1D form as

$$\nu^{(1)}_{i+\frac{1}{2}} = \frac{1}{6} + \frac{1}{3}\epsilon^2_{i+\frac{1}{2}}, \tag{3.58}$$

$$\nu^{(2)} = 0, \tag{3.59}$$

$$\mu_{i+\frac{1}{2}} = \frac{1}{6} - \frac{1}{6}\epsilon^2_{i+\frac{1}{2}}. \tag{3.60}$$

These values were selected to reduce the phase errors in convection to fourth order. We initially implemented these values and performed several test problem in 2D and 3D low-speed vortex flows (the setup for these problems are described in Chapter 5). The calculations are stable in 2D using these values. In 3D, however, "checkerboarding" was observed in the flow field, suggesting that the calculation was numerically unstable. When using small time steps within the explicit stability limit, the numerical instabilities appeared but grew slowly. When using large time steps allowed by implicit integration (the method is described in Chapter 4), the numerical instabilities grew rapidly. For the 3D vortex flows we tested, the smaller the Reynolds (Re) number was, the larger the numerical oscillations were. This trend suggested that with more diffusion, the algorithm became more unstable. This led us to suspect that the numerical diffusion $\nu^{(1)}$ added during the diffusion stage in LCPFCT was too much for 3D calculations. To solve this issue of numerical instability in 3D, we perform Fourier stability analysis for both the 2D and 3D LCPFCT

version of FCT.

To perform the Fourier stability analysis, first consider the generalized conservation equation (Eq. 3.1). We assume that the source term $\mathbf{D_4}$ is 0, that $\mathbf{D_1}, \mathbf{D_2}, \mathbf{D_3}$ are constant, and the velocities u, v, and w are constant. Then Eq. 3.1 reduces to

$$\frac{\partial \mathbf{R}}{\partial t} = -\frac{\partial \mathbf{K_1}}{\partial x} - \frac{\partial \mathbf{K_2}}{\partial y} - \frac{\partial \mathbf{K_3}}{\partial z}, \tag{3.61}$$

whose analytic solution is

$$\mathbf{R}(x, y, z, t) = \mathbf{R}(x - ut, y - vt, z - wt, 0). \tag{3.62}$$

The solution is a propagating wave with velocity (u, v, w). We assume periodic boundary conditions and a spatial harmonic as the initial value. Equation 3.60 can be solved by separation of variables and it has wave solutions of the form:

$$\mathbf{R}(x, y, z, t) = e^{-i\omega t} e^{i(kx+ly+mz)}, \tag{3.63}$$

where the frequency ω and wave numbers k, l, m follow a dispersion relation $\omega = uk + vl + wm$.

When numerically solving Eq. 3.60 using FCT, the flow property is convected from the old time step $\mathbf{R}^o_{i,j,k}$ to a new time step $\mathbf{R}^n_{i,j,k}$ using the procedure listed above. To ensure stability, we need the new solution to not grow unbounded in

time, that is

$$\left|\frac{\mathbf{R}^n_{i,j,k}}{\mathbf{R}^o_{i,j,k}}\right| \leq 1. \tag{3.64}$$

As a reminder, in the FCT procedure, the final solution (Eq. 3.5) consists of two parts which are the convected and diffused low-order solution and an added corrected flux. The corrected flux is calculated through a flux limiter as in Eqs. 3.46-3.48, which prevents overshoots and undershoots so that no oscillation will be created. Therefore, the added corrected flux is inherently stable and as long as the low-order solution is also stable, we should have a stable algorithm under all conditions. Therefore, the stability criterion reduces to

$$\left|\frac{\widetilde{\mathbf{R}}_{i,j,k}}{\mathbf{R}^o_{i,j,k}}\right| \leq 1. \tag{3.65}$$

We can substitute the solution at $t = t^o$ using the form in Eq. 3.63 into the low-order solution and then check if the resulting ratio $\widetilde{\mathbf{R}}_{i,j,k}/\mathbf{R}^o_{i,j,k}$ meets the stability criterion in Eq. 3.65.

3.3.1 Two Dimensions (2D)

To determine if the stability criterion in Eq. 3.65 is satisfied in 2D, we first set all of the terms associated with the variable z to zero in Eqs. 3.60 - 3.64. Here we list the procedure to calculate the low-order solution in 2D, which consists of the convection (transport) stage and the diffusion stage.

- The convection (transport, T) stage is expressed as

$$\begin{aligned}\mathbf{R}_{i,j}^{T} = \mathbf{R}_{i,j}^{o} &- \frac{\epsilon_x}{2}\left(\mathbf{R}_{i+1,j}^{o} - \mathbf{R}_{i-1,j}^{o}\right) \\ &- \frac{\epsilon_y}{2}\left(\mathbf{R}_{i,j+1}^{o} - \mathbf{R}_{i,j-1}^{o}\right),\end{aligned} \tag{3.66}$$

  where we define

$$\epsilon_x = \frac{u\Delta t}{\Delta x}, \epsilon_y = \frac{v\Delta t}{\Delta y}. \tag{3.67}$$

- The convection (transport) with diffusion (TD) stage is expressed as

$$\begin{aligned}\widetilde{\mathbf{R}}_{i,j} = \mathbf{R}_{i,j}^{o} &- \frac{\epsilon_x}{2}\left(\mathbf{R}_{i+1,j}^{o} - \mathbf{R}_{i-1,j}^{o}\right) \\ &- \frac{\epsilon_y}{2}\left(\mathbf{R}_{i,j+1}^{o} - \mathbf{R}_{i,j-1}^{o}\right) \\ &+ \nu_x\left(\mathbf{R}_{i-1,j}^{o} - 2\mathbf{R}_{i,j}^{o} + \mathbf{R}_{i+1,j}^{o}\right) \\ &+ \nu_y\left(\mathbf{R}_{i,j-1}^{o} - 2\mathbf{R}_{i,j}^{o} + \mathbf{R}_{i,j+1}^{o}\right)\end{aligned} \tag{3.68}$$

  Here ν_x and ν_y are the diffusion coefficients. Their original values in [106] were given as Eq. 3.58.

Now we write the flow property $\mathbf{R}_{i,j}^{o}$ at initial time t^o at grid point (i, j) using the wave solutions in Eq. 3.63 in a finite difference form as

$$\mathbf{R}_{i,j}^{o} = e^{-i\omega t^o} e^{ik\Delta xI} e^{il\Delta yJ}. \tag{3.69}$$

The flow property at grid point $(i+n_1, j+n_2)$ can then be written as

$$\mathbf{R}^o_{i+n_1,j+n_2} = e^{-i\omega t^o} e^{ik\Delta x(I+n_1)} e^{il\Delta y(J+n_2)}. \tag{3.70}$$

Here we define the phase angle $k\Delta x = \alpha$ and $l\Delta y = \beta$, for simplicity in notation. We can then substitute Eq. 3.70 into the ratio $T^{TD} = \frac{\widetilde{\mathbf{R}}_{i,j}}{\mathbf{R}^o_{i,j}}$ and simplify it as

$$\begin{aligned} T^{TD} = 1 &- \frac{\epsilon_x}{2}\left(e^{i\alpha} - e^{-i\alpha}\right) \\ &- \frac{\epsilon_y}{2}\left(e^{i\beta} - e^{-i\beta}\right) \\ &+ \nu_x\left(e^{-i\alpha} - 2 + e^{i\alpha}\right) \\ &+ \nu_y\left(e^{-i\beta} - 2 + e^{i\beta}\right). \end{aligned} \tag{3.71}$$

Equivalently, Eq. 3.70 can also be written as

$$\begin{aligned} T^{TD} = 1 &- i\epsilon_x \sin\alpha - i\epsilon_y \sin\beta \\ &+ 2\nu_x\left(\cos\alpha - 1\right) + 2\nu_y\left(\cos\beta - 1\right) \end{aligned} \tag{3.72}$$

To determine if the low-order solution is stable, we calculate the amplitude of T^{TD} and compare it with unity. Here we assume the phase angle α equals to β for simplicity and they both have a range of $[0, \pi]$. Based on Eq. 3.66, ϵ_x and ϵ_y are functions of the time step Δt and their sum is the Courant-Friedrich-Lewy (CFL) number in 2D for a Cartesian mesh. This is expressed as

$$\epsilon_x + \epsilon_y = \frac{u\Delta t}{\Delta x} + \frac{v\Delta t}{\Delta y} = \mathrm{CFL}_{2\mathrm{D}}. \tag{3.73}$$

Therefore, we can substitute Eq. 3.58 for ν_x and ν_y into Eq. 3.71 and calculate the amplitude of T^{TD} as a function of phase angle for all CFL_{2D} numbers. The result is shown in Fig. 3.1. We can see that the amplitude of T^{TD} is smaller than unity for all CFL_{2D} numbers at all phase angles. This shows that the 2D low-order solution is unconditionally stable.

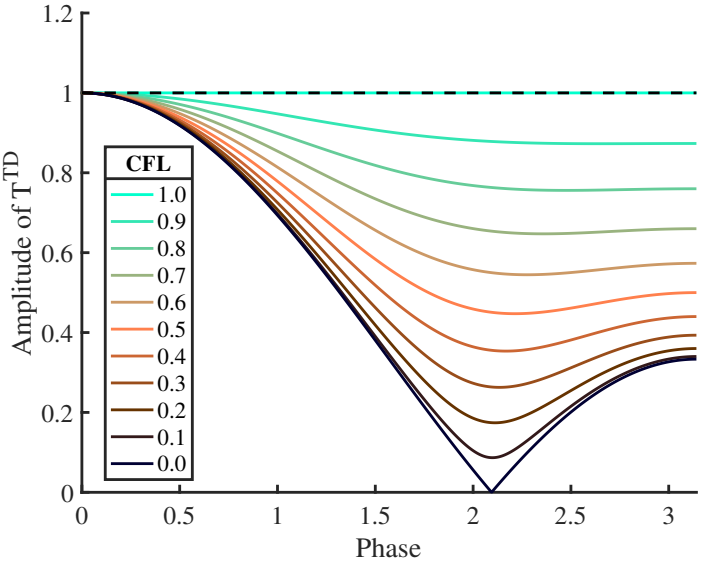

Figure 3.1: Stability plot of the 2D low-order (convected and diffused) solution as a function of phase for all CFL numbers. The diffusion coefficients here use the value in Eq. 3.58, which is the original value given in [106].

3.3.2 Three Dimensions (3D)

We now check the stability of the low-order solution in 3D. Similar to 2D, we repeat the procedures to calculate the low-order solution:

- The convection (transport, T) stage is expressed as

$$\begin{aligned}\mathbf{R}^{T}_{i,j,k} = \mathbf{R}^{o}_{i,j,k} &- \frac{\epsilon_x}{2}\left(\mathbf{R}^{o}_{i+1,j,k} - \mathbf{R}^{o}_{i-1,j,k}\right) \\ &- \frac{\epsilon_y}{2}\left(\mathbf{R}^{o}_{i,j+1,k} - \mathbf{R}^{o}_{i,j-1,k}\right) \\ &- \frac{\epsilon_z}{2}\left(\mathbf{R}^{o}_{i,j,k+1} - \mathbf{R}^{o}_{i,j,k-1}\right),\end{aligned} \tag{3.74}$$

where we define

$$\epsilon_x = \frac{u\Delta t}{\Delta x}, \epsilon_y = \frac{v\Delta t}{\Delta y}, \text{ and } \epsilon_z = \frac{w\Delta t}{\Delta z}. \tag{3.75}$$

- The convection (transport) with diffusion (TD) stage is expressed as

$$\begin{aligned}\widetilde{\mathbf{R}}_{i,j,k} = \mathbf{R}^{o}_{i,j,k} &- \frac{\epsilon_x}{2}\left(\mathbf{R}^{o}_{i+1,j,k} - \mathbf{R}^{o}_{i-1,j,k}\right) \\ &- \frac{\epsilon_y}{2}\left(\mathbf{R}^{o}_{i,j+1,k} - \mathbf{R}^{o}_{i,j-1,k}\right) \\ &- \frac{\epsilon_z}{2}\left(\mathbf{R}^{o}_{i,j,k+1} - \mathbf{R}^{o}_{i,j,k-1}\right) \\ &+ \nu_x\left(\mathbf{R}^{o}_{i-1,j,k} - 2\mathbf{R}^{o}_{i,j,k} + \mathbf{R}^{o}_{i+1,j,k}\right) \\ &+ \nu_y\left(\mathbf{R}^{o}_{i,j-1,k} - 2\mathbf{R}^{o}_{i,j,k} + \mathbf{R}^{o}_{i,j+1,k}\right) \\ &+ \nu_z\left(\mathbf{R}^{o}_{i,j,k-1} - 2\mathbf{R}^{o}_{i,j,k} + \mathbf{R}^{o}_{i,j,k+1}\right)\end{aligned} \tag{3.76}$$

Here ν_x, ν_y, and ν_z are the diffusion coefficients. Their original values in [106] were given as Eq. 3.58.

Now we write the flow property $\mathbf{R}^{o}_{i,j,k}$ at the initial time t^o at grid point (i, j, k)

using the wave solutions in Eq. 3.63 in a finite difference form as

$$\mathbf{R}^{o}_{i,j,k} = e^{-i\omega t^{o}} e^{ik\Delta x I} e^{il\Delta y J} e^{im\Delta z K}. \tag{3.77}$$

The flow property at grid point $(i+n_1, j+n_2, k+n_3)$ can then be written as

$$\mathbf{R}^{o}_{i+n_1,j+n_2,k+n_3} = e^{-i\omega t^{o}} e^{ik\Delta x(I+n_1)} e^{il\Delta y(J+n_2)} e^{im\Delta z(K+n_3)}. \tag{3.78}$$

Here we define the phase angle $k\Delta x = \alpha$, $l\Delta y = \beta$, and $m\Delta z = \gamma$ for simplicity in notation. We can then substitute Eq. 3.77 into the ratio $T^{TD} = \frac{\tilde{\mathbf{R}}_{i,j,k}}{\mathbf{R}^{o}_{i,j,k}}$ and simplify it as

$$\begin{aligned} T^{TD} = 1 &- \frac{\epsilon_x}{2}\left(e^{i\alpha} - e^{-i\alpha}\right) \\ &- \frac{\epsilon_y}{2}\left(e^{i\beta} - e^{-i\beta}\right) \\ &- \frac{\epsilon_z}{2}\left(e^{i\gamma} - e^{-i\gamma}\right) \\ &+ \nu_x\left(e^{-i\alpha} - 2 + e^{i\alpha}\right) \\ &+ \nu_y\left(e^{-i\beta} - 2 + e^{i\beta}\right) \\ &+ \nu_z\left(e^{-i\gamma} - 2 + e^{i\gamma}\right). \end{aligned} \tag{3.79}$$

Equivalently, Eq. 3.79 can also be written as

$$\begin{aligned} T^{TD} = 1 &- i\epsilon_x \sin\alpha - i\epsilon_y \sin\beta - i\epsilon_z \sin\gamma \\ &+ 2\nu_x\left(\cos\alpha - 1\right) + 2\nu_y\left(\cos\beta - 1\right) + 2\nu_z\left(\cos\gamma - 1\right) \end{aligned} \tag{3.80}$$

To determine if the low-order solution is stable, we now calculate the amplitude of T^{TD} and compare it with unity. Here we assume the phase angle α, β and γ are equal to each other for simplicity and that they all have a range of $[0, \pi]$. Based on Eq. 3.75, ϵ_x, ϵ_y, and ϵ_z are functions of the time step Δt and their sum is the Courant-Friedrich-Lewy (CFL) number in 3D for a Cartesian mesh.

$$\epsilon_x + \epsilon_y + \epsilon_z = \frac{u\Delta t}{\Delta x} + \frac{v\Delta t}{\Delta y} + \frac{w\Delta t}{\Delta z} = \mathrm{CFL}_{3\mathrm{D}}. \tag{3.81}$$

Therefore, we can substitute Eq. 3.58 for ν_x, ν_y, and ν_z into Eq. 3.71 and calculate the amplitude of T^{TD} as a function of phase angle for all $\mathrm{CFL}_{3\mathrm{D}}$ numbers. The result is shown in Fig. 3.2. We can see that when $\mathrm{CFL}_{3\mathrm{D}}$ is equal to 0, the amplitude of T^{TD} is on the edge of unity, the stability limit, at the phase angle of π. When $\mathrm{CFL}_{3\mathrm{D}}$ is slightly larger than 0, the amplitude of T^{TD} is larger than unity for large phase angles, which is beyond the stability limit. The larger the $\mathrm{CFL}_{3\mathrm{D}}$ is, the larger the amplitude of T^{TD} becomes, and a larger range of phase angles contributes to instability. This shows that the 3D low-order solution is unstable for any $\mathrm{CFL}_{3\mathrm{D}}$ that is larger than 0 when using the diffusion coefficients in Eq. 3.58 .

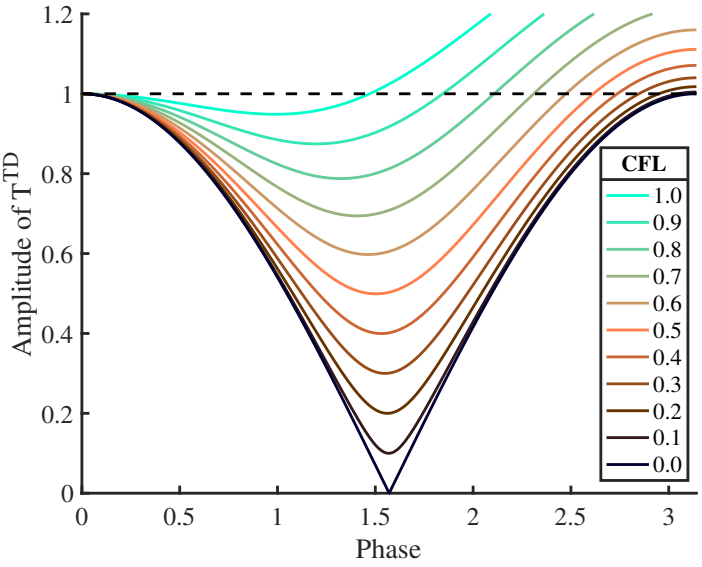

Figure 3.2: Stability plot of the 3D low-order (convected and diffused) solution as a function of phase for all CFL numbers. The diffusion coefficients here use the value in Eq. 3.58, which is the original value given in [106].

Now we isolate the source of instability in 3D. We consider the worst phase angle, $\alpha = \beta = \gamma = \pi$, which gives the most instability. We also consider the condition where the diffusion coefficients ν_x, ν_y, and ν_z are equal in all directions. Then the amplitude of T^{TD} can be calculated as

$$\begin{aligned}\left|T^{TD}\right|^2 &= \left(1 + 2\nu_x\left(\cos\alpha - 1\right) + 2\nu_y\left(\cos\beta - 1\right) + 2\nu_z\left(\cos\gamma - 1\right)\right)^2 + \left(\sin\alpha + \sin\beta + \sin\gamma\right)^2 \\ &= \left(1 + 3 \times 2\nu_x\left(\cos\alpha - 1\right)\right)^2 + \left(3 \times \sin\alpha\right)^2 \\ &= \left(1 + 6\nu_x\left(\cos\alpha - 1\right)\right)^2 + \left(3\sin\alpha\right)^2 .\end{aligned} \tag{3.82}$$

Substituting $\alpha = \pi$ into the equation above gives

$$\left|T^{TD}\right|^2 = (1 - 12\nu_x)^2. \tag{3.83}$$

Then substituting the value of ν_x in Eq. 3.58 into the equation above gives

$$\begin{aligned} \left|T^{TD}\right|^2 &= \left(1 - 12\left(\underline{\frac{1}{6}} + \frac{1}{3}\epsilon_x^2\right)\right)^2 \\ &= \left(1 - \underline{2} - 4\epsilon_x^2\right)^2 \\ &= \left(-1 - 4\epsilon_x^2\right)^2 \\ &= \left(1 + 4\epsilon_x^2\right)^2 \end{aligned} \tag{3.84}$$

This indicates that $\left|T^{TD}\right|$ is always larger than unity as long as ϵ_x is not equal to 0, meaning the low-order solution is always unstable. If we examine the steps in Eq. 3.84, we can see that the absolute instability comes from the underlined values. Decreasing these values could decrease $\left|T^{TD}\right|$ below unity. The solution would then be stable for some non-zero values of ϵ_x.

3.4 One Method for Stabilizing FCT in 3D

From the stability analysis above, we learned that the instability in 3D LCPFCT comes from the diffusion coefficient added during the diffusion stage. One way to stabilize FCT in 3D is to decrease the value of the constant in the diffusion coefficient in Eq. 3.58. As mentioned above, the diffusion and antidiffusion coefficients in Eqs. 3.58 - 3.60 were designed together to give fourth-order accuracy in phase and

amplitude [106, 108]. If we change the diffusion coefficient for stability, the total amount of diffusion and antidiffusion should be kept the same in the final solution to retain this accuracy. Therefore, one way to stabilize FCT in 3D is to split the amount of diffusion into two parts: $\nu^{(1)}$ and $\nu^{(2)}$. Keep $\nu^{(1)}$ in the diffusion stage and assign to it a value that maintains stability for the low-order solution (described in Eqs. 3.24 - 3.26) and then add the residual diffusion $\nu^{(2)}$ back to the solution at the antidiffusion stage (described in Eqs. 3.36 - 3.38). In this way, the excessive amount of diffusion which initially made the 3D solution unstable can now be limited by the flux limiter (Eqs. 3.46- 3.48) to prevent any numerical oscillations.

The values of $\nu^{(1)}$ and $\nu^{(2)}$ we selected in this work for a stable 3D FCT algorithm are listed in Eqs. 3.27 - 3.29 and 3.42. The sum of $\nu^{(1)}$ and $\nu^{(2)}$ is equal to the original ν in Eq. 3.58. The antidiffusion coefficient we use in this work is same as the original, which is in Eq. 3.60.

Now let us check the stability of the new 3D FCT with the new diffusion coefficients $\nu^{(1)}$ and $\nu^{(2)}$. Similar to before, we check the amplitude of T_{TD} and compare it with unity. All of the steps for calculating $\left|T^{TD}\right|$ from Eq. 3.75 to 3.85 still apply, except the diffusion coefficients should be changed to $\nu^{(1)}$. For example, Eq. 3.85 now becomes

$$\begin{aligned} T^{TD} = 1 - i\epsilon_x \sin\alpha - i\epsilon_y \sin\beta - i\epsilon_z \sin\gamma \\ + 2\nu_x^{(1)} (\cos\alpha - 1) + 2\nu_y^{(1)} (\cos\beta - 1) + 2\nu_z^{(1)} (\cos\gamma - 1) \end{aligned} \tag{3.85}$$

We substitute the values of $\nu^{(1)}$ in Eqs. 3.27 - 3.29 in the equation above and also

assume the phase α, β, and γ are equal to each other. The amplitude of T_{TD} as a function of phase for all $\text{CFL}_{3\text{D}}$ numbers is shown in Fig. 3.3. We can see that the amplitude of T_{TD} is now smaller than unity, showing that the low-order solution is stable for all phase angles when $\text{CFL}_{3\text{D}}$ is less than 0.8. There is still however, a range of phase that contributes to instabilities when $\text{CFL}_{3\text{D}}$ is larger than 0.8. The stability limit of $\text{CFL}_{3\text{D}} < 0.8$ should not impose serious constraints on the time-step size in both explicit and implicit calculations.

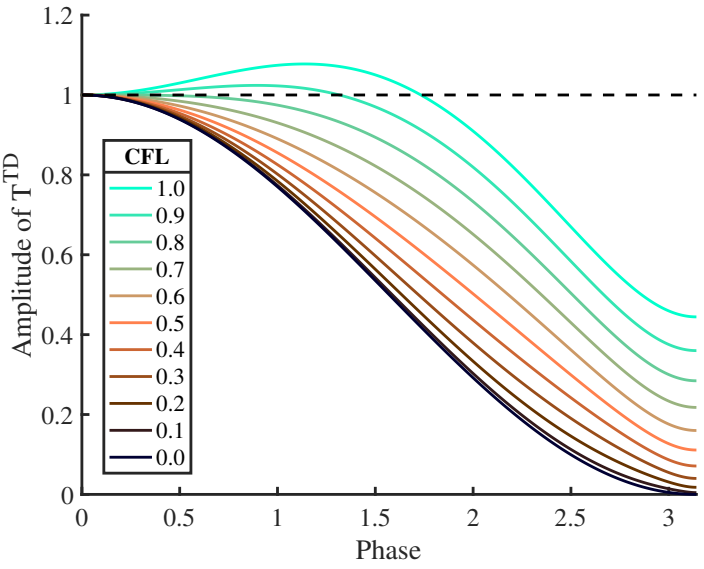

Figure 3.3: Stability plot of the 3D low-order (convected and diffused) solution as a function of phase for all CFL numbers. The diffusion coefficients here use the value in Eqs. 3.27 - 3.29.

Chapter 4: Numerical Algorithm - Barely Implicit Correction (BIC)[1]

4.1 Overview

The barely implicit correction (BIC), originally proposed by Patnaik et al. [20], eliminated the sound speed restriction by solving the governing equations at a large time step determined by the fluid velocity (predictor step), and then applying a pressure correction that effectively equilibrates the acoustic waves. More specifically, at each time step, a pressure correction is applied to the momentum and energy equations (corrector step). Patnaik et al. used the flux-corrected transport (FCT) for the predictor step value, although in principle, any monotone algorithm should work just as well.

The original BIC algorithm [20] was used for one-dimensional and two-dimensional problems, and, in particular, for reactive flows. Examples include computations of a premixed cellular flame structure (Patnaik et al. [21]), and simulations of axisymmetric methane-air diffusion flames (Kaplan et al. [22]). These multidimensional reactive-flow computations produced quantitative results when compared to experiments. Nonetheless, there were numerical issues that caused some problems in

[1]This Chapter is a slightly modified version of what has been published in [1] and has been reproduced here with the permission of the copyright holder.

the execution, such as small, sometimes growing pressure oscillations that had to be damped. Patnaik et al. [21] filtered these oscillations from the solutions by using a high-frequency pressure filter. Kaplan et al. [22] reduced oscillations to an acceptable level by using a control algorithm for the outflow boundary condition.

In this work, we develop and extend the BIC algorithm so that it is robust and stable for one-, two-, and three-dimensional viscous flow problems with and without inflow and outflow boundaries. The base monotone algorithm is described in Chapter 3, which is the same used by Patnaik et al. [20]. Here the new procedure for developing the pressure correction is described in detail along with an additional filter step.

We begin by describing the original BIC procedure, and then show how it can be stabilized, and finally generalize the solution to include viscous and other source terms. The convective fluxes will be solved here using the flux-corrected transport algorithm (FCT). In the original version of FCT, there is a two-stage Runge-Kutta time integration, that is, a half time step (marching from t^o to $t^o + \Delta t/2$) and a full time step (from t^o to $t^o + \Delta t$), which together give second-order in time. In the BIC algorithm given below, the original time integration for FCT is combined with a new BIC step, so that there is only one time step (from t^o to $t^o + \Delta t$) required. This is explained below.

4.2 Original Procedure

First consider the original BIC-FCT approach, which solves the Euler equations that can be written as:

$$\frac{\partial \rho}{\partial t} = -\nabla \cdot (\rho \mathbf{V}) \tag{4.1}$$

$$\frac{\partial \rho \mathbf{V}}{\partial t} = -\nabla \cdot (\rho \mathbf{V}\mathbf{V}) - \nabla P \tag{4.2}$$

$$\frac{\partial E}{\partial t} = -\nabla \cdot (E + P)\,\mathbf{V} \tag{4.3}$$

in which t is time, ρ is density, P is pressure, E is total energy, $\mathbf{V}$ is the velocity vector. The equation of state relating pressure and the total energy is

$$E = \frac{P}{\gamma - 1} + \frac{1}{2}\rho \mathbf{V^2} \tag{4.4}$$

The inclusion of body forces and source terms will be discussed later.

The procedure outlined below is *almost* the same as [20]. Here, we repeat and recast the steps to clarify the path towards the solution and to facilitate the explanation of the need for the new step added to ensure stability. This explanation below is also necessary to address the more substantive modifications needed and explained in a later section.

The term "barely implicit correction" is used to indicate that only selected terms in the equations are treated implicitly [109]. This same basic concept as used here means that only the pressure in Eq. 4.2 and velocity in Eq. 4.3 are treated

implicitly. There were two main stages in the algorithm. First, there is an explicit predictor step using a large time-step governed by CFL condition on the fluid velocity (not the acoustic speed) to solve for predicted values. Then there is a second implicit corrector step that solves an elliptic equation for a pressure correction. They also introduced the implicitness parameter, ω, which allows the algorithm to vary from partially implicit (damping of the sound wave is minimized) to fully implicit (damping of the sound wave is maximized).

These two stages are carried out by a four-step procedure. Below, superscripts "o" denotes the old time step and "n" denotes the new time step. The prime represents the predicted values at the end of the predictor step, and these values are then used by the correction step.

1. Solve for predicted density ρ', and momentum $\rho'\mathbf{V}'$:

$$\frac{\rho' - \rho^o}{\Delta t} = -\nabla \cdot \rho^o \mathbf{V}^o \tag{4.5}$$

$$\frac{\rho'\mathbf{V}' - \rho^o\mathbf{V}^o}{\Delta t} = -\nabla \cdot \rho^o \mathbf{V}^o\mathbf{V}^o - \nabla P^o \tag{4.6}$$

   Use a monotone method (here FCT with one-step time integration) to solve for predicted density ρ' and momentum $\rho'\vec{V}'$. The time step Δt is the large time-step from the CFL condition governed by fluid velocity (not sound speed).

2. Solve for intermediate energy $\overline{E}$:

$$\frac{\overline{E} - E^o}{\Delta t} = -\nabla \cdot (E^o + P^o)\left[\omega\mathbf{V}' + (1-\omega)\mathbf{V}^o\right] \tag{4.7}$$

Again, use FCT with the one-step time integration with the same Δt as in step 1 to solve for an intermediate energy $\overline{E}$. The velocity $\mathbf{V}'$ can be calculated by $\rho'\mathbf{V}'/\rho'$. The convective velocity used in this step is a weighted sum of the old and predicted velocity. Note the introduction of the implicitness parameter ω.

3. Solve for pressure correction δP. This is a step introduced for the BIC procedure.

$$\frac{\delta P}{(\gamma-1)\omega\Delta t} - \omega\Delta t\nabla\cdot\left(\frac{E^o+P^o}{\rho'}\right)\nabla\delta P = \frac{\overline{E}-E^o}{\Delta t} - \frac{\rho'\mathbf{V}'^2-\rho^o\mathbf{V}^{o2}}{2\Delta t} \tag{4.8}$$

Substitute in predicted density ρ', velocity $\mathbf{V}'$, intermediate energy $\overline{E}$ and properties at old time step into this elliptic equation to solve for δP, which is defined as $\delta P \equiv \omega\left(P^n - P^o\right)$. Here γ is the ratio of specific heats.

Equation 4.8 was originally derived in [20] by rewriting Eq. 4.2 with the pressure in an implicit form and Eq. 4.3 with the velocity in an implicit form, and combining them into one equation. To solve Eq. 4.8 for a one-dimensional (1D) system, a tridiagonal matrix solver is needed. For a two- or three-dimensional system, an elliptic solver is required. For boundary conditions, the Neumann condition can be applied at symmetry, no-slip wall, or outflow (zero-gradient) boundaries. If the internal energy is constant at a physical boundary, then the pressure at this boundary is constant according to the equation of state. Therefore a Dirichlet condition ($\delta P = 0$) can be applied as the pressure does not vary. If the internal energy varies at a physical boundary, then the bound-

ary condition for δP can be derived as a function of the internal energy based on the equation of state.

4. Correct the momentum and energy using δP:

$$\rho^n \mathbf{V}^n = \rho' \mathbf{V}' - \Delta t \nabla \delta P \tag{4.9}$$

$$e^n = \frac{\delta P}{(\gamma - 1)\omega} + e^o \tag{4.10}$$

Since the density equation was not treated implicitly, the density at a new time step is equal to the predicted density, that is $\rho^n = \rho'$. Equation 4.9 and 4.10 were given in [20]. Here e represents the total internal energy. Exactly how to update the kinetic energy was not described in the original paper.

Using steps 1-4, we were able to reproduce the two original 1D test problems, which were advection of a contact discontinuity and damping of a sound wave [20]. These two tests involved solution of the Euler equations only. Then, we attempted to use the algorithm as given above to solve the full Navier-Stokes equations by including the diffusion terms that were added through straightforward time-step splitting. The result showed there was a growing, unbounded instability in the solution that could be traced to the coupling with the diffusion terms as well as effects from open boundary conditions.

Simulations of a 2D double shear layer with periodic boundaries on all sides were used to isolate the issues with the additional viscous diffusion terms. The simulations showed the evolution of the two shear layers rolling into large vorticies

due to an initial sinusoidal velocity perturbation. The implicit calculation ran, but with strong unphysical oscillations in the temperature and density.

Simulations of a 3D columnar vortex were performed using an inflow boundary with open boundaries on all other sides of the domain. The results showed uncontrolled oscillations and was completely unbounded after only a few time-steps. This type of outflow boundary problem was also encountered by Patnaik et al. [21] and Kaplan et al. [22]. The issue of how to stabilize an outflow will be discussed in more detail below.

4.3 New Solution Procedure

In order to stabilize the algorithm, we first need to isolate the cause of the instability. This leads us to change our focus from pure convection (Euler equations) to additional physical processes that occur in a flow. When numerically solving the full Navier-Stokes equations using explicit time schemes, timestep-splitting is often used. This means each physical process, that is convection, diffusion, and chemical reactions, is calculated serially in one time step. Then the solutions of all the individual processes are summed, effectively coupling all the physical processes to advance in time. This method, in theory, is correct for small time steps and it works well when using explicit time integration for convection, or when the changes in variables are not significant in one time step. When using implicit algorithms such as BIC, however, the large time step may cause large changes in momentum and energy due to diffusion or reaction (if there is chemical heat release, which will be

addressed in a later work). Since the original BIC algorithm was only applied to the convection stage, the changes in momentum and energy from the other physical processes were not explicitly accounted for in the pressure correction. This mismatch is what was causing the instability issue. The pressure-correction procedure has to be modified, in some way to include the changes from other physical processes.

One approach was given in the most recent document of the BIC algorithm [23]. An extra term S was included in the energy equation (Eq. 4.7) as a source term, and this formed the new equation for the intermediate energy:

$$\frac{\overline{E} - E^o}{\Delta t} = -\nabla \cdot (E^o + P^o) \left[\omega \mathbf{V}' + (1-\omega)\mathbf{V}^o\right] + S \tag{4.11}$$

This term S serves as a "storage" variable which accumulates the change of total internal energy due to diffusion and other processes. Then using this new expression for $\left(\overline{E} - E^o\right)/\Delta t$, the effects of S are then fed into the elliptic equation, Eq. 4.8. Now δP includes the effects of energy change in all of the physical processes considered.

Then, step 4, which is the correction of momentum, energy and pressure, was given by [23] as:

$$\rho^n \mathbf{V}^n = \rho' \mathbf{V}' - \Delta t \nabla \delta P \tag{4.12}$$

$$E^n = \frac{\delta P}{(\gamma - 1)\omega} + E^o \tag{4.13}$$

$$P^n = P^o + \delta P \tag{4.14}$$

This update of variables, however, introduces two inconsistencies. The first is

in the kinetic energy computed from the updated momentum $\rho^n \mathbf{V}^n$ and updated total energy of Eq. 4.13. This inconsistency manifests itself because the new pressure correction is applied to the old total energy, which does not account for the relatively large new kinetic energy. We show this mismatch by first expanding the old total energy E^o,

$$E^o = \frac{P^o}{\gamma - 1} + \frac{1}{2}\rho^o \mathbf{V}^{o2}. \tag{4.15}$$

The old total energy is expressed as a sum of the internal and the kinetic energies, with the internal energy written using the equation of state. We then incorporate the pressure correction by substituting Eq. 4.15 into Eq. 4.13. Rearranging then gives:

$$E^n = \frac{\omega P^o + \delta P}{(\gamma - 1)\omega} + \frac{1}{2}\rho^o \mathbf{V}^{o2} \tag{4.16}$$

which means only the internal energy is updated with the pressure correction term, and the kinetic energy does not change from its value at the old time step. The momentum, however, is updated according to Eq. 4.12. This mismatch violated conservation and we observed that this asynchronism generated nonphysical pressure waves within large momentum gradient regions.

We now introduce one modification to the kinetic energy correction to address

the mismatch of energies. We replace Eq. 4.13 at step 4 with:

$$E^n = \frac{\omega P^o + \delta P}{(\gamma - 1)\omega} + \frac{1}{2}\rho^n \mathbf{V}^{n2} \tag{4.17}$$

This corrects the kinetic energy from the updated momentum $\rho^n \mathbf{V}^n$. The velocity at the new time step $\mathbf{V}^n$ can be calculated by $\rho^n \mathbf{V}^n / \rho^n$.

The second inconsistency is in Eq. 4.14, which does not account for the implicitness ω. The corrected form is written as:

$$P^n = P^o + \delta P / \omega. \tag{4.18}$$

Although adding the extra term S helps account for all the physical processes in the pressure correction, oscillations in pressure still arises when the time step is very large. Large implicit time steps result in regions with strong energy source, and when such a region is under-resolved, numerical instabilities occur and eventually grow unbounded if left unchecked. These oscillations decrease as the time step decreases, and they are effectively gone when the time step is close to a usual explicit time step. Two approaches are often used to suppress such numerical instabilities. These are artificial dissipation by including additional damping terms in the equations [110, 111], and more efficiently, spatial filtering which does not affect the main physical gradients in the flow [112, 113, 114, 115]. A high-frequency pressure filter

is suggested for BIC in [23] to avoid the oscillations:

$$P^{filtered} = P + \alpha \nabla^4 P \tag{4.19}$$

in which α is a small constant. It was, however, necessary to determine the optimal α on a case-by-case basis, and the filter violates conservation.

Here we eliminate high-frequency oscillations and maintain physical structures and conservation by implementing an extra FCT step [116]. The monotone property of FCT allows for it to act as a high-frequency filter. We use this extra step by passing the conservative variables calculated from step 4 ($\rho^n, \rho^n \mathbf{V}^n$ and E^n) into the FCT routine as inputs, while forcing the convective velocities and all pressure and source terms to be zero. This means no additional convection or pressure work in a computational cell is performed. Furthermore, because all the conservative variables are filtered, this procedure preserves conservation. In our usage, we find that this filter is applicable to most cases without extra tuning or optimizing.

4.4 Coupling BIC with Diffusion Processes

So far, we have shown how to use BIC to solve for convective fluxes. To obtain the complete solution to the full set of Navier-Stokes equations, the diffusion processes need to be modeled and included. Here we couple the diffusion with the convection process through time-step splitting procedure mentioned above. This means that, in one time step, the diffusion and convection fluxes are calculated independently, and each process uses the solution from the previous process as

initial conditions. There are three major considerations for using time-step splitting, especially when the convection process uses an implicit method. These are: (1) time-step control, (2) the order in which of each physical process is computed, and (3) when and how to update variables. The exact way the processes are updated is explained in detail below.

4.4.1 Governing Equations

We consider the time-dependent, compressible Navier-Stokes equations :

$$\frac{\partial \rho}{\partial t} = -\nabla \cdot (\rho \mathbf{V}) \tag{4.20}$$

$$\frac{\partial (\rho \mathbf{V})}{\partial t} = -\nabla \cdot (\rho \mathbf{V}\mathbf{V}) - \nabla P - \nabla \cdot \hat{\tau} \tag{4.21}$$

$$\frac{\partial E}{\partial t} = -\nabla \cdot ((E + P)\,\mathbf{V}) - \nabla \cdot (\mathbf{V} \cdot \hat{\tau}) - \nabla \cdot (K \nabla T) \tag{4.22}$$

$$\hat{\tau} = \rho\nu \left(\frac{2}{3} (\nabla \cdot \mathbf{V})\,\mathbf{I} - (\nabla \mathbf{V}) - (\nabla \mathbf{V})^{\dagger} \right) \tag{4.23}$$

where T is temperature, K is thermal conductivity, I is the identity matrix, $\hat{\tau}$ is the stress tensor. Superscript † denotes the transpose for a matrix. We assume Newtonian fluids and ν is the kinematic viscosity. These equations are closed with the ideal gas equation of state:

$$P = \rho \frac{R}{M_w} T \tag{4.24}$$

The total energy is calculated using Eq. 4.4.

4.4.2 Temporal Integration Procedure

Figure 4.1 summarizes the integration process in one computational time-step, in which the subscript o represents the starting (or "old") value, and subscripts 1, 2, and n denote stages where the variables need to be updated. Accordingly, table 4.1 lists the values of all the variables at the end of each stage. The total procedure is now explained step by step.

Step (1) Calculate the global time step, Δt_g.

The global time step is the overall Δt_g that all the physical processes use to advance to the new time-step ($t^o + \Delta t_g$). To ensure the stability of the time integration, this time step is constrained by both the physical process and the choice of numerical algorithm. The time-step limit for each process can be calculated by:

$$\Delta t_{conv} = CFL_{wave} \min\left(\frac{\Delta x}{|v| + a}\right), \tag{4.25}$$

$$\text{or} \quad \Delta t_{conv} = CFL_{fluid} \min\left(\frac{\Delta x}{|v|}\right) \tag{4.26}$$

$$\Delta t_{cond} = C_{cond} \min\left(\frac{\Delta x^2}{2\lambda/\rho c_p}\right) \tag{4.27}$$

$$\Delta t_{visc} = C_{visc} \min\left(\frac{\Delta x^2}{2\mu/\rho}\right) \tag{4.28}$$

where v is the fluid velocity, a is the speed of sound, λ is the thermal conductivity, μ is the dynamic viscosity. Here Δx is the computational mesh size and the subscripts *conv*, *cond*, and *visc* stand for convection, conduction and viscosity. Two CFL

conditions for the convection process are defined here, in which CFL_{wave} includes the acoustic velocity and CFL_{fluid} is governed only by the fluid velocity. Equivalent conditions for conduction and viscous diffusion processes are defined as C_{cond} and C_{visc}. These CFL and the C_{cond}, C_{visc} conditions are dependent on the algorithms chosen for these processes.

If each of these processes, that is convection, thermal conduction, and viscous diffusion, is integrated using an explicit algorithm, then the global time step is determined by the smallest time-step required to ensure stability. When using BIC algorithm for convection, however, the implicit time-step Δt_{conv} could be larger than the other required time-steps. In order to preserve the computational efficiency, the Δt_g is chosen as the implicit time step Δt_{conv} and the other processes are subcycled using local time steps Δt_{local} within the required stability limit.

At this stage, all of the variables have values from the previous time step. This stage is denoted as 'o' which stands for 'old' in Fig. 4.1 and all the variables are listed in the second column in Table 4.1 with subscript 'o'.

Step (2) Compute the diffusion effects

After obtaining the local time-step limits Δt_{cond} and Δt_{visc}, subcycle the integration of the heat conduction and viscous diffusion from the old time step, t^o, to the new time step, $t_n = t^o + \Delta t_g$, using a local time-step Δt_{local} for n times, where $\Delta t_{local} = \Delta t_g / n$. The number of the subcycles is determined so that the local time step is not larger than the smallest of these two limits, ($\Delta t_{local} \leq$

$\min(\Delta t_{cond}, \Delta t_{visc})$), while the number of the subcycles is minimized. Here the diffusion process is calculated using second-order spatial differencing and high-order Runge-Kutta time integration.

There is a special treatment for updating of variables at this stage. In the new BIC procedure described in section 4.3, the change of total internal energy due to the diffusion process needs to be extracted and stored temporarily in the variable $S = \Delta(\rho e)/\Delta t_g$, which will be passed into the energy equation (Eq. 4.11) that is solved in the next convection step. At this next convection step, the effect of the change of the total internal energy due to diffusion is included as a pressure effect, by redistributing the pressure correction back into the flow field through the elliptic equation 4.8. Therefore to avoid redundancy, the total internal energy at this stage should temporarily keep the value it had before the diffusion process. This means that the pressure should also stay as P_o, as pressure is a function of the total internal energy. The density, velocity, and momentum should be updated as usual. The total energy should be updated with the old internal energy before the diffusion ($P_o/(\gamma - 1)$) and the new kinetic energy ($\frac{1}{2}\rho_1 V_1^2$). Accordingly, the temperature should be calculated using the old pressure P_o and the new density ρ_1. This is listed in the third column 'After diffusion: 1' in Table 4.1.

Step (3) Compute the convective transport using BIC : explicit predictor

Now perform steps 1 and 2 of the BIC algorithm to calculate the predicted convective fluxes. That is, solve Eqs. 4.5, 4.6 and then 4.11, using the global time step Δt_g and the values updated after the diffusion process. This means the ρ^o, $\mathbf{V}^o$, P^o and E^o in Eqs. 4.5, 4.6 and 4.11 are essentially the values with subscript '1' in Table 4.1.

This stage after the explicit predictor is denoted as '2' in Fig. 4.1 and 'intermediate stage: 2' in Table 4.1. The values ρ', $\rho'\mathbf{V}'$ and $\overline{E}$ in Table 4.1 are the outputs from the monotone algorithm solver. The notation is kept same as in Eqs. 4.5, 4.6 and 4.11 for consistency. The pressure should have the same value that it had at the beginning of the time step, that is, P_o. Although the density changed at this stage, the temperature and velocity are not updated to save computational efforts as they will not be used in the next corrector step.

Step (4) Compute the convective transport using BIC : implicit corrector

Solve the elliptic equation 4.8 for the pressure correction δP. Then correct the momentum, total energy and pressure using Eqs. 4.12, 4.17 and 4.14, respectively. Here we used a multigrid elliptic solver from BoxLib [117]. The default setting of the solver is employed, where red-black Gauss-Seidel smoother is used for relaxation,

biconjugate gradient stabilized algorithm is used for the coarse grid exact solver, and V-cycle is used for restriction and interpolation between fine and coarse grids.

At this stage, which is denoted as 'n', all of the physical processes are at the same stage of integration, and all the flow properties are consistent and synchronized appropriately to the new time $t^o + \Delta t_g$. The values of all of the variables at this stage are listed in the fifth column in Table 4.1 with subscripts 'n'.

Step (5) Apply a high-frequency filter if necessary

If necessary, a high-frequency filter, which here is an extra FCT step, could be applied here after finishing all the integration processes. Since the FCT filter operates on conservative variables, primitive variables need to be updated after the filtering accordingly to avoid synchronization errors.

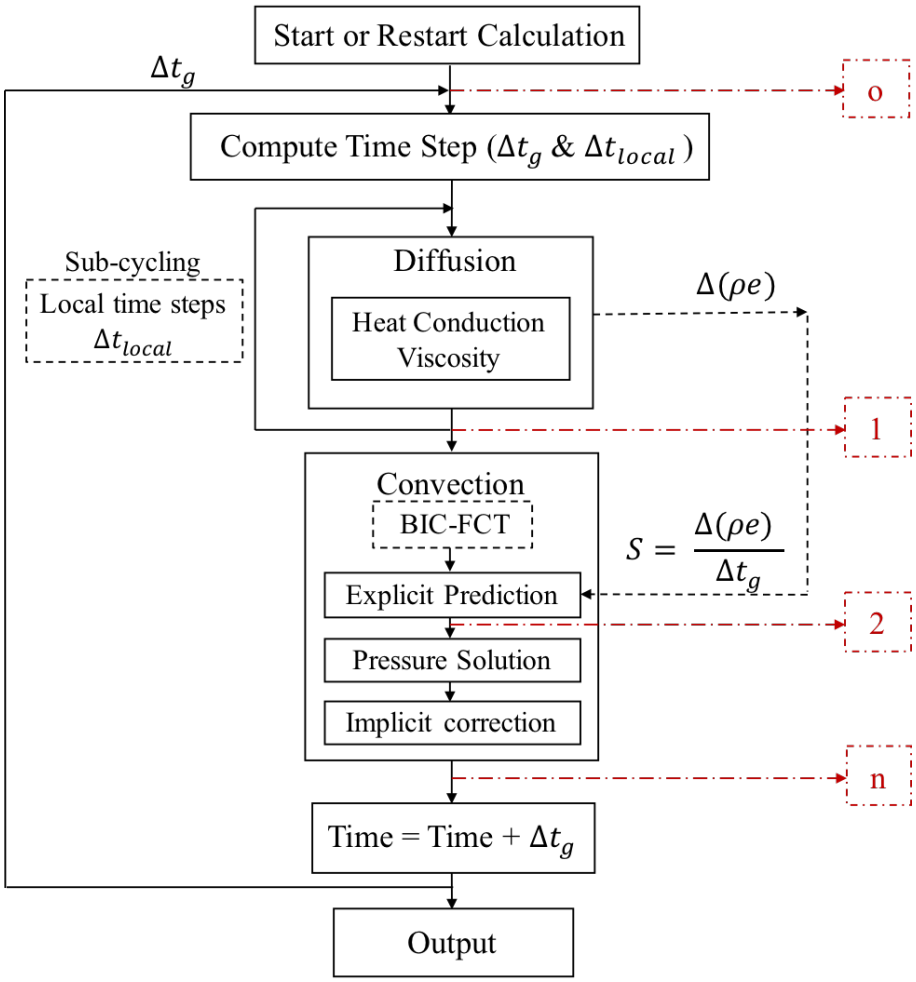

Figure 4.1: Flowchart of the coupling of the physical processes in one time-step

Table 4.1: Update of the variables at each stage

Stage	Old time step: o	After diffusion: 1	Intermediate stage: 2	New time step: n
Density	ρ_o	ρ_1	$\rho_2 = \rho'$	$\rho_n = \rho_2$
Momentum	$\rho_o V_o$	$\rho_1 V_1$	$\rho_2 V_2 = \rho' V'$	$\rho_n V_n = \rho_2 V_2 - \Delta t \nabla \delta P$
Energy	$E_o = \frac{P_o}{\gamma - 1} + \frac{1}{2}\rho_o V_o^2$	$E_1 = \frac{P_o}{\gamma - 1} + \frac{1}{2}\rho_1 V_1^2$	$E_2 = \overline{E}$	$E_n = \frac{\omega P_o + \delta P}{(\gamma - 1)\omega} + \frac{1}{2}\rho_n V_n^2$
Pressure	P_o	$P_1 = P_o$	$P_2 = P_o$	$P_n = P_o + \delta P/\omega$
Temperature	T_o	$T_1 = P_o/R\rho_1$	$T_2 = T_1$	$T_n = P_n/R\rho_n$
Velocity	V_o	V_1	$V_2 = V_1$	$V_n = \rho_n V_n/\rho_n$

Chapter 5: Test Cases[1]

In the following, the performance of the BICFCT algorithm is examined for four test problems. Section 5.1 studies the order of convergence in time and space by convecting a sinusoidal density profile. In section 5.2, simulations of a 2D lid-driven cavity flow demonstrate the ability of BICFCT on solving steady-state swirling flows. The results are compared with a numerical solution using a vorticity-stream-function formulation of the incompressible Navier-Stokes equations [24]. Section 5.3 describes simulations of a 2D doubly periodic shear layer. These are used to examine the behavior of the BIC algorithm when it is used to simulate transient flows with strong vorticity gradients. The results are qualitatively compared with a "Numerical Acoustic Relaxation (NAR)" method [25] and quantitatively compared with a pseudospectral method [26]. In section 5.4, the BICFCT algorithm is applied to a 3D vortex breakdown problem, which validates its ability of predicting the instabilities that occur in swirling jet flows. The results are qualitatively comparable with a previous DNS simulation [27].

For all of the test problems in this paper, the implicitness parameter $\omega = 1.0$ is used. The original BIC paper tested the prior version of the algorithm for variable

[1]This Chapter is a slightly modified version of what has been published in [1, 2] and has been reproduced here with the permission of the copyright holder.

ω and showed the damping and dispersion effects of ω on sound waves. For all of the low-Mach number flows of interest to us here, $\omega = 1.0$ is adequate. We leave the investigation of variable ω to future work when we discuss reactive flows.

5.1 1D Convection of a Sinusoidal Density Profile

This simulation solves the 1D convection equation for density with an initial sinusoidal profile $\rho^o(x) = 1 - 0.1\sin(\pi x)$ on the domain $x \in [0, 2]$ with periodic boundary conditions. The convection speed is initialized with a constant value of 1m/s. First we study the order of convergence in space by keeping the $\text{CFL}_{\text{fluid}}$ constant as 0.3 and varying the grid size Δx with the values $\{0.0125, 0.025, 0.05, 0.1\}$ m. We measure the L1 norm of the error of the density profile for each simulation at time $t = 2$ s, which is one convection period. The result is shown in Fig. 5.1, which shows that BICFCT has second order accuracy of convergence in space.

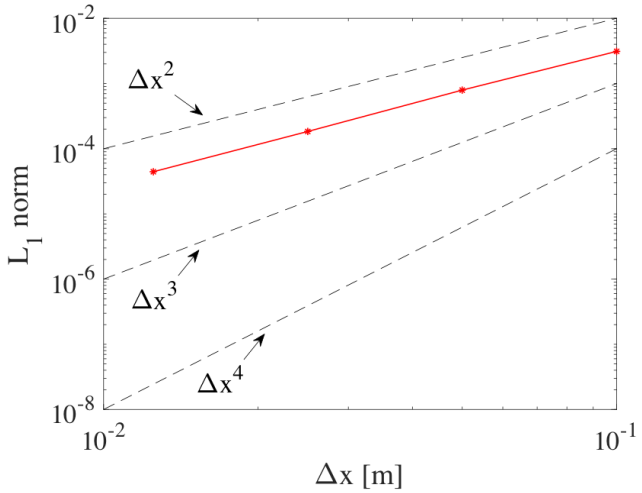

Figure 5.1: BICFCT's order of convergence in space of a sinusoidal density convection. The dots connected by the solid line are the L1 norm of errors of the simulations using BICFCT.

Then we study the order of convergence in time by keeping the grid size constant with $\Delta x = 0.05$ and varying $\text{CFL}_{\text{fluid}}$ with the values of $\{0.05, 0.1, 0.2, 0.3\}$. The L1 norm of the error of the density profile for each simulation at time $t = 2$ s is shown in Fig. 5.2. The results show that the error does not converge as the time step Δt decreases. This can be explained by how the diffusion and antidiffusion stages work in LCPFCT. During the diffusion stage, second order diffusion is first added to the solution (Eq. 3.24 - 3.26) to ensure monotonicity. Then, the flux limiter picks one from the three antidiffusion terms in Eq. 3.46, which are an antidiffusive flux with a designed coefficient μ and two other values calculated by the neighboring low-order (convected and diffused) solutions, to counteract the excessive diffusion added during the diffusion stage and make the final solution accurate while maintaining monotonicity. When the flux limiter chooses the first term in Eq. 3.46, the antidiffusive flux with μ, the numerical diffusion introduced by the diffusion stage is completely removed as the time step Δt approaches zero. This means the error after convection decreases as Δt decreases and the solution should converge. When the flux limiter chooses the other two terms calculated by neighboring low-order solutions, however, the numerical diffusion cannot be completely canceled as time step Δt approaches zero, leaving residual diffusion that is not a function of Δt. Therefore, when Δt approaches zero, the amount of dissipation does not necessarily go to zero. In fact, when Δt is small, it takes more iterations for one convection period, which could introduce more dissipation. This explains why the error actually increases with decreasing Δt in the 1D convection of the sinusoidal density profile. The details of where the residual diffusion comes from are described in the following

discussion section.

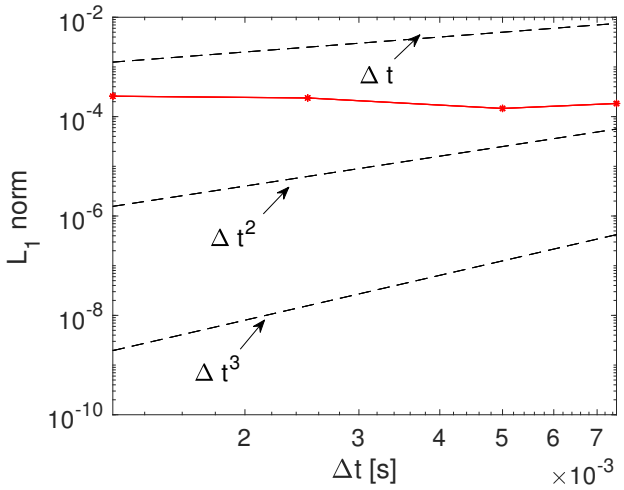

Figure 5.2: BICFCT's order of convergence in time of a sinusoidal density convection. The dots connected by the solid line are the L1 norm of errors of the simulations using BICFCT.

5.2 2D Lid-Driven Cavity

This simulation considers flow in a 2D square cavity with no-slip boundary conditions on the lower and side walls, and an upper wall moving with a constant uniform velocity. A primary vortex, driven by shear forces, eventurally forms at the center of the cavity. It is accompanied by secondary vortices at corners. The flow pattern is shown in Fig. 5.3 as streamlines superimposed on the field of velocity in the horizontal direction (x-velocity). The lid-driven flow is a classical test problem for validation of numerical methods and computational codes. Previous numerical results are reviewed in [118]. Here we compare our simulations with the data from Ghia et al. [24], who solved a vorticity-stream-function formulation of the 2D incompressible Navier-Stokes equations using a finite-difference method.

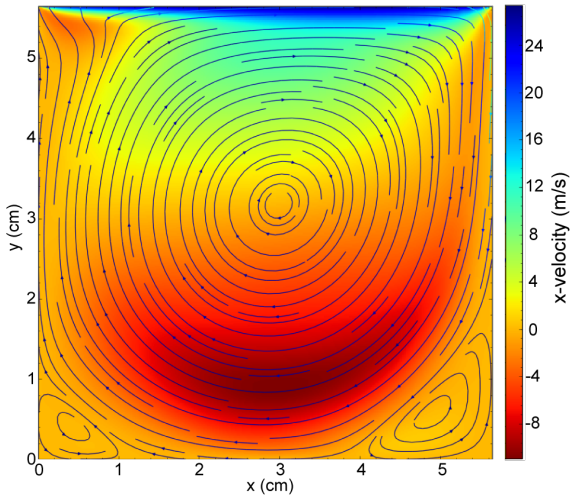

Figure 5.3: Streamline superimposed on the contour of x-velocity for case 3 with $Re = 1000$, $CFL_{wave} = 86$.

Three different implicit time steps using BIC are tested by holding $CFL_{fluid} = 0.5$ as a constant and varying sound speed through flow temperatures from 300 K to $3,000$ K and $30,000$ K. The resultant CFL_{wave} equals to 13, 38 and 86 respectively. Other than the temperature, the other flow properties are initialized to model dry air at standard condition (300 K, 1 atm). The values of the parameters are summarized in Table 5.1 below. The test cases are performed for $Re = 1000$. Using all the values in Table 5.1, we derive the lid velocity $U_{lid} = 27.775$ m/s and the length of the square cavity $H = 0.0565$ m. A non-slip wall boundary condition is applied at all the four boundaries. The upper wall has a constant velocity U_{lid}. All of the calculations are performed on a uniform 256×256 Cartesian mesh.

Table 5.1: Properties of the flow for three test cases: case 1 with $CFL_{wave} = 13$, case 2 with $CFL_{wave} = 38$, and case 3 with $CFL_{wave} = 86$. The Re is defined as $U_{lid}H/\nu$, and Ma is defined as $U_{lid}/\sqrt{\frac{\gamma R_u T}{M_{w,air}}}$.

	Re	Ma	T [K]	P [atm]	$M_{w,air}$ [kg/mol]	γ	ν [m^2/s]	Pr
Case 1	1000	0.08	300	1.0	28.97	1.4	1.568×10^{-5}	0.711
Case 2	1000	0.0253	3000	1.0	28.97	1.4	1.568×10^{-5}	0.711
Case 3	1000	0.008	30000	1.0	28.97	1.4	1.568×10^{-5}	0.711

Figure 5.4 presents the velocity profiles (x-velocity and y-velocity) at the vertical and horizontal centerlines of the cavity for cases 1 with $CFL_{wave} = 13$. The effect of the fourth order FCT filter is tested in this calculation. The steady state results show good agreement when compared with the reference data from Ghia et al. [24]. The results in Fig. 5.4 show that the application of the filter does not affect the accuracy of the calculation, and does not change the flow structure.

Figure 5.5 and 5.6 show the velocity profiles for case 2 with $CFL_{wave} = 38$ and case 3 with $CFL_{wave} = 86$. These calculations with relatively high CFL_{wave} conditions are performed with the filter. The steady state results for both cases agree well with the reference data [24].

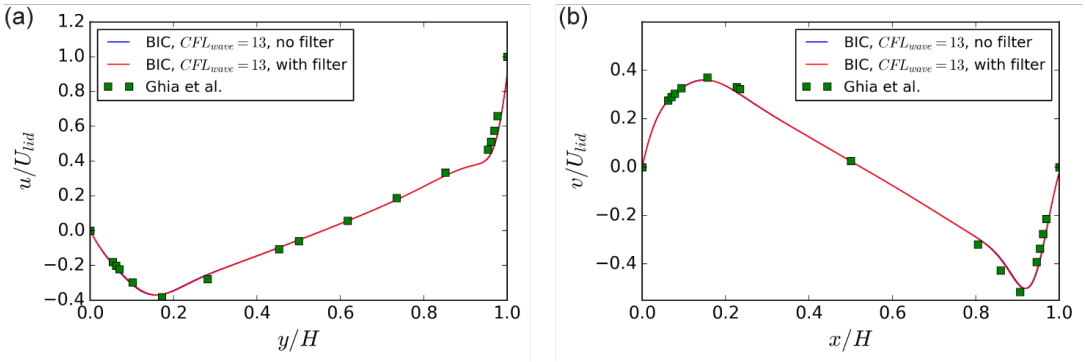

Figure 5.4: Comparison of the velocity profiles at the cavity's centerlines for $Re = 1000$, $CFL_{wave} = 13$ with and without filter. (A) x-velocity along the vertical centerline. (B) y-velocity along the horizontal centerline. Squares: data from calculation using $(\omega - \psi)$ formulation (Ghia et al. [24]); Line plots: implicit calculation using BIC (present work). For this calculation, with and without the filter give same results to numerical accuracy.

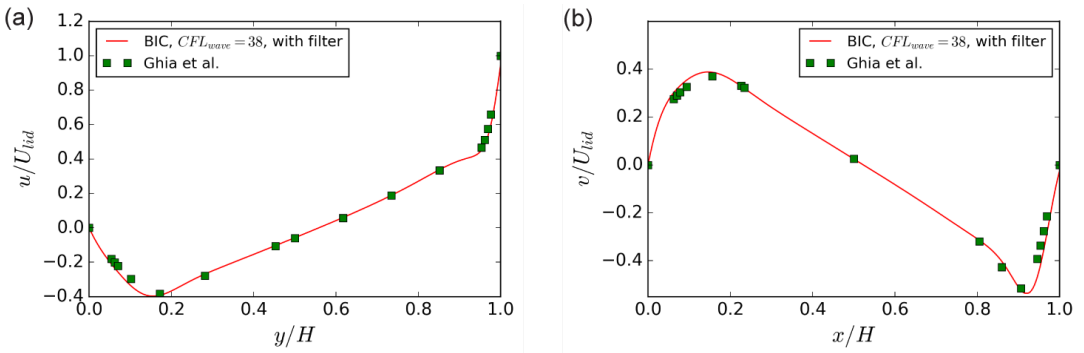

Figure 5.5: Comparison of the velocity profiles at the cavity's centerlines for $Re = 1000$, $CFL_{wave} = 38$ with filter. (A) x-velocity along the vertical centerline. (B) y-velocity along the horizontal centerline. Squares: data from calculation using $(\omega - \psi)$ formulation (Ghia et al. [24]); Line plots: implicit calculation using BIC (present work).

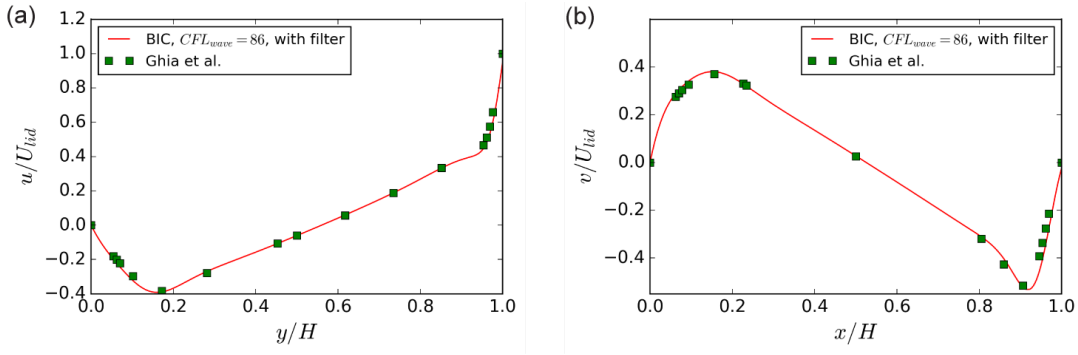

Figure 5.6: Comparison of the velocity profiles at the cavity's centerlines for $Re = 1000$, $CFL_{wave} = 86$ with filter. (A) x-velocity along the vertical centerline. (B) y-velocity along the horizontal centerline. Squares: data from calculation using $(\omega - \psi)$ formulation (Ghia et al. [24]); Line plots: implicit calculation using BIC (present work).

5.3 2D Doubly Periodic Shear Layers

The simulations of 2D double shear layers with periodic boundaries on all sides are performed in a unit domain $[0, 1] \times [0, 1]$. In this domain, a horizontal jet is initialized with small vertical perturbations, and at the jet boundaries, the two shear layers roll up into large vortices as the flow evolves. This configuration was originally introduced by Bell, Colella & Glaz [119], and further examined by Minion & Brown [26], Nourgaliev, Dinh & Theofanous [25] to compare various numerical methods for stability and accuracy, as the large vorticity gradients in this setup are

sensitive to the numerical algorithms. The initial velocity condition is given by

$$u = \begin{cases} \tanh\left(\vartheta\left(y - 0.25\right)\right), & \text{for} \quad y \leq 0.5 \\ \tanh\left(\vartheta\left(0.75 - y\right)\right), & \text{for} \quad y > 0.5 \end{cases}$$

$$v = \gamma \sin\left(2\pi\left(x + 0.25\right)\right) \tag{5.1}$$

where ϑ is the parameter that controls the width of the shear layer. The initial perturbation uses the lowest wavenumber with an amplitude γ. The other flow properties are initially uniform throughout the domain. In this work, calculations are performed for a "thin layer" configuration $\vartheta = 80$, with a perturbation strength $\gamma = 0.05$ at $Re = 10,000$. The initial velocity profiles are shown below:

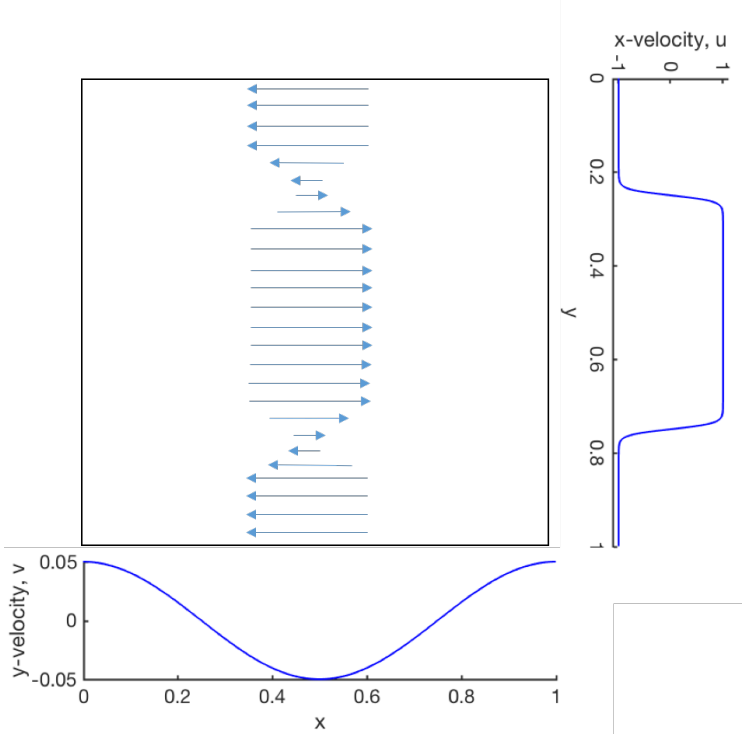

Figure 5.7: Initial velocity conditions for doubly periodic shear layers.

The different computations are performed on uniform Cartesian grids, 256×256 and 512×512. A summary of the vorticity maps for a time late into the calculation is shown by Figs. 5.8 to 5.10. Quantitative comparisons of the decay of total enstrophy and total kinetic energy with the results obtained by the pseudospectral method of Minion & Brown [26] are shown in Fig. 5.11. Their pseudospectral method solves the incompressible Navier Stokes equations using a projection method in spectral space and a fourth-order Runge-Kutta method for time integration.

Figure 5.8 compares the results of simulations using explicit FCT and implicit BIC, with the same time step governed by $CFL_{wave} = 0.9$. This is close to the explicit stability limit for this low-speed flow problem. The vorticity fields show good agreement between the explicit and implicit results. The vorticity fields are also in qualitative agreement with those shown by Nourgaliev, Dinh & Theofanous [25]. In Fig. 5.11, the dissipation profiles of the total enstrophy and the total kinetic energy for both the explicit and the implicit simulations agree closely with those shown by the pseudospectral method on a 768×768 grid. The difference between the explicit and the implicit calculation for the total enstrophy is about 0.16%, and in the total kinetic energy is about 0.019%.

Figure 5.9(a) shows the result of the calculation using BIC with $CFL_{wave} = 32$ (the corresponding $CFL_{fluid} = 0.1$) on the 256×256 grid. In addition to the two large main vortices, there are "wrinkles" in the shear layers. A closer examination of these shows that they are small vortices. These vortices were also found and discussed by Minion & Brown [26], who showed that when the flow is under-resolved, spurious vortices form due to perturbations with higher wavenumbers imposed by

the truncation errors from the numerical discretization. When a finer mesh with 512×512 is used with $CFL_{wave} = 32$, the spurious vortices disappear as shown in Fig. 5.9(b). Another calculation is performed on the 512×512 grid using an even larger time step with $CFL_{wave} = 58$ (the corresponding $CFL_{fluid} = 0.2$), as displayed in Fig. 5.9(c). In general, the vorticity fields of all cases in Figs. 5.8 and 5.9 agree well with each other, both in terms of the structure of the main vortices and the shear layer thickness. It indicates, however, that the implicit calculations may require a higher resolution than the explicit FCT to resolve the flow features when using large implicit time steps. This is possibly due to the relatively low-order calculation for the pressure correction in BIC compared with the accuracy of the fourth-order FCT (when calculating the pressure correction, a second-order discretization is used for the Laplacian-like term in the elliptic equation (Eq. 4.8), and a 3-point stencil for each dimension for the multigrid solver is selected in Boxlib).

As shown in Fig. 5.11, all of the dissipation curves for calculations using BIC with large time steps agree closely with the pseudospectral method on a 768×768 grid. The good agreement validates the ability of BIC to predict consistent results using various time steps. Some minor differences, however, do appear in the comparison of the cases with different time steps in Fig. 5.11. With the same resolution, calculations with larger time steps show slightly faster dissipation, which is seen in the comparison of the cases on grid 256×256 with $CFL_{wave} = 0.9$ and $CFL_{wave} = 32$, and the cases on grid 512×512 with $CFL_{wave} = 32$ and $CFL_{wave} = 58$ in Fig. 5.11.

We now consider the effects of further increasing the time step. A relatively

large time step with $CFL_{wave} = 150$ (the corresponding $CFL_{fluid} = 0.5$) is used for an implicit simulation on a 512×512 grid without the filter. The result is shown in Fig. 5.10(a), in which numerical instabilities appear inside and around the outer-edge of the vortices. These instabilities can be seen in the vorticity fields, and are presented more clearly in the vorticity contours. These oscillations cause a faster decay of both the total enstrophy and the kinetic energy compared with the curves for other stable calculations as shown in Fig. 5.11. Intended to stabilize the calculation, the filter is then applied to re-calculate this case using the same time step with $CFL_{wave} = 150$. As shown in Fig. 5.10(b), applying the FCT filter helps eliminate the oscillations outside of the vortices, which brings the dissipation curves in Fig. 5.11 slightly closer towards the other stable solutions than the curves of the case without the filter. There is, however, still a noticeable difference between the dissipation curves. Very small oscillations around the edges of the vortices appear when a closer examination is taken of Fig. 5.10(b). Despite these differences, the actual difference of the total kinetic energy in value is only about 0.51% compared with other calculations using smaller time steps. This decrease of the kinetic energy causes a 0.4 K increase in temperature. Nevertheless, this case suggests that the filter can help mitigate spurious oscillations, which allows for more acceptable solutions to be obtained.

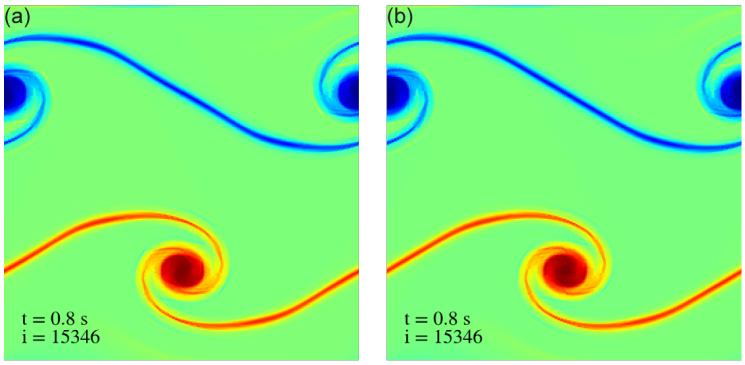

Figure 5.8: Vorticity fields for calculations using explicit FCT and implicit BIC with $CFL_{wave} = 0.9$. The implicit BIC calculation is performed without the filter

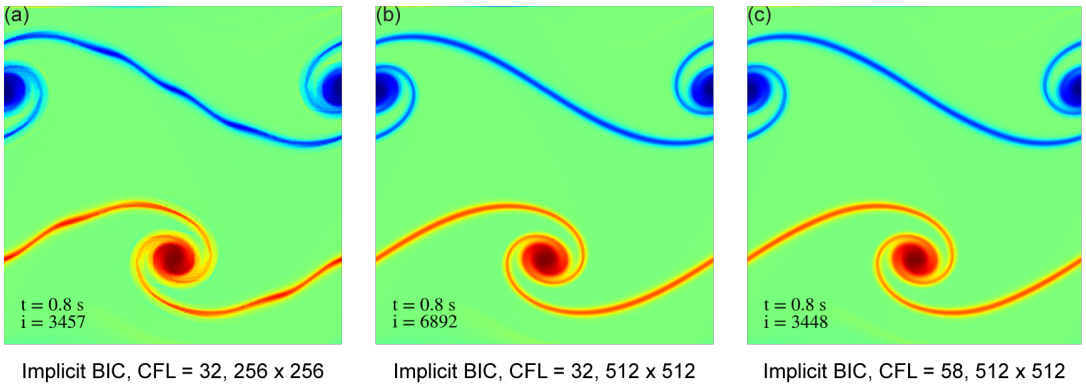

Figure 5.9: Vorticity fields for implicit BIC calculations with different time steps and grids. The FCT filter is applied on all of these three cases.

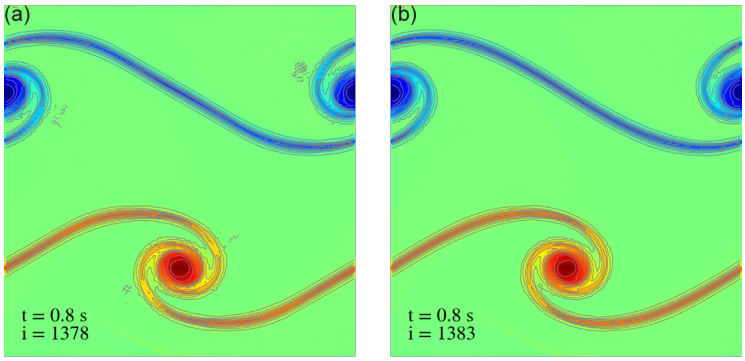

Figure 5.10: Vorticity fields with superimposed vorticity contours for implicit BIC calculations with $CFL_{wave} = 150$ on a 512×512 grid, (a) without the filter and (b) with the filter.

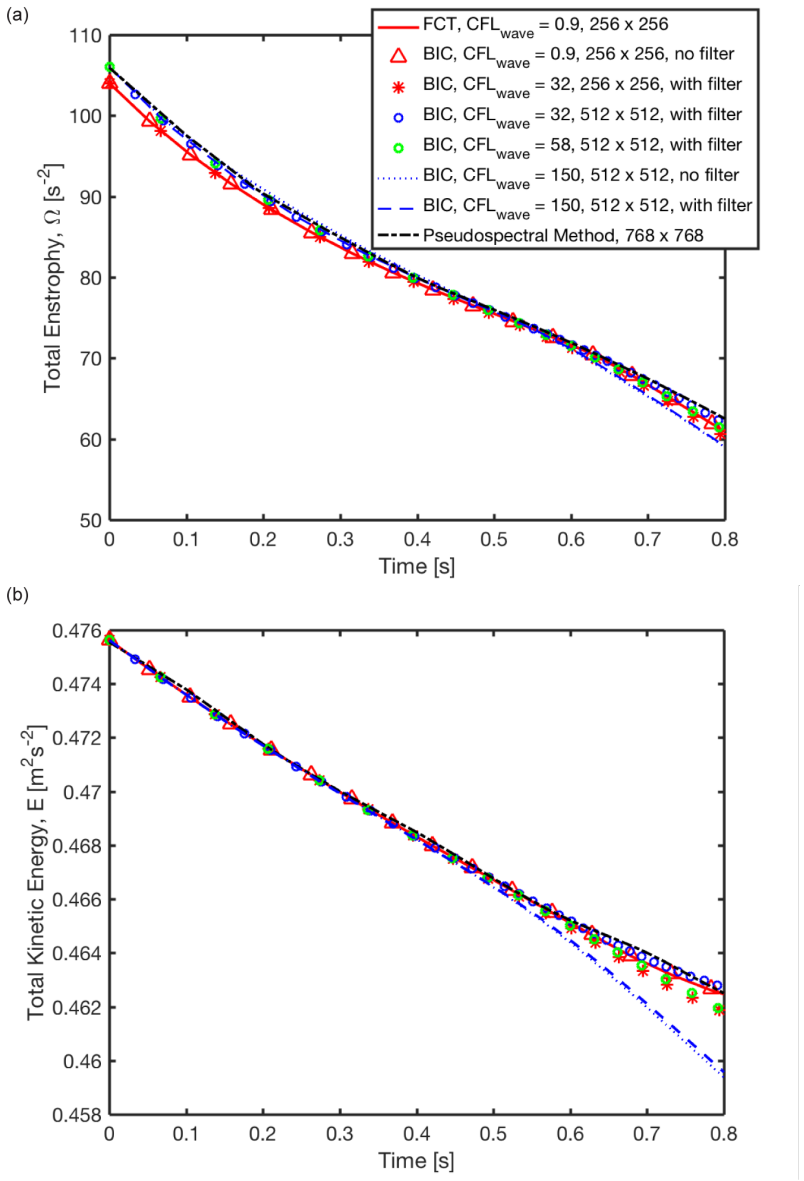

Figure 5.11: Time history of (a) total enstrophy, $\sum_{i,j} \frac{\omega_{i,j}^2}{2} \frac{\Delta A_{i,j}}{A_{\text{total}}}$, and (b) total kinetic energy, $\sum_{i,j} \frac{|u|_{i,j}^2}{2} \frac{\Delta A_{i,j}}{A_{\text{total}}}$ for doubly periodic "thin" shear layer tests at $Re = 10,000$. Comparison of explicit FCT, implicit BIC calculations with the solution by the psedospectral method (Minion & Brown [26]).

5.4 3D - Vortex Breakdown

A 3D vortex breakdown problem was computed to test the ability of BIC to predict the instabilities that occur in swirling jet flows. In swirling jets, the vortex structure may be affected by disturbances imposed by the evolution of fluid dynamics, physical boundaries, and temperature. These disturbances can cause adverse pressure gradients on the vortex core. When the axial momentum of the flow is not sufficient to overcome the force generated by the adverse pressure gradient, the vortex structure can form a new stable state. This state is characterized by a stagnation point on the central axis of the vortex with a recirculation zone around it. This change in the vortex structure is referred to as "vortex breakdown."

Based on distinctive internal structures, vortex breakdown was characterized into three types by Sarpkaya [33]: the spiral mode, the bubble mode, and the double-helix mode. Seven types were reported by Faler & Leibovich [39], which include more intermediate states. Extensive research has been done over the past on this phenomenon, which leads to a conclusion that the types of breakdown are mainly controlled by the flow Reynolds number and the swirling level. Here, we adopt one set of the flow parameters from a DNS simulation by Ruith et al. [27]. Under this selected flow condition, the vortex undergoes three major types of breakdown.

In the calculations presented below, the flow is initialized with a "Grabowski vortex" profile, which is adopted from [27], originally introduced by Grabowski & Berger [28]. The azimuthal, radial, and axial velocities vary with the radial location

r:

$$v_\theta(0 \leq r \leq 1) = Sr(2 - r^2) \tag{5.2}$$

$$v_\theta(1 \leq r) = S/r \tag{5.3}$$

$$v_r(r) = 0 \tag{5.4}$$

$$v_z(0 \leq r \leq 1) = \alpha + (1 - \alpha)r^2(6 - 8r + 3r^2) \tag{5.5}$$

$$v_z(1 \leq r) = 1 \tag{5.6}$$

Here, the swirl number is defined as $S = v_\theta(R)/v_{z,\infty}$, where R is the radius of the vortex core, and the Reynolds number is $Re = v_{z,\infty}R/\nu$.The coflow parameter $\alpha = v_{z,c}/v_{z,\infty}$ describes the axial velocity as a jet-like ($\alpha > 1.0$) or wake-like profile ($\alpha < 1.0$). We set $Re = 300$, $S = 1.3$, $\alpha = 1$, $R = 1$, and $v_{z,\infty} = 1$ m/s, which is one case in [27]. In a swirling flow, the centrifugal force directed outwards should be balanced by the pressure gradient force pointing inwards. Based on the radial force balance,

$$\frac{v_\theta^2}{r} = \frac{1}{\rho}\frac{\partial P}{\partial r} \tag{5.7}$$

we derive the Grabowski pressure profile outside (Eq. 5.8) and inside (Eq. 5.9) of

the vortex core as a function of the radial location:

$$P_{out}(1 \leq r) = \rho S^2 \left(-\frac{1}{2r^2}\right) + P_\infty \tag{5.8}$$

$$P_{in}(0 \leq r \leq 1) = \rho S^2 \left[\frac{r^6}{6} - r^4 + 2r^2 - \frac{7}{6}\right] + P_{out}(r = 1) \tag{5.9}$$

Three simulations are presented in this work:

1. Reference case: Explicit calculation using FCT with $CFL_{wave} = 0.95$. Vortex breakdown in the chosen flow configuration is controlled more by kinematic than thermodynamic effects, in order to maximize the time step, the sound speed was scaled through density while keeping the Mach number below 0.15:

   a) The maximum Mach number is defined as $M_{max} = v_{max}/a = v_{max}/\sqrt{\gamma P/\rho}$, in which v_{max} is the maximum fluid velocity and a is the sound speed. In order to keep M_{max} below 0.15, we selected a clean number for ρ as 1000 kg/m^3 so that the resulted far-field pressure $P_\infty \approx 71428$ Pa, which is not too far from the realistic condition. Peak velocity magnitude v_{max} is obtained from the initial velocity field.

   b) Then the molecular weight is chosen as high as $M_w = 1000$ kg/kmol, so that the temperature is not unrealistically low. The resultant temperature in the initial flow field is $T_{min} = 8.427$ K and $T_{max} = 8.573$ K, which is calculated using $T = PM_w/(R_u\rho)$.

2. Implicit calculation using BIC with $CFL_{wave} = 2.0$. This calculation keeps all of the flow properties as the reference case. The corresponding CFL_{fluid} is around

0.2.

3. Implicit calculation using BIC with $CFL_{wave} = 60$. This case intends to test the performance of BIC at higher CFL_{wave} condition. Therefore, the sound speed was scaled up by raising the flow temperature through lowering the density from 1000 kg/m^3 to 1 kg/m^3. This setup results in a similar corresponding CFL_{fluid} around 0.2. Except for the density and temperature, all the other flow properties are same as in the explicit simulation.

The initial pressure and azimuthal velocity profiles are shown in Figure 5.12. They are same for all of the cases.

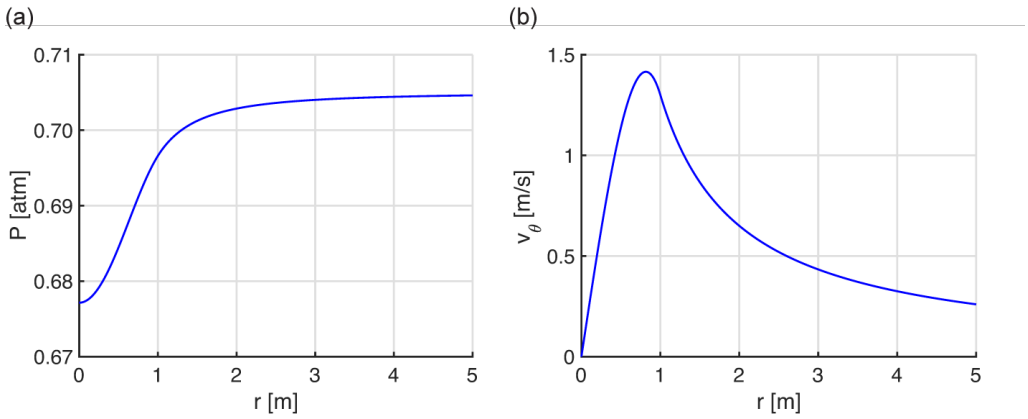

Figure 5.12: Grabowski vortex profile with $S = 1.3$, $\alpha = 1$: (a) Pressure distribution for the Grabowski vortex profile; (b) Azimuthal distribution for the Grabowski vortex profile.

The simulations are performed on a 40 m $\times$ 40 m $\times$ 20 m domain as shown in Fig. 5.13, in which we define the z-axis as the axial direction. An inflow condition is imposed on the lower axial x-y plane, as indicated in Fig. 5.13, with the Grabowski vortex profile as described above. The upper axial x-y plane is treated as non-reflecting. The pressure is controlled at the lateral boundaries by the Bernoulli's

equation, since the flow is assumed to be irrotational outside of the vortex core. This boundary pressure is then calculated by $P = P_\infty - \rho V^2/2$, where V is the magnitude of the velocity. The velocity at the lateral boundaries are specified using a first order extrapolation with a zero gradient. For flow leaving the boundaries, we also apply the same first order extrapolation with a zero gradient for the temperature. For flow coming into the boundary, we specify the temperature using the ideal gas law with the fixed density discussed earlier.

The flow is initialized with the axisymmetric, columnar Grabowski vortex profile throughout the whole domain, in which the axisymmetry is applied at the center of the x-y plane along the z axis. Cartesian mesh is employed with three levels of refinement. The cell width is halved for each level. The refinement does not change during the calculation. The radial location of refinement is fixed at where the radial pressure gradient is not significant based on Eqs. (5.8) and (5.9).

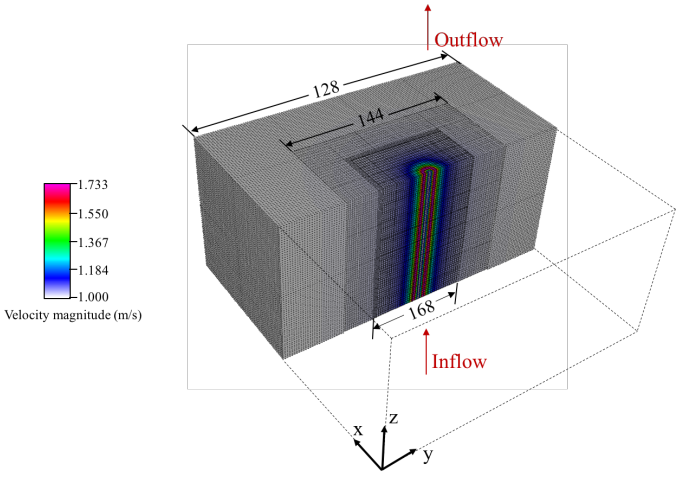

Figure 5.13: Computational domain and mesh with superimposed initial velocity field

Figures 5.15 to 5.17 show time series for the three simulations. In these figures,

the flow streaklines are superimposed on normalized pressure contours, where the dark region indicates higher pressure and the light region indicates low pressure. As the major vortex structure is at the center of the computational domain, only a small central section of the domain of 4 m $\times$ 20 m is shown in Figs. 5.15 to 5.17. They have been rotated 90° from that shown in Fig. 5.13, with the flow now going from left to right. The flow particle paths are visualized through streaklines by releasing massless particles at the inflow boundary, from 18 locations distributed evenly along a circle centered at the vortex axis with a 5 cm radius. The particles released on the circle are colored as black, white and grey, which were selected to show different initial locations and the swirling motion. At the center of the vortex, the particles are colored pink. A schematic diagram of these particle injection points is shown in Fig. 5.14.

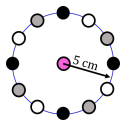

Figure 5.14: Layout of the particle injection location

In all of the three cases, the flow starts to decelerate in the axial direction at a similar time around 23.0 s, and a similar location on the vortex axis. This deceleration leads to a radial expansion of the vortex core, which eventually results in the formation of the bubble mode. The bubbles in all the cases start to show a conical shape at about 45.0 s. At around 90.0 s, the bubbles are developed to a similar size, and then the downstream instabilities start to occur.

Under this flow condition and the current setup of the domain, the downstream

secondary instability initially forms the double-helix mode, then transitions to the spiral mode, and finally settles back into the double-helix mode. In Fig. 5.15, this transition appears in the explicit simulation as shown by the distinct flow structures of an early-stage, relatively narrow double-helix mode at time 112.0s (Fig. 5.15d), a spiral mode at time 187.0s (Fig. 5.15e), and a widely expanded double-helix mode at time 703.0s (Fig. 5.15g). Both implicit calculations are able to predict this transition. As shown in Fig. 5.16 where the $CFL_{wave} = 2.0$, the flow downstream first forms a narrow double-helix mode at time 118.0s (Fig. 5.16d). After a short period, this mode is then replaced by a spiral mode shown at time 165.0s in Fig. 5.16 (e). Eventually, the downstream flow settles into a stable, widely expanded double-helix mode shown at time 369.0s (Fig. 5.16f) and a later time 650.0s (Fig. 5.16g). This stable double-helix mode has a thinner flow structure comparing with the earlier transient one in Fig. 5.16 (d). Similarly in Fig. 5.17 where the $CFL_{wave} = 60$, the early stage double-helix flow structure appears at time 118.4s (Fig. 5.17d), followed by a spiral mode at time 164.0s (Fig. 5.17e), and eventually transitions to a steady state with a widely expanded double-helix mode shown at time 369.3s (Fig. 5.17f) and a later time 650.5s (Fig. 5.17g). The results of the two implicit calculations with different CFL_{wave} conditions agree closely with each other, both in terms of the flow structures and the phase accuracy. The flow structures in the explicit calculation and the two implicit calculations also agree quite well with the previous DNS simulation results from Ruith et al. [27]. These computations show the ability of the BIC algorithm to capture and predict the transition of all three major types of the vortex breakdown using large implicit time steps.

Figure 5.18 shows a quantitative comparison of the pressure and the axial velocity along the axial direction for the explicit FCT simulation and the two implicit BIC simulations. The profiles are taken at three radial locations, ranging from the vortex axis ($r = 0$ m) to the far field ($r = 8$ m). In Fig. 5.18 (a), the bubble mode in the three calculations is developing while the downstream flow is not affected by the secondary instabilities. The location of the bubble formation is indicated by the minimum velocity on the axial velocity profile at $r = 0$ m. It shows that the location of the bubble is almost the same for all three cases, although the downstream recovery of the vortex is slightly different. This leads to a more pronounced difference in the behavior when the spiral and double-helix modes occur, which is shown in Fig. 5.18 (b). Here, at the centerline $r = 0$ m, we observe a secondary minimum in the axial velocity downstream of the bubble, which corresponds to the bifurcation point of the double helix. This minimum is lower in the implicit calculations than it is in the explicit calculation, which implies the flow experiences a stronger deceleration at the double-helix bifurcation point in the implicit calculations. This is consistent with the stronger adverse pressure gradient near this point in the implicit calculations seen in Fig. 5.18 (b). Although there is a difference between the explicit and implicit simulations, this difference does not grow as CFL_{wave} is increased.

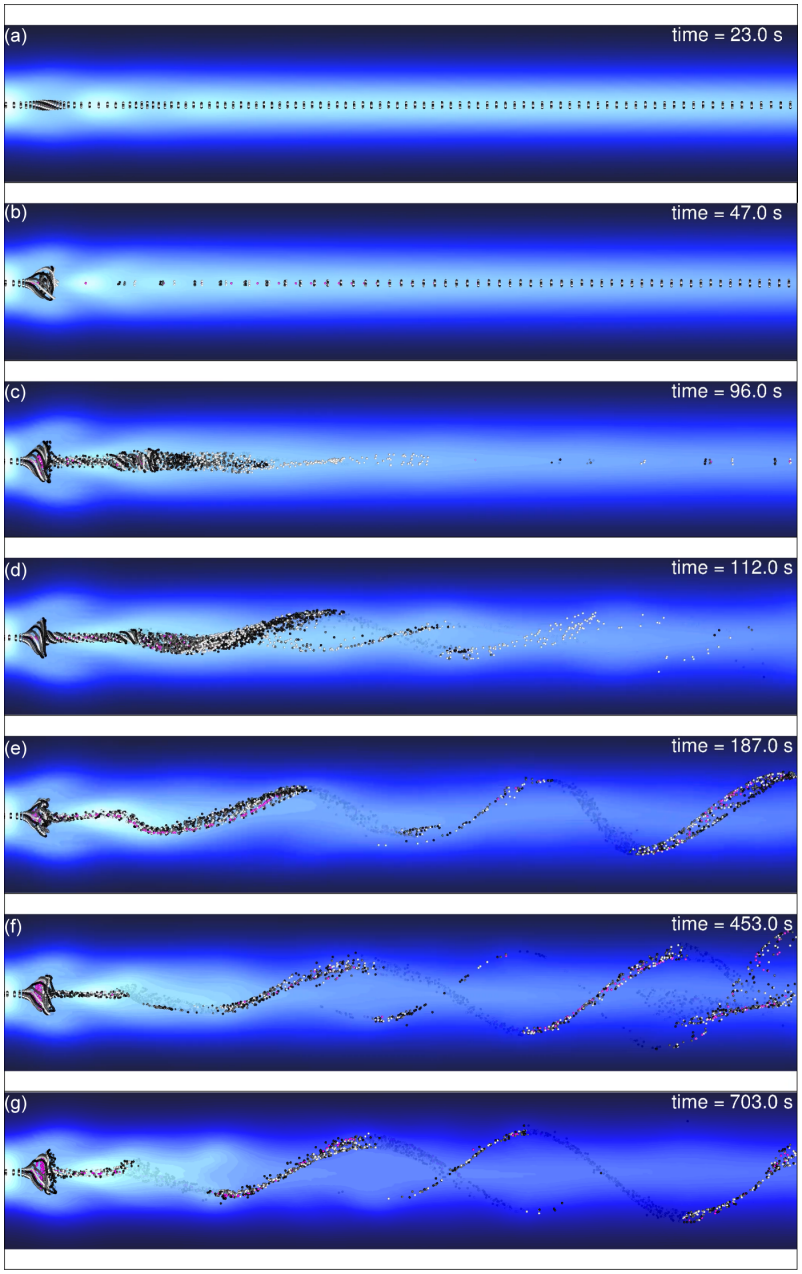

Figure 5.15: Streaklines imposed on contours of normalized pressure for the explicit FCT calculation with $CFL_{\text{wave}} = 0.95$. The darker regions indicate higher pressure and the lighter regions indicate lower pressure. Time steps are selected to show the formation and transitions of the instability modes.

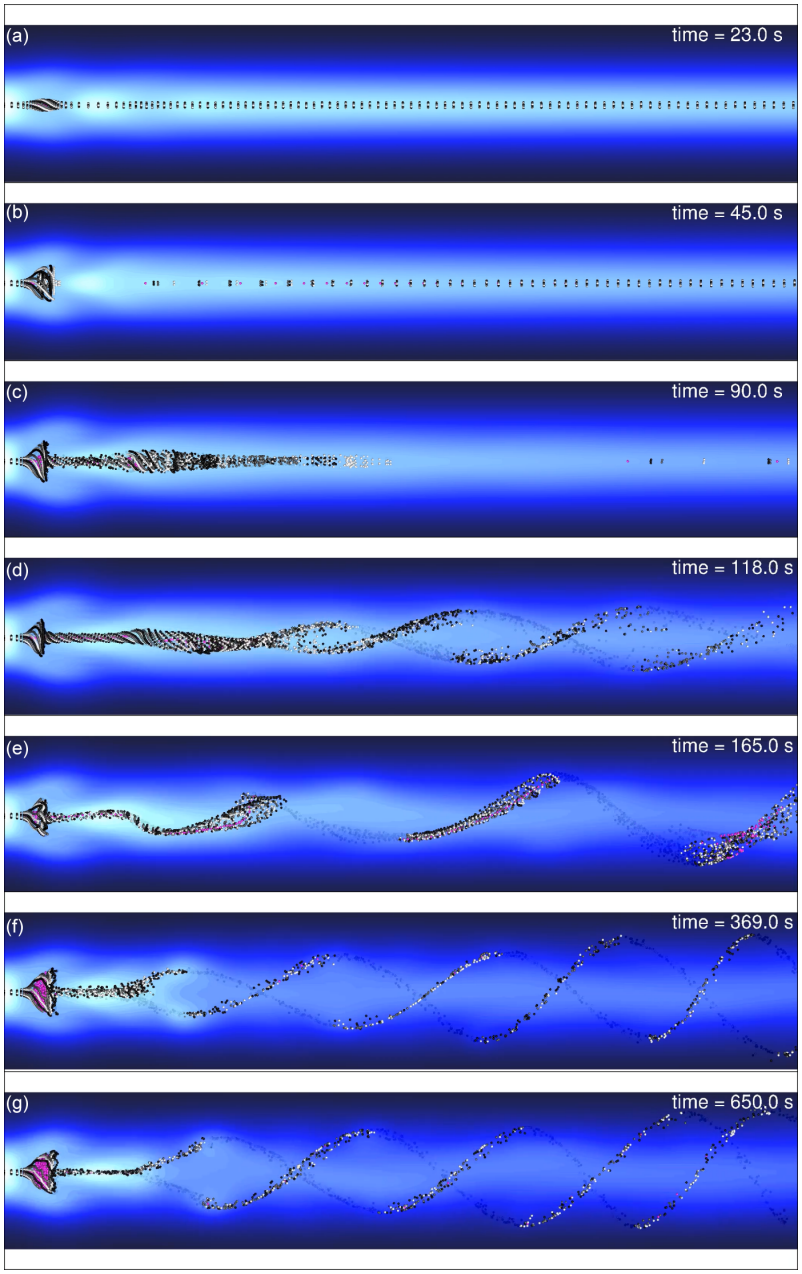

Figure 5.16: Streaklines imposed on contours of normalized pressure for the implicit BIC calculation with $CFL_{\text{wave}} = 2.0$. The darker regions indicate higher pressure and the lighter regions indicate lower pressure. Time steps are selected to show the formation and transitions of the instability modes. The FCT filter is applied.

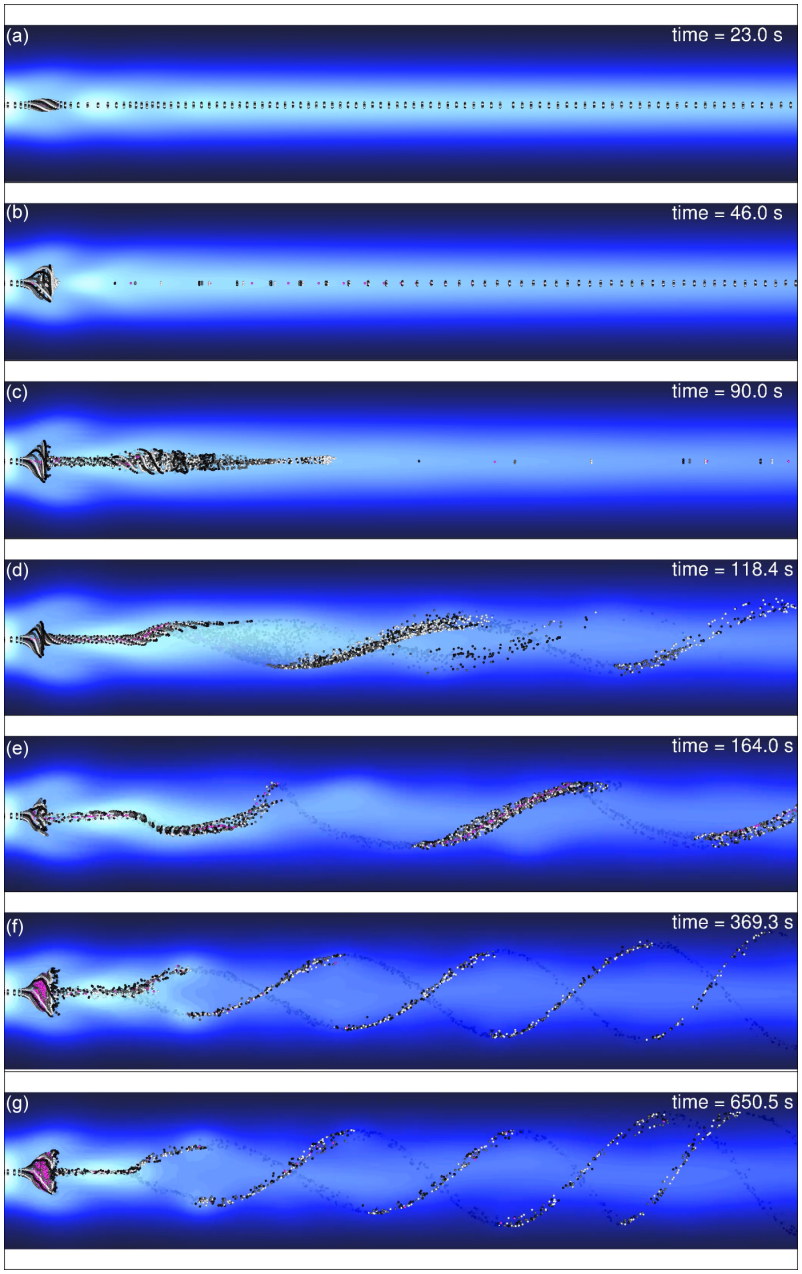

Figure 5.17: Streaklines imposed on contours of normalized pressure for the implicit BIC calculation with $CFL_{\text{wave}} = 60.0$. The darker regions indicate higher pressure and the lighter regions indicate lower pressure. Time steps are selected to show the formation and transitions of the instability modes. The FCT filter is applied.

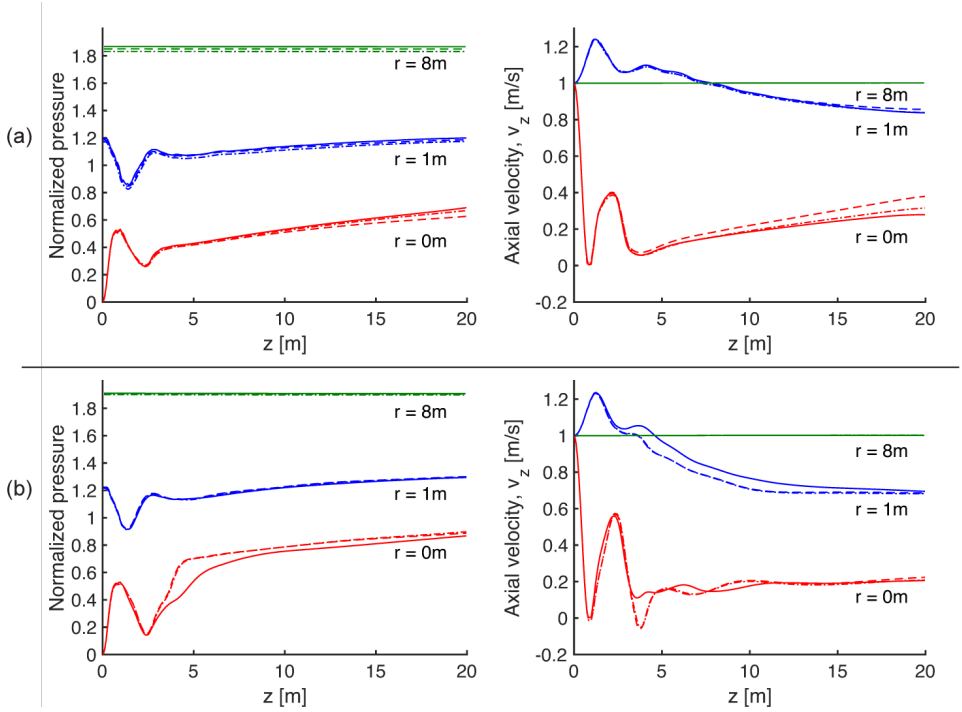

Figure 5.18: Time averaged pressure and axial velocity at different radial locations: (a) Time averaged from $t = 85$ to 95 s, when the bubble is developing; (b) Time averaged from $t = 600$ to 650 s, when the downstream instabilities are developed. Solid line: explicit FCT simulation, dashed line: implicit BIC simulation with $CFL_{wave} = 2.0$, and dash-dotted line: implicit BIC simulation with $CFL_{wave} = 60$.

5.4.1 Direct Comparison of Explicit and Implicit Calculations

We further isolate the cause of the differences between the explicit and implicit calculations by using the explicit and implicit algorithms to recompute the reference case with the same time-step size. A CFL_{wave} of 0.8 is used for both computations. The results show the same flow structure in both the implicit and explicit calculations. The resulting flow structure is shown in Fig. 5.19 from the explicit calculation. Same as the prior vortex breakdown calculations in this chapter, the vortex first undergoes the bubble mode, shown in Fig. 5.19a, then the spiral

mode, shown in Fig. 5.19b, and then double-helix mode, shown in Fig. 5.19c.

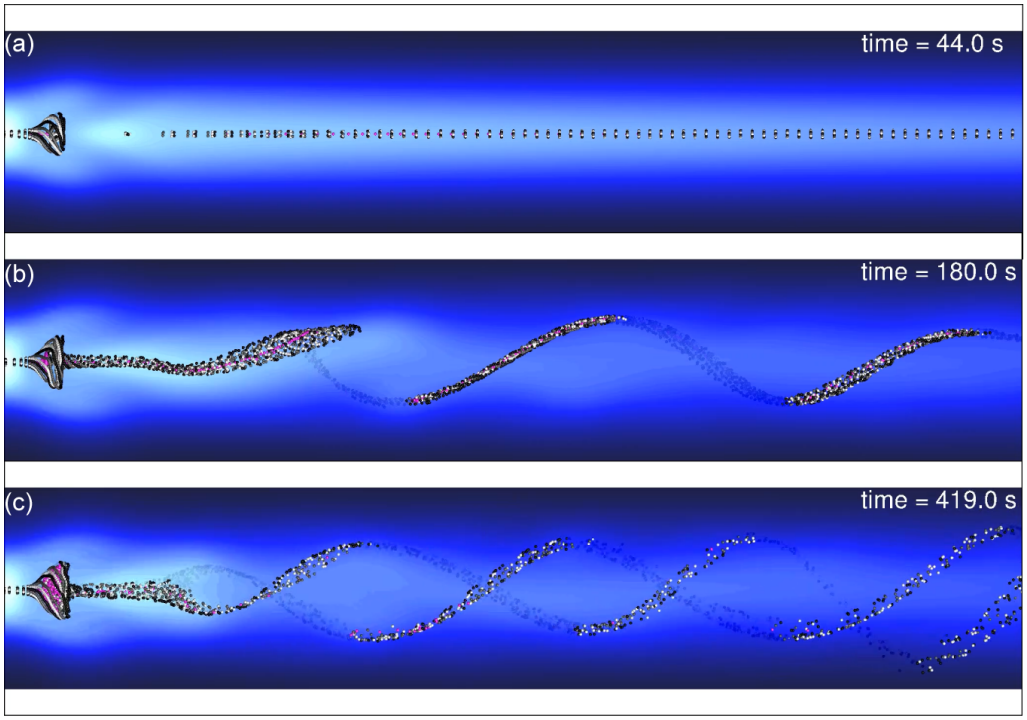

Figure 5.19: Streaklines imposed on contours of normalized pressure for the explicit FCT calculation of the reference case with $CFL_{\text{wave}} = 0.8$. The darker regions indicate higher pressure and the lighter regions indicate lower pressure. Time steps are selected to show the bubble mode, the spiral mode, and the double helix mode of vortex breakdown.

A comparison of the explicit and implicit calculations on the vortical structures of the three modes are shown in Fig. 5.20 and 5.21, corresponding to time $t = 146.6$ s and $t = 400.0$ s respectively. In these figures, the vortical structures are visualized by the vorticity iso-surfaces with normalized vorticity magnitude $|\omega| = 0.5$. Figure 5.20 shows a bubble mode at a upstream location with a spiral mode downstream in both the explicit and implicit calculations. The location, shape, and size of the bubbles are very similar in these two calculations. The downstream spiral mode also shows very good agreement in the sense of the shape and length. The misalignment of the

spiral motion, however, indicates that there is a phase difference between the explicit and implicit calculations. At a later time as shown in Fig. 5.21, the downstream spiral mode transitions into a double-helix mode in both cases. Similar to the phase difference of the spiral mode, this later time still exhibits a phase difference and thereby affects the rotational motion of the double-helix mode. The upstream bubble, however, maintains a similar shape and size comparing with Fig. 5.20, which also shows strong agreement between the explicit and implicit calculations.

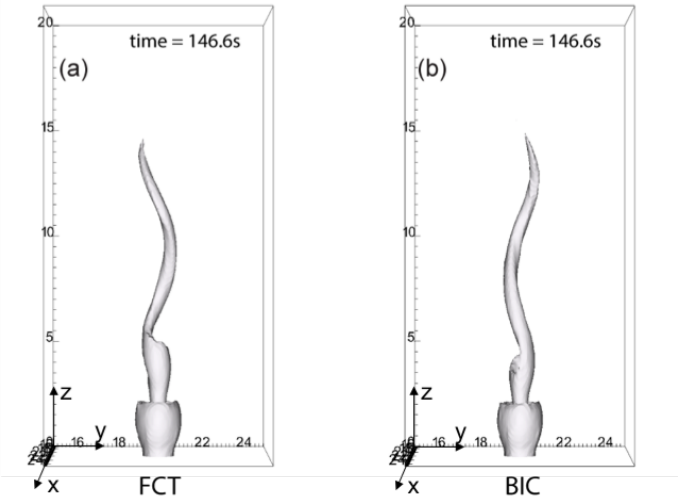

Figure 5.20: Vorticity iso-surface $|\omega| = 0.5$ for the explicit FCT and implicit BIC calculations with $CFL_{\text{wave}} = 0.8$ at time $t = 146.6$ s. The vorticity magnitude is normalized with the maximal value. Only a central section of the computational domain is shown.

A quantitative analysis is performed by extracting line data of the axial velocity and the pressure along the axial direction at different radial locations, and visualizing them over time. Figure 5.22 compares the axial velocity development along the vortex axis ($r = 0\,\text{m}$) for the explicit and implicit simulations. We discuss this figure from bottom to top as time develops, and from left to right as

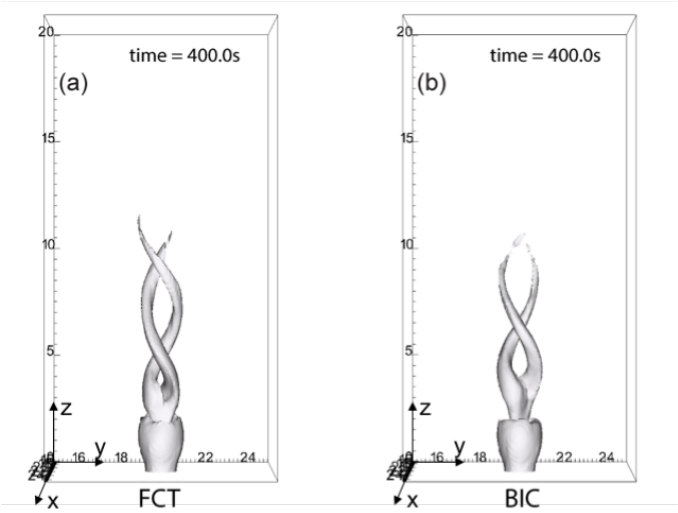

Figure 5.21: Vorticity iso-surface $|\omega| = 0.5$ for the explicit FCT and implicit BIC calculations with $CFL_{\text{wave}} = 0.8$ at time $t = 400.0$ s. The vorticity magnitude is normalized with the maximal value. Only a central section of the computational domain is shown.

from upstream to downstream. The flow is initialized with uniform axial velocity $v_z = 1\,\text{m/s}$, and it slowly decays in magnitude. Not long after the start, we observe a small negative axial velocity region near the upstream inflow location, which lasts through out the entire time period. This regions corresponds to the bubble mode breakdown, as indicated by the arrow with 'B' in Fig. 5.22 for both cases. Just downstream of the bubble, there is a small region with higher axial velocities, where the flow particles are injected out of the bubble with an acceleration into the downstream field. For both the explicit and implicit calculations, the results at this early stage from 0 s to about 110 s agree quite well with each other. In Fig. 5.22 (a) for the explicit calculation, from approximately 110 s to 220 s, oscillations form mainly due to the occurrence of the downstream spiral mode, and the transition from the spiral to the double-helix mode. At around 220 s, a second region with

negative axial velocity forms downstream of the acceleration zone, which indicates the bifurcation point of the double-helix structure. The double-helix mode is maintained through out the rest of the simulation, which is indicated by an arrow with 'H'. For the implicit calculation in 5.22 (b), oscillations form after about 110 s due to the development of secondary breakdown modes downstream. The occurrence of the double-helix mode, however, shows at a later time at around 280 s compared with the explicit calculation.

Figure 5.23 compares the pressure development along the vortex axis ($r = 0$ m) for the explicit and implicit simulations. The pressure is normalized in both cases. For this figure, we also discuss from bottom to top as time develops, and from left to right as from upstream to downstream. The time history of the pressure development is divided into three sections for both cases, as indicated by the white dashed lines and the numbers as section markers. For both simulations, the section 1 is an approximate time period from when the upstream bubble mode starts to form to when it is fully developed (refer to Fig. 5.19a). The second section is an approximate time period when the downstream spiral mode forms (refer to Fig. 5.19b) and starts to transition into the double-helix mode. Section 3 is approximately when the there is a steady state double-helix mode downstream (refer to Fig. 5.19c). In section 1, the pressure profile is initialized with a uniform distribution along the axial direction at the vortex center, and starts to increase downstream near the outflow boundary due to the decay of the vortex. This creates an adverse pressure gradient along the axial direction, which imposes a force on the flow particles against the traveling direction. When this force is so large to an extent that the momentum of the flow is

not sufficient to overcome it, the vortex column breaks down into the bubble mode. The explicit FCT and implicit BIC results show a similar trend of this development of the pressure gradient. The strength of the gradient, however, is smaller from the implicit calculation when compared with the explicit result. At a later time period in section 2, in general, the high pressure regions in both cases grow larger towards the upstream direction, which is due to the blockage effect of the bubble. Oscillations with a relatively high frequency are observed in this section, which is associated with the flow motion of the spiral mode. More differences in the two calculations, however, exist in this time period. Here, there are two major oscillations with lower frequencies in Fig. 5.19(b) for the implicit simulation at approximately 160 s and 240 s, whereas in Fig. 5.19(a) for the explicit simulation these oscillations are weaker with smaller amplitudes. In section 3, the flow is fully developed and reaches a quasi-steady state, where we see a periodical oscillation in the pressure field with a relatively low frequency. This oscillation is also observed by Ruith, Chen, Meiburg & Maxworthy in [27], where they refer to it as a pulsating bubble state since the bubble empities and refills itself, thereby shrinking and growing in size periodically. In both the explicit and implicit calculations, the period of this oscillation is similar, which is about 140 s. This is of the same order as observed in [27]. The phase of this oscillation, however, is not synchronized in our explicit and implicit calculations. This is consistent with the phase shift in the helical flow structures in Fig. 5.21, which actually shows up earlier in the spiral mode as discussed before for Fig. 5.20. It is also consistent with our observation in Fig. 5.22, where there is an earlier development of the secondary instability development downstream in the explicit

calculation than in the implicit one. This leads us to look back to the beginning of the simulations to determine the cause of this asynchronization.

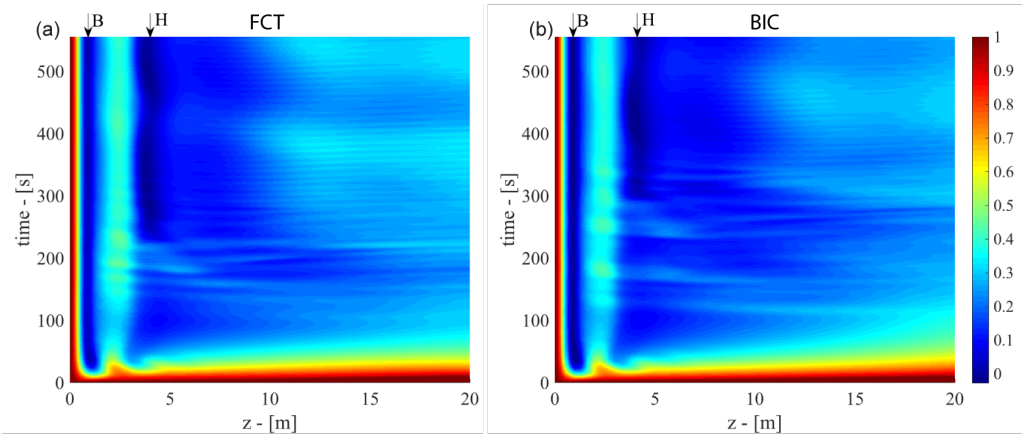

Figure 5.22: Time history of the axial velocity v_z along the vortex axis ($r = 0$m) for the explicit FCT and implicit calculations with $CFL_{\text{wave}} = 0.8$. The arrow with 'B' indicates the location of the bubble mode, and the arrow with 'H' indicates the location of the bifurcation point of the double-helix mode.

We therefore focus on the first 20 s of the calculations. In order to better visualize the pressure wave propagation along the axial direction, we take the same datasets used in figure 5.23 and normalize them by applying $P(z,t_i) = \frac{P(z,t_i) - \text{mean}(P(z,t_i))}{\text{mean}(P(z,t_i))}$ for all time steps t_i. The results for the first 20s are shown in figure 5.24 for both calculations, with black dashed lines on top indicating the first major pressure wave propagation from upstream to downstream. For the regions below the black dashed lines, the flow field has not felt the pressure wave coming from the upstream yet, where the pressure increases with a uniform rate across the axial locations due to the vortex dissipation. For regions above the black dashed lines and below around 10s, the flow here has experienced the pressure wave traveling downstream, but before the wave reaches the outflow boundary and reflects back. Due to the wave effect,

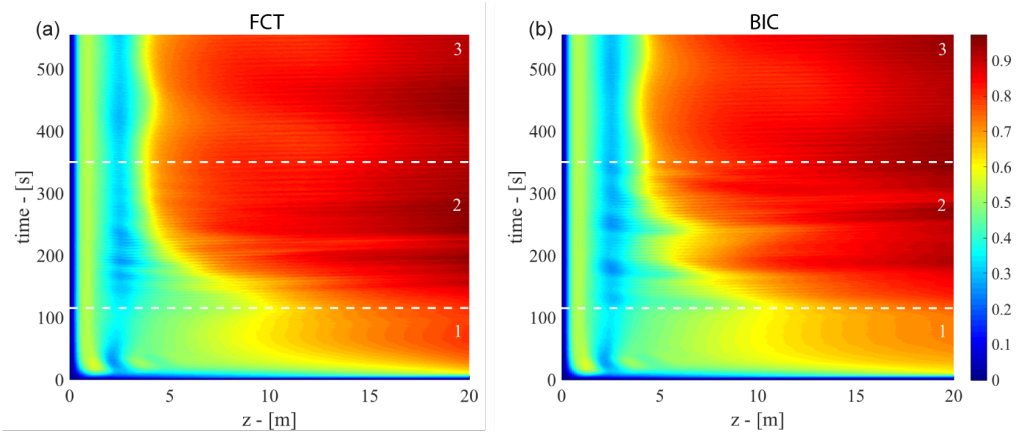

Figure 5.23: Time history of the normalized pressure along the vortex axis ($r = 0$m) for the explicit FCT and implicit calculations with $CFL_{\text{wave}} = 0.8$. The time history is divided into three sections based on the flow development indicated by the white dashed lines and the associated numbers.

the pressure in this region increases with a different rate as before. There is a time delay at different axial locations of this change of rate, since the wave propagates at a finite speed. In general, the regions before 10s in both calculations show strong agreement with each other. After the wave interacts with the outflow boundary, we observe some clearer differences in the pressure field between the explicit and implicit simulations. From this figure, the differences mainly show up near the outflow boundary, where the pressure is higher in the explicit calculation than in the implicit one. This leads us to speculate that it is the difference between how the explicit FCT and implicit BIC are couple to the outflow boundary condition that causes the difference in the pressure field, and further affects the phase of the instabilities.

To confirm this, we extract the time history of pressure from Fig. 5.23 at axial locations $z = 10\,\text{m}$ and $z = 20\,\text{m}$ for the first $30\,\text{s}$, and compare them in Fig. 5.25 for both cases. In this figure, we go from the left to the right as advancing

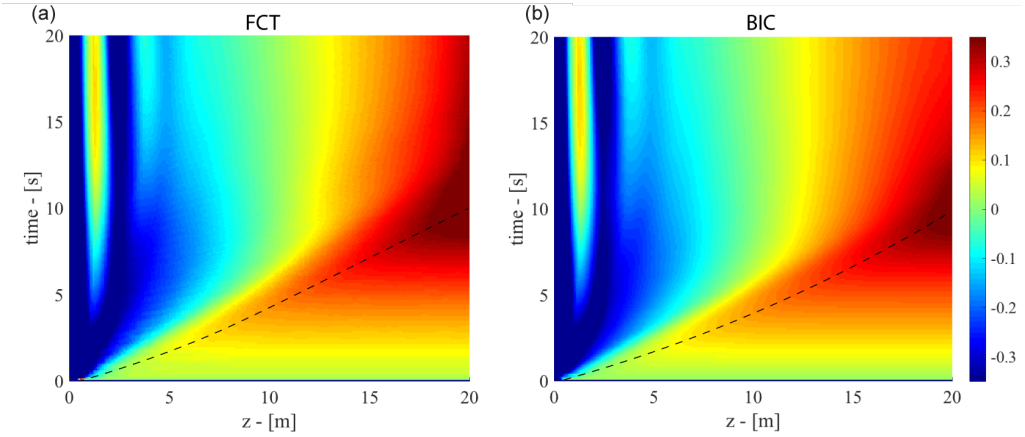

Figure 5.24: Time history of the pressure along the vortex axis ($r = 0$m) normalized by $P(z,t_i) = \frac{P(z,t_i) - \text{mean}(P(z,t_i))}{\text{mean}(P(z,t_i))}$ for all time steps t_i, for the explicit FCT and implicit calculations with $CFL_{\text{wave}} = 0.8$. The black dashed lines indicate the approximate propagation paths of the first major pressure wave.

in time, and discuss the three important time stages that are marked as 'A', 'B', and 'C'. From the beginning to time A, the pressure wave travels from upstream to downstream before reaching $z = 10\,\text{m}$. The pressure at $z = 10\,\text{m}$ and $z = 20\,\text{m}$ both rises with a same rate due to the uniform vortex dissipation, as discussed above. Note that the explicit and implicit results agree very well at both locations. At time A, the pressure wave arrives at $z = 10\,\text{m}$, therefore the slope of the pressure profile at $z = 10\,\text{m}$ changes due to the wave influence. At this time, no significant changes occur in the rate of the pressure increase at $z = 20\,\text{m}$. From time A to time B, the pressure wave is traveling from $z = 10\,\text{m}$ to $z = 20\,\text{m}$ before it reaches the boundary, during which the explicit and implicit results maintain strong agreements at both axial locations. At time B, the pressure wave arrives at $z = 20\,\text{m}$, which is at the outflow boundary. Similarly, the slope of the pressure profile for $z = 20\,\text{m}$ changes under the wave effect. A deviation of the BIC curve from the FCT curve at

$z = 20\,\mathrm{m}$, however, occurs when this wave interacts with the boundary and reflection effects start to occur in the domain. This deviation results in a growing discrepancy between the BIC and FCT results as the time grows. From time B, the influence from the outflow boundary starts to propagate back into the domain. Note that before it reaches $z = 10\,\mathrm{m}$ at time C, the explicit and implicit results at $z = 10\,\mathrm{m}$ follow closely with each other over time. Once it passes $z = 10\,\mathrm{m}$ after time C, we observe a similar deviation between the two calculations at $z = 10\,\mathrm{m}$ as time grows. The discrepancy is smaller compared with that at $z = 20\mathrm{m}$, but at both locations, the explicit calculation predicts a larger pressure gradient than that from the implicit calculation. This larger pressure gradient downstream of the bubble may be the main reason that causes the secondary instabilities (the spiral and the double-helix modes) to occur earlier than in the implicit calculation, which is essentially the origin of the phase difference in the downstream motions discussed above. This discrepancy is essentially from the difference of how the implicit algorithm handles the open outflow boundary through an elliptic solver, versus the explicit algorithm by using an explicit FCT solver. Note that the flow upstream of the bubble is not affected by this pressure wave difference. This to some extent confirms the theory that, the bubble mode is a critical state where no waves could propagate further upstream, which separates the flow from an upstream supercritical state to a downstream subcritical state.

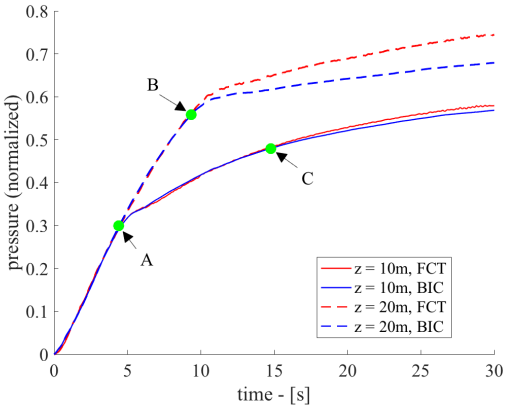

Figure 5.25: Normalized pressure data extracted at two locations: (1) radial location $r = 0$m, axial location $z = 10$m, and (2) radial location $r = 0$m, axial location $z = 20$m for the first 30 seconds from both explicit FCT and implicit BIC calculations with $CFL_{\text{wave}} = 0.8$..

5.5 Discussion

There are several important features of applying the BIC procedure to an explicit solution of the NS equations. From our experience of using this algorithm, we have identified important points worth discussing. Below, we discuss the residual numerical diffusion after the antidiffusion stage in LCPFCT, use of LCPFCT as a spatial high-frequency filter, details of algorithm coupling, the comparison of explicit and implicit calculations, the importance of the equation of state, and future directions.

5.5.1 The Residual Numerical Diffusion after the Antidiffusion Stage in LCPFCT

In the application of BICFCT to the 1D convection of a sinusoidal density profile, we showed that the error after convection does not converge with decreasing time-step size. This is because the residual numerical diffusion after the antidiffusion stage sometimes does not decrease as the time step Δt decreases. To see where this residual numerical diffusion comes from, we need to revisit the steps in FCT, and rewrite the final solution in Eq. 3.5 in the finite difference approximation form. For simplicity, we consider the 1D form of Eq. 3.5, which is equivalent to Eq. 3.22 in [106]. Here we rewrite it as

$$\mathbf{R}_i^n = \widetilde{\mathbf{R}}_i - (\mathbf{F}^C_{i+\frac{1}{2}} - \mathbf{F}^C_{i-\frac{1}{2}}), \tag{5.10}$$

where the low order solution $\widetilde{\mathbf{R}}_i$ is the convected and diffused solution. The corrected flux is then added to the low-order solution to cancel the numerical diffusion as much as possible while not enhancing the original local extrema. The corrected fluxes $\mathbf{F}^C_{i+\frac{1}{2}}$ and $\mathbf{F}^C_{i-\frac{1}{2}}$ are determined using a flux limiter. In 3D, the limiter is Eq. 3.46 in Chapter 3. The equivalent 1D form of the flux limiter is given in [106] as Eq. 3.21. Here we rewrite it as

$$\mathbf{F}^C_{i+\frac{1}{2}} = S_{i+\frac{1}{2}} \max\left[0,\ \min\left(\left|\mathbf{F}^{ad}_{i+\frac{1}{2}}\right|, S_{i+\frac{1}{2}}\left(\widetilde{\mathbf{R}}^x_i - \widetilde{\mathbf{R}}^x_{i-1}\right), S_{i+\frac{1}{2}}\left(\widetilde{\mathbf{R}}^x_{i+2} - \widetilde{\mathbf{R}}^x_{i+1}\right)\right)\right], \tag{5.11}$$

Notice that the flux limiter actually chooses one among the three terms as the corrected flux in Eq. 5.11. Different amount of residual numerical diffusion is introduced to the local solution when the limiter chooses different terms.

First, we check the residual diffusion assuming the flux limiter chooses the first term, that is $\mathbf{F}^C_{i+\frac{1}{2}} = \mathbf{F}^{ad}_{i+\frac{1}{2}}$ and $\mathbf{F}^C_{i-\frac{1}{2}} = \mathbf{F}^{ad}_{i-\frac{1}{2}}$. We can then write the final solution as

$$\mathbf{R}_i^n = \widetilde{\mathbf{R}}_i - (\mathbf{F}^C_{i+\frac{1}{2}} - \mathbf{F}^C_{i-\frac{1}{2}}) \tag{5.12}$$

$$= \mathbf{R}_i^o - \frac{\epsilon_x}{2}\left(\mathbf{R}^o_{i+1} - \mathbf{R}^o_{i-1}\right) + \nu_x^{(1)}\left(\mathbf{R}^o_{i-1} - 2\mathbf{R}^o_i + \mathbf{R}^o_{i+1}\right) - (\mathbf{F}^{ad}_{i+\frac{1}{2}} - \mathbf{F}^{ad}_{i-\frac{1}{2}}) \tag{5.13}$$

$$= \mathbf{R}_i^o - \frac{\epsilon_x}{2}\left(\mathbf{R}^o_{i+1} - \mathbf{R}^o_{i-1}\right) + \nu_x^{(1)}\left(\mathbf{R}^o_{i-1} - 2\mathbf{R}^o_i + \mathbf{R}^o_{i+1}\right) - \left(\mu_x(\mathbf{R}^T_{i+1} - \mathbf{R}^T_i) - \mu_x(\mathbf{R}^T_i - \mathbf{R}^T_{i-1})\right) + \nu_x^{(2)}\left(\mathbf{R}^o_{i-1} - 2\mathbf{R}^o_i + \mathbf{R}^o_{i+1}\right) \tag{5.14}$$

$$= \mathbf{R}_i^o - \frac{\epsilon_x}{2}\left(\mathbf{R}^o_{i+1} - \mathbf{R}^o_{i-1}\right) + \left(\nu_x^{(1)} + \nu_x^{(2)}\right)\left(\mathbf{R}^o_{i-1} - 2\mathbf{R}^o_i + \mathbf{R}^o_{i+1}\right) - \mu_x(\mathbf{R}^T_{i+1} - 2\mathbf{R}^T_i + \mathbf{R}^T_{i-1}) \tag{5.15}$$

$$= \mathbf{R}_i^o - \frac{\epsilon_x}{2}\left(\mathbf{R}^o_{i+1} - \mathbf{R}^o_{i-1}\right) + \left(\nu_x^{(1)} + \nu_x^{(2)}\right)\left(\mathbf{R}^o_{i-1} - 2\mathbf{R}^o_i + \mathbf{R}^o_{i+1}\right) - \mu_x\left[\mathbf{R}^o_{i-1} - \frac{\epsilon_x}{2}\left(\mathbf{R}^o_i - \mathbf{R}^o_{i-2}\right) - 2\left[\mathbf{R}^o_i - \frac{\epsilon_x}{2}\left(\mathbf{R}^o_{i+1} - \mathbf{R}^o_{i-1}\right)\right] + \mathbf{R}^o_{i+1} - \frac{\epsilon_x}{2}\left(\mathbf{R}^o_{i+2} - \mathbf{R}^o_i\right)\right] \tag{5.16}$$

As the time step Δt approaches zero, the solution at the new time step $\mathbf{R}_i^n$ should be equal to the solution at the old time step $\mathbf{R}_i^o$ if the numerical discretization introduces no residual numerical diffusion. When Δt approaches to zero, all of the terms with the CFL number ϵ_x becomes zero. With this assumption, Eq. 5.16 can

be simplified to

$$\mathbf{R}_i^n = \mathbf{R}_i^o + \left(\nu_x^{(1)} + \nu_x^{(2)} - \mu_x\right)\left(\mathbf{R}_{i-1}^o - 2\mathbf{R}_i^o + \mathbf{R}_{i+1}^o\right). \tag{5.17}$$

Here the values of $\nu_x^{(1)}$, $\nu_x^{(2)}$, and μ_x are given in Eq. 3.58 - 3.60 for 1D and 2D and in Eq. 3.39-3.42 for 3D. Although the values for $\nu_x^{(1)}$ and $\nu_x^{(2)}$ are different for 1D, 2D, and 3D, when the CFL number ϵ_x approaches zero, the following equation applies to 1D, 2D, and 3D:

$$\nu_x^{(1)} + \nu_x^{(2)} = \frac{1}{6}, \tag{5.18}$$

$$\mu_x = \frac{1}{6}. \tag{5.19}$$

Therefore, the second term on the right hand side of Eq. 5.17 becomes zero, which gives

$$\mathbf{R}_i^n = \mathbf{R}_i^o \tag{5.20}$$

when Δt approaches zero. This means that when the flux limiter chooses the first term, that is $\mathbf{F}_{i+\frac{1}{2}}^{ad}$, there is no residual numerical diffusion in the local solution as Δt approaches zero.

When the flux limiter chooses the second or the third term in Eq. 5.11, however, there is residual diffusion in the local solution that is not a function of Δt, which prevents the error from converging in time. This can be shown here as an example

when the flux limiter chooses the second term, which is $\mathbf{F}^C_{i+\frac{1}{2}} = \widetilde{\mathbf{R}}^x_i - \widetilde{\mathbf{R}}^x_{i-1}$ and $\mathbf{F}^C_{i-\frac{1}{2}} = \widetilde{\mathbf{R}}^x_{i-1} - \widetilde{\mathbf{R}}^x_{i-2}$. We can then write the final solution as

$$\mathbf{R}^n_i = \widetilde{\mathbf{R}}_i - (\mathbf{F}^C_{i+\frac{1}{2}} - \mathbf{F}^C_{i-\frac{1}{2}}) \tag{5.21}$$

$$\begin{aligned} &= \mathbf{R}^o_i - \frac{\epsilon_x}{2}\left(\mathbf{R}^o_{i+1} - \mathbf{R}^o_{i-1}\right) + \nu^{(1)}_x\left(\mathbf{R}^o_{i-1} - 2\mathbf{R}^o_i + \mathbf{R}^o_{i+1}\right) \\ &\quad - (\mathbf{F}^{ad}_{i+\frac{1}{2}} - \mathbf{F}^{ad}_{i-\frac{1}{2}}) \end{aligned} \tag{5.22}$$

$$\begin{aligned} &= \mathbf{R}^o_i - \frac{\epsilon_x}{2}\left(\mathbf{R}^o_{i+1} - \mathbf{R}^o_{i-1}\right) + \left(\nu^{(1)}_x + \nu^{(2)}_x\right)\left(\mathbf{R}^o_{i-1} - 2\mathbf{R}^o_i + \mathbf{R}^o_{i+1}\right) \\ &\quad - \left((\widetilde{\mathbf{R}}^x_i - \widetilde{\mathbf{R}}^x_{i-1}) - (\widetilde{\mathbf{R}}^x_{i-1} - \widetilde{\mathbf{R}}^x_{i-2})\right). \end{aligned} \tag{5.23}$$

When Δt approaches zero, Eq. 5.23 can be simplified as

$$\begin{aligned} \mathbf{R}^n_i = \mathbf{R}^o_i &+ \frac{1}{6}\underline{\left(\mathbf{R}^o_{i-1} - 2\mathbf{R}^o_i + \mathbf{R}^o_{i+1}\right)} \\ &- \frac{1}{6}\underline{\left(\mathbf{R}^o_{i-3} + 2\mathbf{R}^o_{i-2} - 6\mathbf{R}^o_{i-1} + 2\mathbf{R}^o_i + \mathbf{R}^o_{i+1}\right)}. \end{aligned} \tag{5.24}$$

The second and the third terms underlined on the right hand side of Eq. 5.24 are essentially the upwind finite difference approximation form of second order and fourth order derivatives of the solution profile $\mathbf{R}^o$. Therefore, we can rewrite Eq. 5.24 as

$$\begin{aligned} \mathbf{R}^n_i = \mathbf{R}^o_i &+ \underline{\frac{1}{6}\frac{d^2R}{dx^2}\bigg|_i [-1,0,1]} \\ &\underline{- \frac{d^2R}{dx^2}\bigg|_i [-2,-1,0] - \frac{1}{6}\frac{d^4R}{dx^4}\bigg|_i [-3,-2,-1,0,1]}, \end{aligned} \tag{5.25}$$

in which the stencils used for the derivative approximation are included in square brackets. The first underlined term is a second order diffusion that is introduced at

the diffusion stage in FCT which guarantees monotonicity. The second underlined term contains a second order and a fourth order antidiffusion, which reduces the added numerical diffusion, but does not cancel it completely. The residual diffusion which is underlined in Eq. 5.25 is not a function of Δt, which means the residual diffusion does not vanish as Δt approaches zero. When the flux limiter chooses this combination for the corrected flux, the error does not converge in time.

When the flux limiter chooses the third term in Eq. 5.11, the resulting residual diffusion has the same derivatives as in Eq. 5.25, except approximated using different stencils. The residual diffusion does not vanish as Δt approaches zero either and the error does not converge in time. The details of the derivation are not shown here.

Ideally, if the flux limiter chooses the first term in Eq. 5.11 at every grid point in the convection calculation, there would be no residual numerical diffusion in the solution and the error of convection should converge in time. When there is changes in monotonicity in the solution profile, that is when the solution profile that is convected contains extremum, however, the flux limiter has to choose the second or third term in Eq. 5.11 near the extremum to ensure the original extremum is not enhanced and no new unphysical maximum or minimum is created. Therefore, the error of convection does not vanish when using small Δt and sometimes the error can even be larger than that using a large Δt. The errors from smaller time steps, however, are not expected to be an issue because larger time steps are preferable when using BICFCT to take advantage of BICFCT's computational efficiency for low-Mach-number flows.

5.5.2 The Filter

We have shown that the new BIC algorithm is stable when the implicit time step is considerably larger than the time step required by the explicit stability limit. Nonetheless, when the time step is too large, numerical oscillations can occur in the solution. A high-frequency filter is necessary in order to control the major numerical instabilities, and therefore to stabilize the calculation while maintaining the accuracy.

The filter used here is an extra FCT step. In previous work [116, 120], the FCT algorithm has been used as a post-processing filtering operation to extract a solution from a very noisy direct simulation Monte Carlo calculation. As the effect of the filtering as a post-processing tool is essentially to smooth local peaks in the data, this application inspired us to use FCT as a spatial filter during the calculation to control numerical noise. The details of the filtering process are discussed in [116].

The effect of the steps in FCT is first to smooth local peaks in the data, which alters the local value of ρ and the value of its neighbors. Then, in the limited antidiffusion step, the neighbors keep values closer to their original values, but the peak remains smoothed. The practical result of these steps is a high-frequency filter with some useful properties, as shown in Fig. 5.26. Here a square wave, propagating at zero velocity, is passed through the FCT algorithm using a uniform grid, as shown in Fig. 5.26*a*. The result is that the square wave is unaltered by FCT, up to numerical round off. Next, if a random spectrum of high-frequency noise is superimposed on the square wave, as shown in Fig. 5.26*b*, FCT reduces the noise while rigorously

conserving ρ. During this process, the quantity ρ is convected at zero velocity. The noise in the profile is smoothed by the residual diffusion after the antidiffusion stage shown in Eq. 5.25 when the flux limiter chooses the second or third terms in Eq. 5.11. The comparison of the results after 5000 and 20,000 passes shows that the less noisy solution stops changing as the number of filter passes increases. This is because the flux limiting step eliminates local extrema on neighboring points. After these points are smoothed, the limiter chooses the first term in in Eq. 5.11, which does not affect the solution as shown in Eq. 5.20 when convection speed is zero, thereby stopping the effects of the filtering.

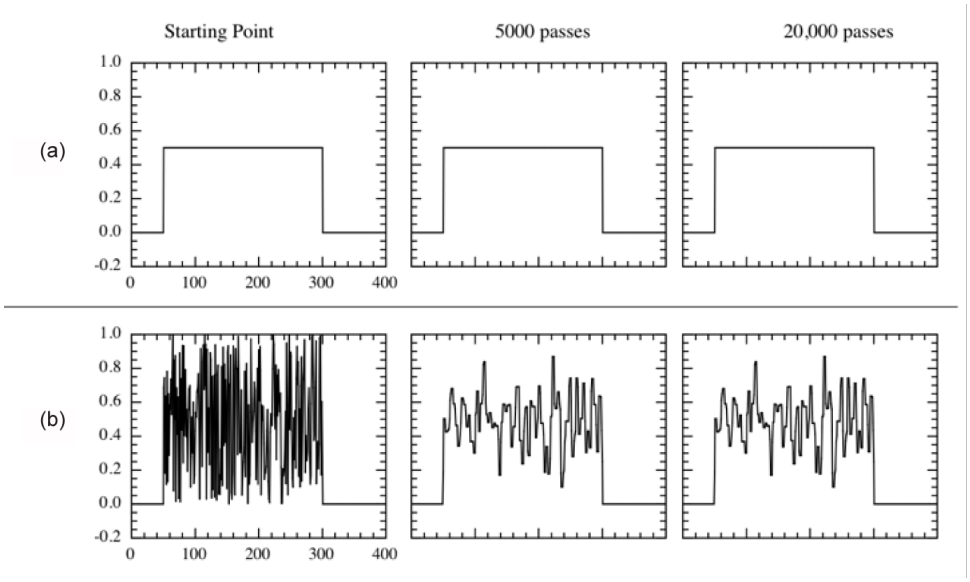

Figure 5.26: Reprinted from [116]. Application of FCT filter to square wave. Plain square wave (panel a) and one that has been superimposed with random noise (panel b) are passed through FCT with $\mathbf{V} = 0$. The starting point and the results after 5000 and 20,000 passes through the FCT filter are shown for both cases.

In theory, any high-frequency spatial filter that could help control high-frequency oscillations should work just as well. When the BIC algorithm is combined with

FCT, however, using the FCT routine itself as a filter reduces the complexity of implementation.

5.5.3 The Coupling of BIC with Explicit Algorithms

It is also important to examine the interface between the combined BIC and explicit algorithm, and not only their separate inherent features. An example is the effect of a multiplicative coefficient that is introduced in FCT. This coefficient was introduced to add a very small amount of numerical diffusion in every time integration step, so that no local existing extrema will be enhanced and therefore the monotonicity is ensured. Although the influence of this coefficient was well studied for explicit calculations [121], it affects the results in a different way when BIC is applied.

The amount of the numerical diffusion has been quantified in [121] for explicit FCT. Here, we have seen that when FCT is combined with BIC, the total amount of the numerical diffusion decreases with larger implicit time steps. This is attributed to the inherent benefit of BIC simply having a larger time step: that is, the total number of time integration steps is reduced by using larger time steps to march towards the target physical time. Although the numerical diffusion in FCT imposed by this coefficient is very small, the effect is not negligible when it is close in value to the physical viscosity. Using BIC when it is possible provides a noticeably better result especially when a quantitatively accurate solution is required.

The performance of BIC discussed in this work is based on the combination

of BIC with FCT. When BIC is applied to other methods, the influence of the interface between them should be carefully examined in the analysis of the overall performance and the interpretation of the results.

5.5.4 Comparison of Explicit and Implicit Calculations

We have compared the results obtained from explicit FCT and implicit BIC calculations side by side for the 2D doubly periodic shear layers problem and the 3D vortex breakdown problem. In both cases, the implicit calculations show excellent agreement with the explicit solutions. The accuracy of the solutions from BIC is shown to be robust using time steps varying from near the explicit stability limit to hundreds of times larger.

Closer examinations of the implicit calculations with large time steps in the 2D doubly periodic shear layers problem show some additional numerical diffusion compared with the explicit solution. In this case, we see a slightly faster decay of the total enstrophy and the kinetic energy when using lager implicit time steps. The additional diffusion observed in the BIC simulations is possibly related to the relatively less accurate elliptic solver for the pressure correction when compared with the fourth-order accurate FCT. This implies that even when a high-order monotone algorithm is used for the explicit prediction, the overall spacial accuracy could be limited by the choice of the elliptic solver for the implicit correction. In this work, we use a second-order discretization for the Laplacian-like term in the elliptic equation 4.8, and a 3-point stencil for each dimension for the elliptic solver from the Boxlib

library. A higher order discretization stencil and a more accurate elliptic solver can be used in future applications.

5.6 Summary and Conclusions

For the computation of low-Mach-number flows, we have presented a new BIC algorithm based on the original BIC introduced in [20, 23]. The original BIC algorithm proposed a solution procedure that includes an explicit predictor step to solve the convective portion of the Navier-Stokes equations and an implicit corrector step to remove the acoustic limit on the CFL condition. The explicit predictor uses a high-order monotone algorithm while the implicit corrector solves an elliptic equation for a pressure correction to equilibrate acoustic waves. The modification described in this work has several new features. These are: (1) a modification of the energy correction, and (2) a filter step that is operated on all of the conserved variables to remove spurious oscillations. Another contribution in this work is the description of the integration procedure of BIC with the terms that represent physical diffusion processes. The performance of BIC was tested by combining it with a fourth-order monotone FCT algorithm. A sinusoidal density profile is convected and three swirling flows with successively increased difficulty are modeled.

First, a sinusoidal density profile was convected in 1D and the solution was compared against an exact solution to assess BIC's spatial and temporal order of convergence. The error analysis showed that BIC is second-order convergent in space and it is not convergent in time. The errors from smaller time steps are larger than

errors from larger time steps. Further analysis showed that the reason for the non-convergence in time comes from the residual numerical diffusion at certain locations which does not vanish to zero as time-step size decreases. This residual numerical diffusion comes from the flux-limiting step of FCT and it is introduced into the solution where there is monotonicity change in the local solution profile. The errors from smaller time steps, however, are not expected to be an issue because larger time steps are preferable when using BICFCT to take advantage of its computational efficiency for low-Mach-number flows.

Second, a flow in a 2D enclosed cavity with a moving upper wall is simulated using various implicit time steps. This case is selected to demonstrate the ability of BIC on solving steady-state swirling flows. The solutions obtained using BIC are compared with results from an incompressible calculation [24]. In this case, we obtain good agreements for CFL_{wave} number of at least 100.

The third test problem is the evolution of two shear layers into large vortices in a 2D periodic domain. This case is simulated to examine the behavior of BIC when solving transient flows with strong vorticity gradients. For this case, comparisons between explicit FCT and implicit BIC calculations are presented side by side. The accuracy of the solutions using BIC are shown to be robust using time steps varying from near the explicit stability limit to hundreds of times larger. The CFL_{wave} number exceeds 100 before there are even small differences. The solutions from the BIC calculations also show excellent agreement when compared to other algorithms [25, 26]. A closer examination on the time history of total enstrophy and the total kinetic energy shows a slightly faster decay of both when a larger time step is used.

This additional diffusion is possibly from the relatively lower-order solution of the pressure correction term in BIC compared with the fourth-order explicit FCT. This shows that the choice of the multigrid solver for the elliptic equation can limit the overall spatial accuracy of the algorithm, although high-order explicit methods are used.

The fourth test problem is a 3D vortex breakdown with an inflow-outflow boundary condition, which tests BIC on predicting the instabilities that occur in swirling jet flows. The bubble modes predicted by BIC with different time steps agree closely with the one obtained from the explicit FCT calculation, in terms of both shape and location. The comparison also shows that BIC is able to predict the downstream spiral mode and the double-helix mode, and capture the transition from one to another, although BIC predicts a stronger deceleration at the double-helix bifurcation point. Direct comparisons of the implicit and explicit calculations were made using the same CFL_{wave}. The results show a phase difference in the rotational motion of the downstream double helix. Further analysis of the pressure waves showed that differences in the flow occurred after the initial pressure wave reached the outflow boundary. This difference led to the phase difference of the double helix and it comes from how BIC and explicit FCT handle the outflow boundary differently.

A spatial filter is sometimes necessary to eliminate high-frequency numerical oscillations and therefore stabilizes the calculations when using large implicit time steps. Fourth-order monotone FCT, used here as the routine for solving convective fluxes, is suggested as a convenient choice for such a required filter. The FCT

algorithm could serve as a filter which reduces the complexity of implementation as one FCT routine could work for two purposes. Moreover, it is conservative, and does not require extra tuning or optimization for most applications.

Potential future improvements include the generalization of the pressure correction to account for different equations of states, and an algorithm that transitions between BICFCT and explicit FCT to simulate flows that cover a range of Mach numbers.

Chapter 6: Application - Sensitivity of Vortex Breakdown on Heat Release and Heat Extraction Effects

6.1 Introduction

In this chapter, we investigate the effects of heat release and heat extraction on vortex breakdown using the BICFCT algorithm. To date, there have been only a few studies on the heat-release effects on vortex breakdown. The experiment by Rukes et al. [89, 90] applied heating to the bubble mode of vortex breakdown in air by placing a heated, coiled wire within a vortex undergoing vortex breakdown. They focused on the effects of heating on PVC. A numerical study by Gorbunova et al. [91] employed a simplified, confined configuration of swirling flow and applied a source of heat around the vortex axis. They focused on the impact of heat release on the amplitude and frequency of PVC. The mechanism of how PVC is affected by heat release effects, however, is still not clear. Changes of the dynamics and modes of vortex breakdown undergoing heat release could play a role in the mechanism so that further study is needed to help find the answer. In this work, we present a fundamental study of heat-release and heat-extraction effects on the dynamics of vortex breakdown and the transition of modes.

6.2 Governing Equations

We solve the 3D unsteady compressible NS equations described in Eqs. 4.20 to 4.23 with an additional source term Q in the energy equation,

$$\frac{\partial E}{\partial t} = -\nabla \cdot ((E + P)\,\mathbf{V}) - \nabla \cdot (\mathbf{V} \cdot \hat{\tau}) - \nabla \cdot (K \nabla T) + Q. \tag{6.1}$$

This additional Q is included in the FCT solution procedure through the D_4 source in Eq. 3.1, written here as

$$\mathbf{D_4} = \begin{bmatrix} 0 \\ 0 \\ 0 \\ 0 \\ Q \end{bmatrix}. \tag{6.2}$$

The energy change rate Q is positive for heat release and negative for heat extraction. The source term $\mathbf{D_4}$ is incorporated through FCT by Eq. 3.34 into the BICFCT integration procedure at the explicit predictor step (step 3 in section 4.4.2). If the time integration procedure in section 4.4.2 is followed, at the explicit predictor step, the term S in Eq. 4.11 should now consist of the change of total internal energy due to diffusion and the defined value Q. The details of how BICFCT handles energy release from combustion is described in [3].

The heat diffusivity is assumed to have the following temperature dependence,

$$\alpha = \alpha_0 \frac{T^{0.7}}{\rho}, \tag{6.3}$$

where α_0 is constant. The viscosity μ is given by

$$\mu = Pr\alpha\rho, \tag{6.4}$$

where Pr is the Prandtl number. The viscosity is shown to have the same temperature dependence after substituting in Eq. 6.3,

$$\mu = Pr\alpha_0 T^{0.7}. \tag{6.5}$$

The heat conductivity is given as

$$K = \alpha\rho C_p, \tag{6.6}$$

where C_p is the heat capacity at constant pressure. After substituting in Eq. 6.3, the heat conductivity is expressed as

$$K = C_p\alpha_0 T^{0.7}. \tag{6.7}$$

6.3 Initial Conditions, Boundary Conditions, and Geometrical Setup

We initialize the flow with the axisymmetric, columnar Grabowski vortex profile through out the whole domain, which is same as the initial condition used for the vortex breakdown test cases in Chapter 5. The profiles of the azimuthal, radial, and axial velocities are presented as Eq. 5.2 - 5.6. The pressure profiles are in Eq. 5.8 - 5.8. The swirl number is defined as $S = v_\theta(R)/v_{z,\infty}$, where R is the radius of the vortex core, and the Reynolds number is $Re = v_{z,\infty}R/\nu$.

For all the calculations, a rectangular-prism domain is used with boundary conditions the same as described in Chapter 5. Using the computational domain for the heat-release cases shown in Fig. 6.1 as an example, an inflow condition is imposed on the lower axial x-y plane with the Grabowski vortex profile as described above. The upper axial x-y plane is treated as nonreflecting. The pressure is controlled at the lateral boundaries by the Bernoulli's equation, since the flow is assumed to be irrotational outside of the vortex core. This boundary pressure is then calculated by $P = P_\infty - \rho V^2/2$, where V is the magnitude of the velocity. The velocity at the lateral boundaries are specified using Eq. 5.3. For the temperature of the flow leaving the boundaries, we apply first order extrapolation with the derivative normal to the boundary. For flow coming into the boundary, we specify the temperature using the ideal gas law with fixed air density. For the heat-addition cases, we apply an inflow air density 1.177 kg/m^3 which yields an inflow temperature of 300 K at 1 atm. For the heat extraction cases, we use inflow air density at 0.2941 kg/m^3 which yields a temperature of 1200 K at 1 atm. For all of the calculations in this

Chapter, $\mathrm{CFL}_{\mathrm{fluid}} = 0.3$ is used.

For the calculations with heat addition, we initialize the flow with air properties at 300 K and 1 atm. These air properties are the thermal conductivity $K = 2.624 \times 10^{-5}$ kW/m K, specific heat ratio $\gamma = 1.4$, molecular weight $M_w = 28.97$ kg/kmol, and Prandtl number $Pr = 0.707$. To compute the temperature scaling of the heat diffusivity α, the constant α_0 in Eq. 6.3 can be calculated using Eq. 6.7. We first calculate a baseline flow with $Re = 300$, $S = 1.3$ and, $\alpha = 1$, which is same as the vortex breakdown test cases in Chapter 5. Here we set the radius of the vortex core $R = 0.00635$ m so that the resultant $v_{z,\infty}$ from the definition of Re is not so fast that the low-Mach-number assumption is no longer valid and not too slow that the flow takes too long to develop. A 0.254 m $\times$ 0.254 m $\times$ 0.127 m computational domain is employed as shown in Fig. 6.1a, in which we define the z-axis as the axial direction. The mesh is Cartesian with four levels of refinement encompassing the vortex core as shown in Fig. 6.1a. The cell width is halved for each level. The finest cell size is $\Delta x = 0.254/512 = 4.96 \times 10^{-4}$ m. The refinement does not change during the calculation.

After the baseline flow for the heat addition cases reaches the quasi-steady state, it develops a bubble mode upstream and a double-helix mode downstream, as shown in the axial velocity field in Fig. 6.1b (the detailed flow structure is described in the following section). Heat addition is then introduced into a specified volume in the flow. An enlarged view of the region with heat input is shown in Fig. 6.1c. The heat-addition region is a cylinder centered around the vortex axis with a diameter of 0.01 m and a height of 0.008 m. We compute two separate cases with $Q_1 =$

2500 kW/m^3 and Q_2 = 3200 kW/m^3. In Fig. 6.1c, contour lines of axial velocity are overlaid on the center-slice map of axial velocity to indicate the relative location of the heat release region to the two reversed flow regions, which refer to the bubble and the onset of the double-helix mode downstream. There are two shear layers in the axial velocity profile at the current steady state of the baseline flow, an inner shear layer and an outer shear layer as shown in Fig. 6.1d. We set the heat release region within the inner shear layer for both calculations with Q_1 and Q_2.

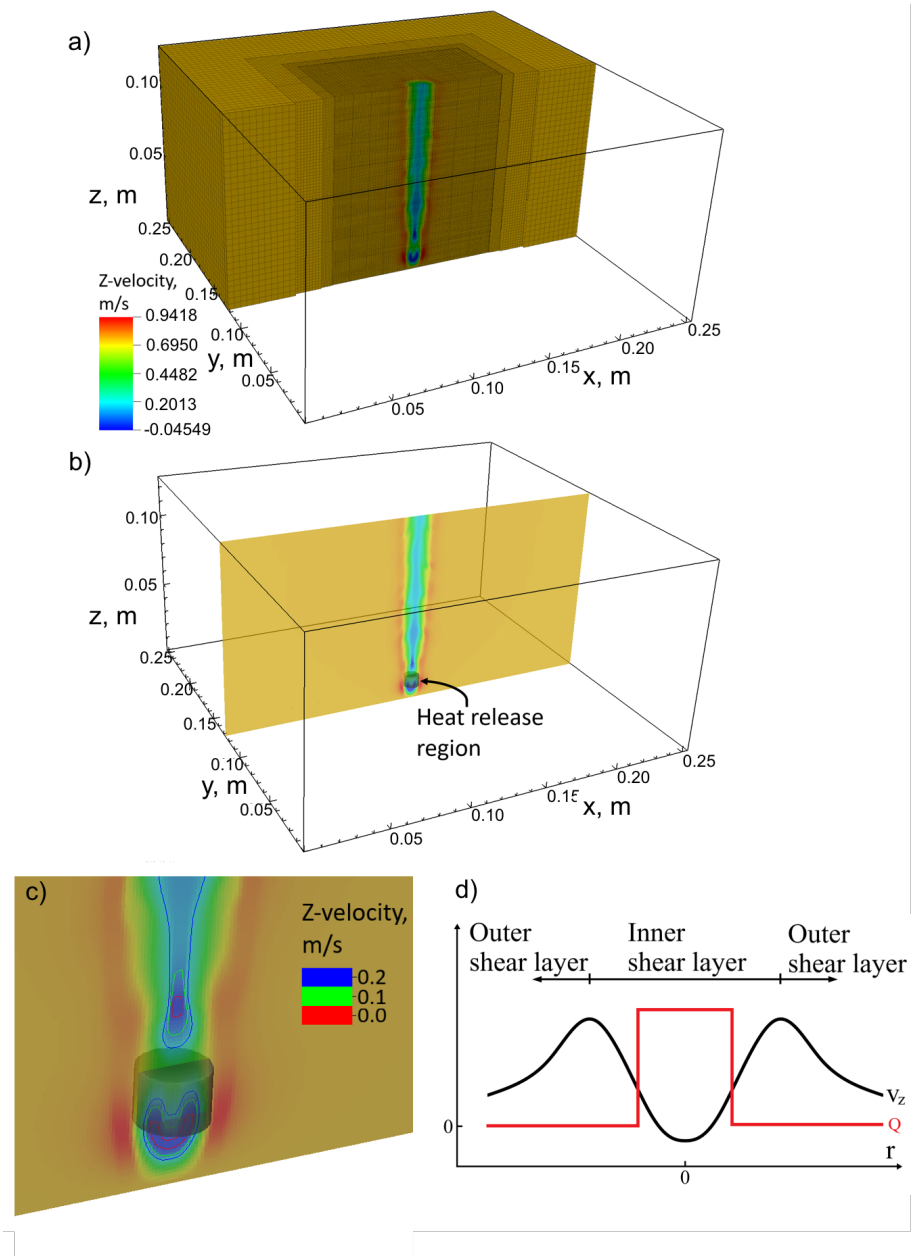

Figure 6.1: Computational setup for the cases with heat release effects. (A) Computational domain and mesh with superimposed axial velocity field. This mesh uses four levels of refinement. The axial velocity field here is the quasi-steady state of the baseline flow for heat release effects. (B) A center slice of the axial velocity field superimposed with the specified region with heat release. (C) A zoomed in view of the region with heat release. Contour lines of the axial velocity is superimposed to indicate the reversed flow region. (D) A schematic of the relative location of the region with heat release to the inner and outer shear layers in the axial velocity. The heat release is introduced within the inner shear layer.

For the calculations with heat extraction, we initialize the flow with air properties at 1200 K and 1 atm. These air properties are the thermal conductivity $K = 7.640 \times 10^{-5}$ kW/m K, specific heat ratio $\gamma = 1.323$, molecular weight $M_w = 28.97$ kg/kmol, and Prandtl number $Pr = 0.711$. We first calculate a baseline flow with $Re = 100$, $S = 1.3$ and, $\alpha = 1$. Here we set the radius of the vortex core $R = 0.02$ m so that the resultant $v_{z,\infty}$ from the definition of Re is neither too fast or too slow, as described above. A 0.8 m $\times$ 0.8 m $\times$ 0.4 m computational domain in employed as shown in Fig. 6.2a. The mesh is Cartesian with four levels of refinement as shown in Fig. 6.2a. The cell width is halved for each level. The finest cell size is $\Delta x = 0.8/512 = 1.5625 \times 10^{-3}$ m. The refinement does not change during the calculation.

First the baseline flow is allowed to reach a quasi-steady state, where it develops a bubble mode upstream and a laminar, columnar vortex downstream, as shown in the axial velocity field in Fig. 6.2b (detailed flow structure is described in the following section). Then, heat is extracted from a specified volume in the developed flow with the developed modes. An enlarged view of the region with heat extraction is shown in Fig. 6.2c. The heat extraction region is a cylinder centered around the vortex axis with a diameter of 0.036 m and a height of 0.022 m. We simulate the effects of two different heat-addition rates $Q_3 = -475$ kW/m^3 and $Q_4 = -1187.5$ kW/m^3. In Fig. 6.2c, the axial velocity contour lines are superimposed to indicate the relative location of the heat extraction region to the reversed flow region, which refers to the bubble mode. We set the heat extraction region within the inner shear layer for both calculations with Q_3 and Q_4, as indicated in

the schematic in Fig. 6.2d.

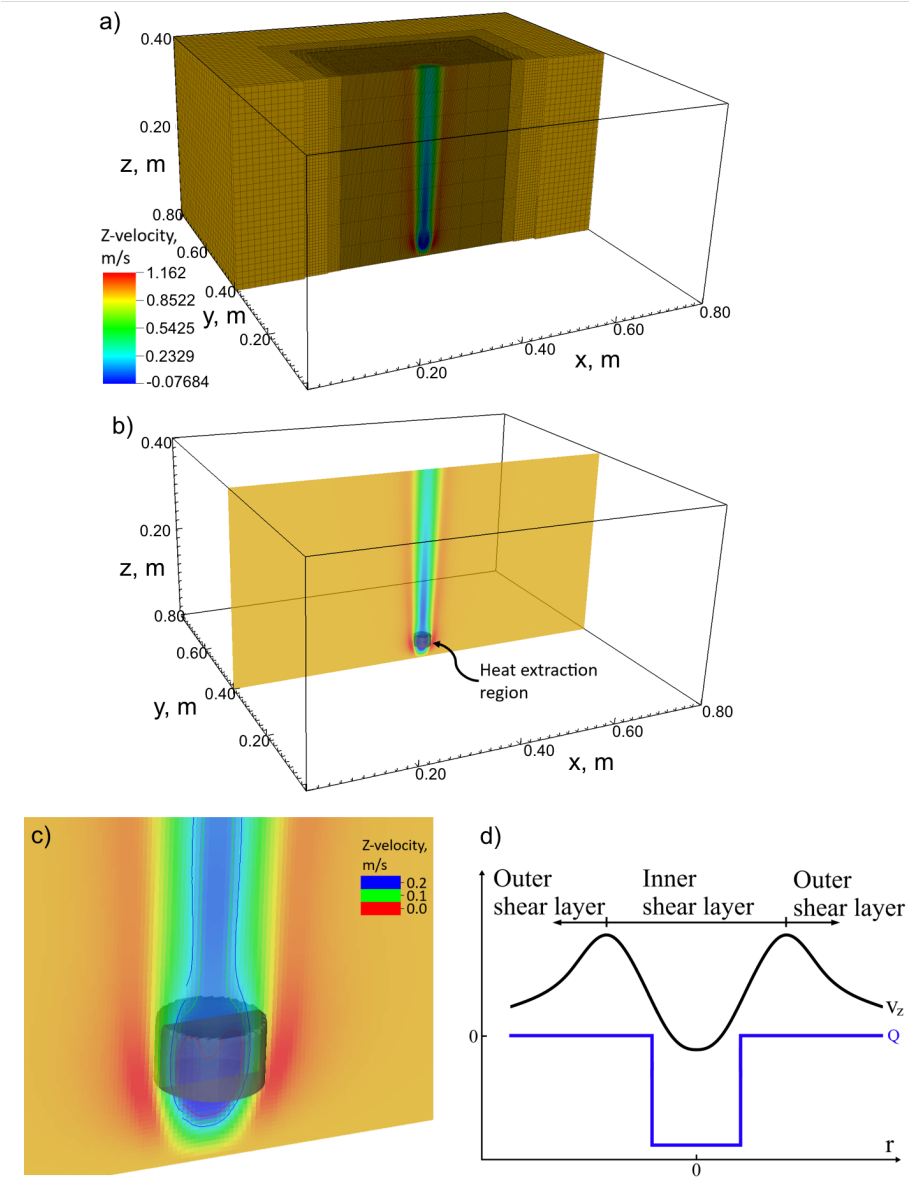

Figure 6.2: Computational setup for the cases with heat extraction effects. (A) Computational domain and mesh with superimposed axial velocity field. This mesh uses four levels of refinement. The axial velocity field here is the quasi-steady state of the baseline flow for heat extraction effects. (B) A center slice of the axial velocity field superimposed with the specified region with heat extraction. (C) A zoomed in view of the region with heat extraction. Contour lines of the axial velocity is superimposed to indicate the reversed flow region. (D) A schematic of the relative location of the region with heat extraction to the inner and outer shear layers in the axial velocity. The heat extraction is introduced within the inner shear layer.

6.4 Results

6.4.1 Heat Addition Effects

6.4.1.1 Baseline Flow

Figure 6.3 shows a time series of the baseline flow for the heat-addition cases. In a manner similar to the vortex breakdown calculation in Chapter 5, the flow particle paths are visualized through streaklines by releasing massless particles at the inflow boundary. The streaklines are superimposed on temperature contours. In Fig. 6.3, the temperature contour is uniformly black, which indicates a constant temperature of 300 K. In Fig. 6.3, only a central section of the computational domain is shown and the flow is from left to right.

As shown in Fig. 6.3a, the flow decelerates in the axial direction at around 0.2 s. This deceleration eventually leads to the formation of the bubble mode upstream, as shown in Fig. 6.3b. At a later time, a secondary instability develops downstream, resulting in a spiral mode initially. The spiral mode eventually transitions into a double-helix mode and maintains its structure as the flow reaches a quasi-steady state, as shown in Fig. 6.3d and e.

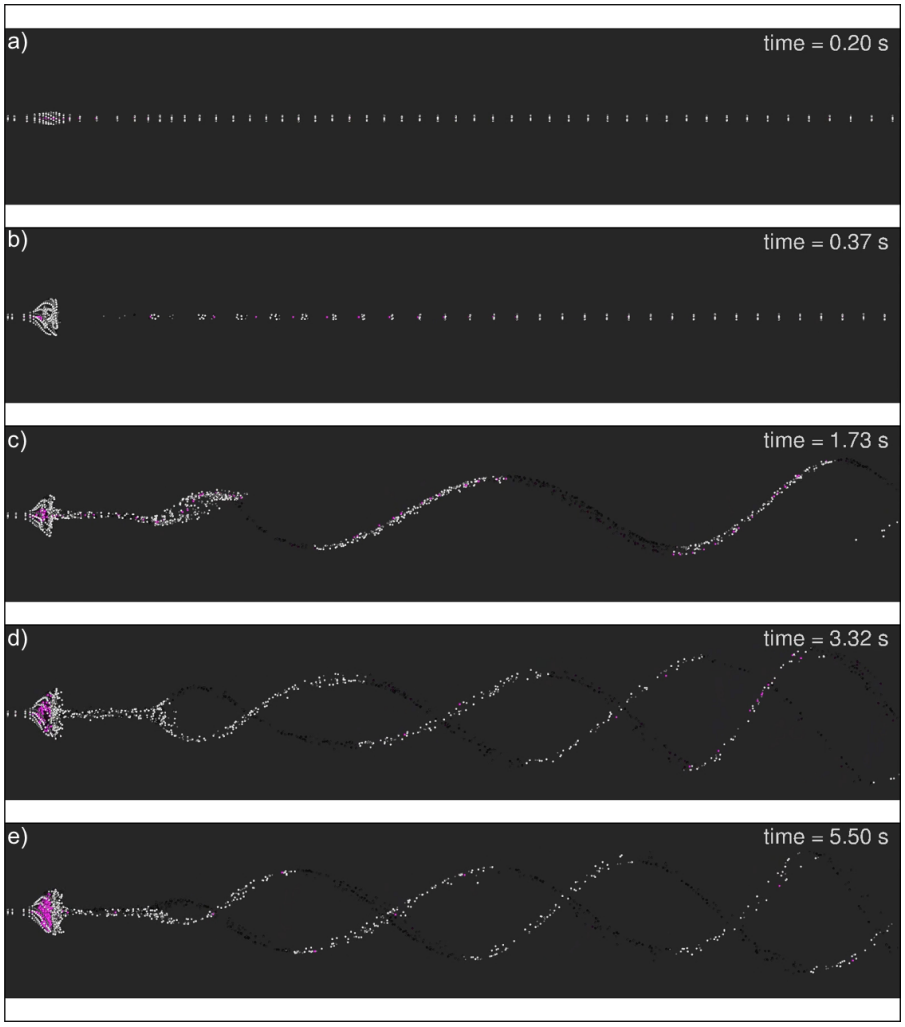

Figure 6.3: Streaklines overlaid on maps of temperature for the baseline flow for the cases with heat release effects. The temperature contour is uniformly black, which indicates a constant temperature of 300 K.

6.4.1.2 Heat Addition, $Q_1 = 2500$ kW/m^{3}case

Heat addition with a value of Q_1 is introduced into the quasi-steady baseline flow shown in Fig. 6.3e at time $t = 5.50$ s. The heat addition is held constant once it starts. Figure 6.4 shows a time series for the flow development from $t = 5.50$ s. Figures 6.4a and b show the initial transient state and the flow eventually reaches

a new quasi-steady state in Figs. 6.4c-f. The temperature contour in figure 6.4 shows that the temperature peaks near the downstream end of the bubble around the region where heat addition is introduced with a maximum temperature around 500 K.

As the flow develops, the bubble upstream at later time instances, seen in Figs. 6.4b-f, becomes larger in size than before heat addition, seen in Fig. 6.4a. This is because the negative axial velocity increases inside the bubble and therefore the reversed flow region inside the bubble becomes larger. The location of the bubble, however, is not affected by the heat addition.

In Figs. 6.4c-f, at the quasi-steady, the bifurcation point of the downstream double-helix moves further downstream compared with Figs. 6.4a and b. Notice that the bifurcation location oscillates in the axial direction. This is illustrated by the dashed line in Figs. 6.4c-f. The oscillation period is about 1.3 s. The span of double-helix structure in the radial direction at the new quasi-steady state becomes narrower, as shown in Figs. 6.4c-f.

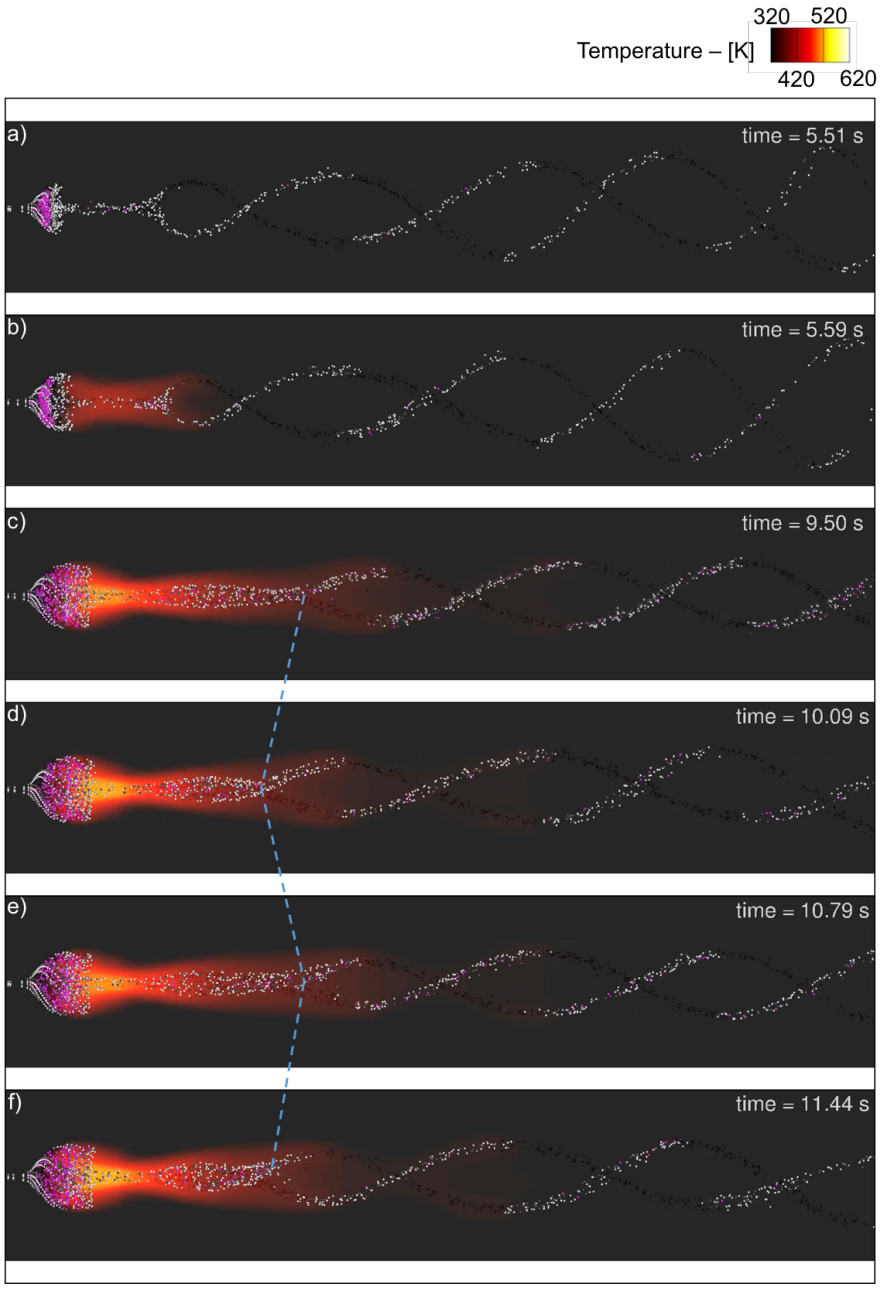

Figure 6.4: Streaklines overlaid on maps of temperature for the case with heat release rate $Q_1 = 2500$ kW/m^3. The dark region indicates lower temperature and the lighter regions indicates higher temperature.

6.4.1.3 Heat Addition, $Q_2 = 3200$ kW/m^3 case

Heat addition with a value of Q_2 is introduced into the quasi-steady baseline flow shown in Fig. 6.3e at time $t = 5.50$ s. Time series of the flow development after heat release is shown in Fig. 6.5. Figures 6.5a-b show the initial transient state and that the flow eventually reaches a new quasi-steady state in Figs. 6.5c-g. Similar to the case with Q_1, the temperature peaks near the downstream end of the bubble around the region where heat addition is applied, except with a higher maximum temperature around 630 K. The bubble upstream also increases in size as the flow develops (Figs. 6.5b-g) compared with the original form (Fig. 6.5a). The location of the bubble is not affected by the heat addition.

Different from the case with Q_1, the downstream double-helix structure initially becomes narrower in the radial direction, as shown Fig. 6.5b, and eventually merges into a columnar vortex after the flow reaches the quasi-steady state shown in Figs. 6.5c-g. Notice that there is a helical structure in the downstream columnar vortex. This helical structure disappears and reappears at the quasi-steady state. The appearance of the helical structure is shown in Figs. 6.5c, e, and g. The disappearance is shown in Figs. 6.5d and f.

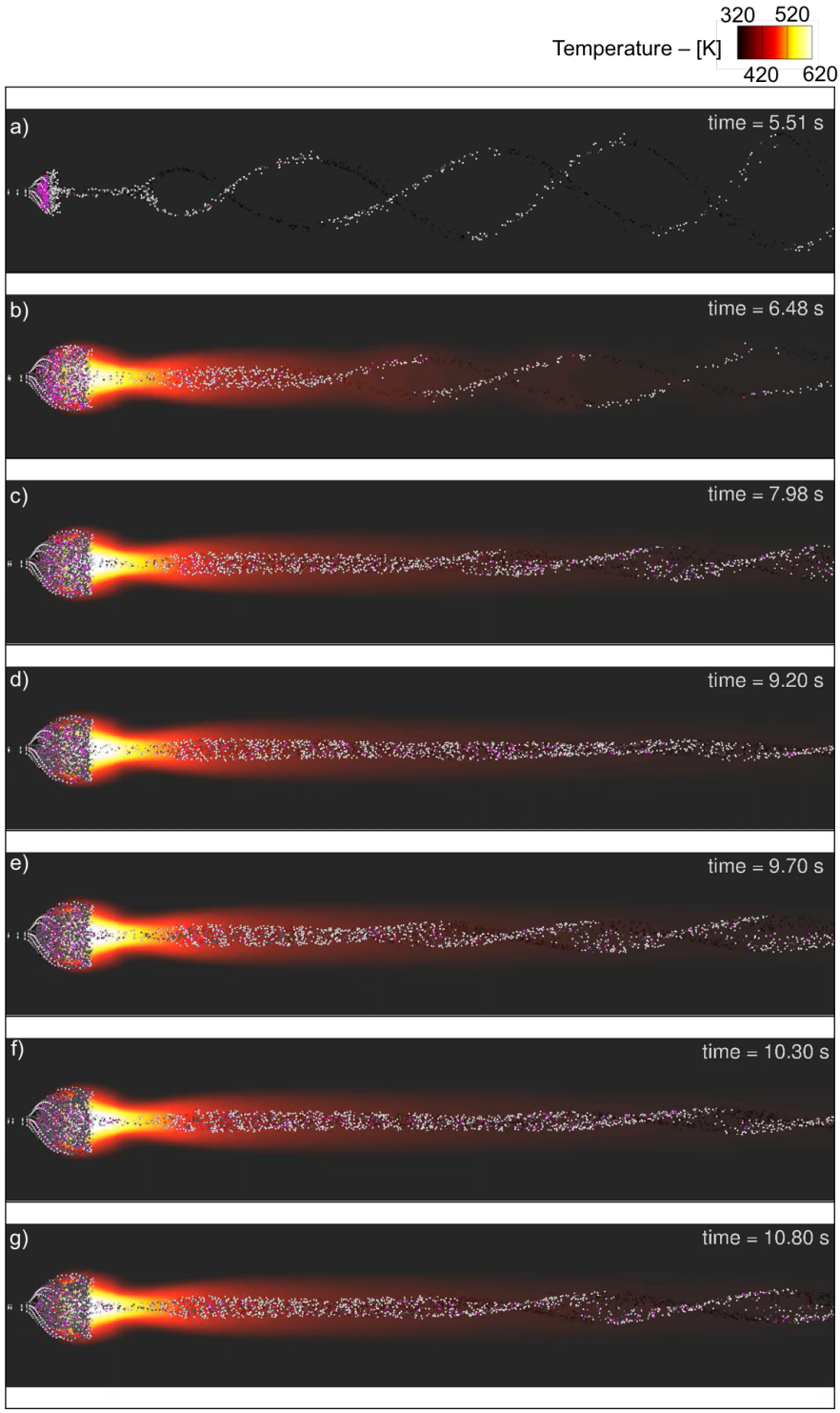

Figure 6.5: Streaklines overlaid on maps of temperature for the case with heat release rate $Q_2 = 3200$ kW/m^3. The dark region indicates lower temperature and the lighter regions indicates higher temperature.

6.4.2 Heat Extraction Effects

6.4.2.1 Baseline Flow

Figure 6.3 shows a time series of the baseline flow for the heat extraction cases. The streaklines are superimposed on temperature contours. In Fig. 6.6, the temperature contour is uniformly black, indicating a constant temperature of 1200 K in the flow field. In Fig. 6.3, only a central section of the computational domain is shown and the flow is from left to right.

As shown in Fig. 6.6a, the flow decelerates in the axial direction at around 0.27 s and forms the bubble mode upstream as shown in Fig. 6.3b. At a later time in Fig. 6.3c, the downstream flow starts to recover the columnar vortex structure. At the quasi-steady state, the flow develops a bubble mode upstream and a columnar vortex downstream, as shown in Fig. 6.3d.

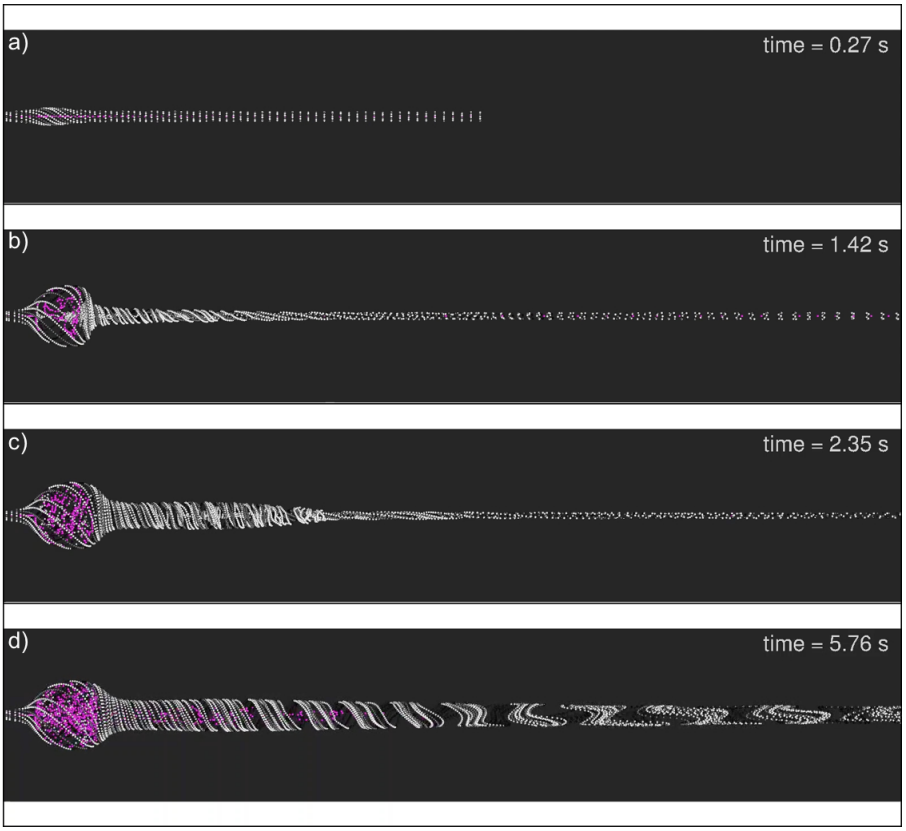

Figure 6.6: Streaklines overlaid on maps of temperature for the baseline flow for the cases with heat extraction effects. The temperature contour is uniformly black, which indicates a constant temperature of $1200K$.

6.4.2.2 Heat Extraction, $Q_3 = -475$ kW/m^3 case

Heat extraction with a value of Q_3 is introduced into the quasi-steady baseline flow shown in Fig. 6.6d at time $t = 5.76$ s. Time series of the flow development after heat extraction is shown in Fig. 6.7. Figures 6.7a-e show the initial transient state and that the flow eventually reaches a new quasi-steady state as shown in Figs. 6.7f and g. The temperature contour in Fig. 6.7 shows that the minimum temperature is near the downstream end of the bubble around the region where heat extraction is applied with a minimum temperature around 900 K.

Not long after the heat extraction is applied, the downstream columnar vortex develops a helical structure as shown in Fig. 6.7b. This disturbance leads to a precession of the vortex downstream at time 7.85 s as shown in Fig. 6.7c. The precession grows and develops into a spiral mode as shown in Fig. 6.7d. Later, at time 11.66 s as shown in Fig. 6.7e, the spiral structure starts to split into two helical structure. The flow downstream then eventually settles into a double-helix mode as shown in Fig. 6.7f and g.

The bubble mode in Fig. 6.7d-g is smaller in size compared with that in Fig. 6.7a-c. This shows the opposite trend as observed in the heat addition cases, which is as expected. The decrease in the bubble size is because the negative axial velocity decreases and therefore the reversed flow region becomes smaller. The location of the bubble, however, is not affected by the heat extraction effects. In Fig. 6.7f and g, we notice that the bifurcation point of the double-helix impinges into the bubble, merging with it from the bubble's downstream end. This is different from the double-helix mode observed in previous cases (for example in Fig. 6.3).

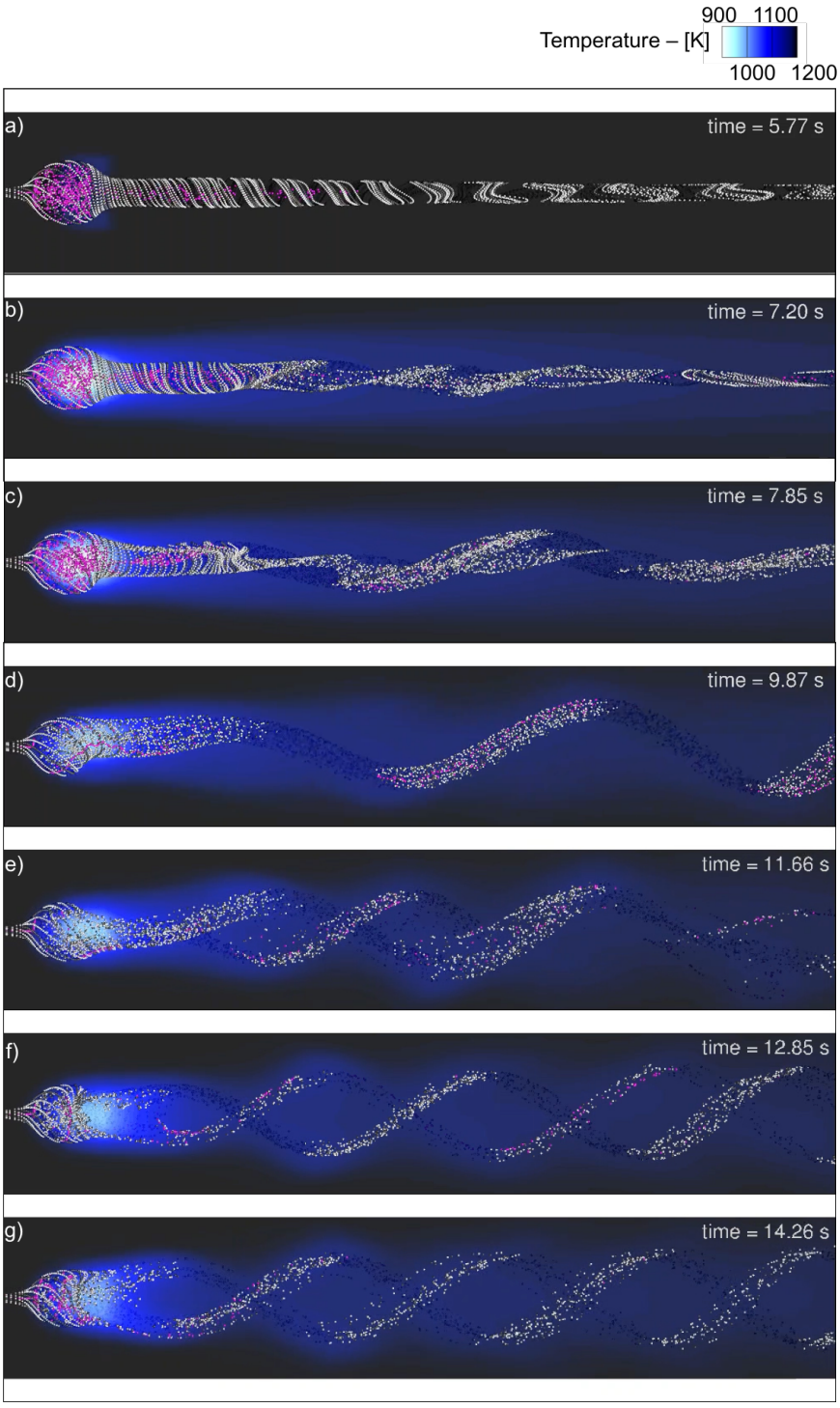

Figure 6.7: Streaklines overlaid on maps of temperature for the case with heat extraction rate $Q_3 = -475$ kW/m^3. The dark region indicates higher temperature and the lighter regions indicates lower temperature.

6.4.2.3 Heat Extraction, $Q_4 = -1187.5$ kW/m^3 case

The heat extraction with a value of Q_4 is applied to the quasi-steady baseline flow shown in Fig. 6.6d at time $t = 5.76$ s. A time series of the flow development after heat extraction is shown in Fig. 6.8. Figures 6.8a-d show the initial transient state and the flow eventually reaches a new quasi-steady state as shown in Figs. 6.7e and f. The temperature contour in Fig. 6.7 shows that the minimum temperature is near the downstream end of the bubble around the region where heat extraction is applied with a minimum temperature around 370 K.

After heat extraction is applied, the downstream columnar vortex develops a helical structure as shown in Fig. 6.8b. Different from the case with Q_3, the downstream flow bypasses the spiral mode and this helical structure develops directly into a double-helix structure as shown in Fig. 6.8c and d. Eventually, the flow reaches a quasi-steady state with a bubble mode upstream and a double-helix mode downstream.

Similar to the case with Q_3, the bubble mode in Fig. 6.8d-f is smaller in size compared with that in Fig. 6.8a-c. The location of the bubble, however, is not affected by the heat extraction. The bifurcation point of the double-helix also impinges onto the bubble and merges with it from its rear end.

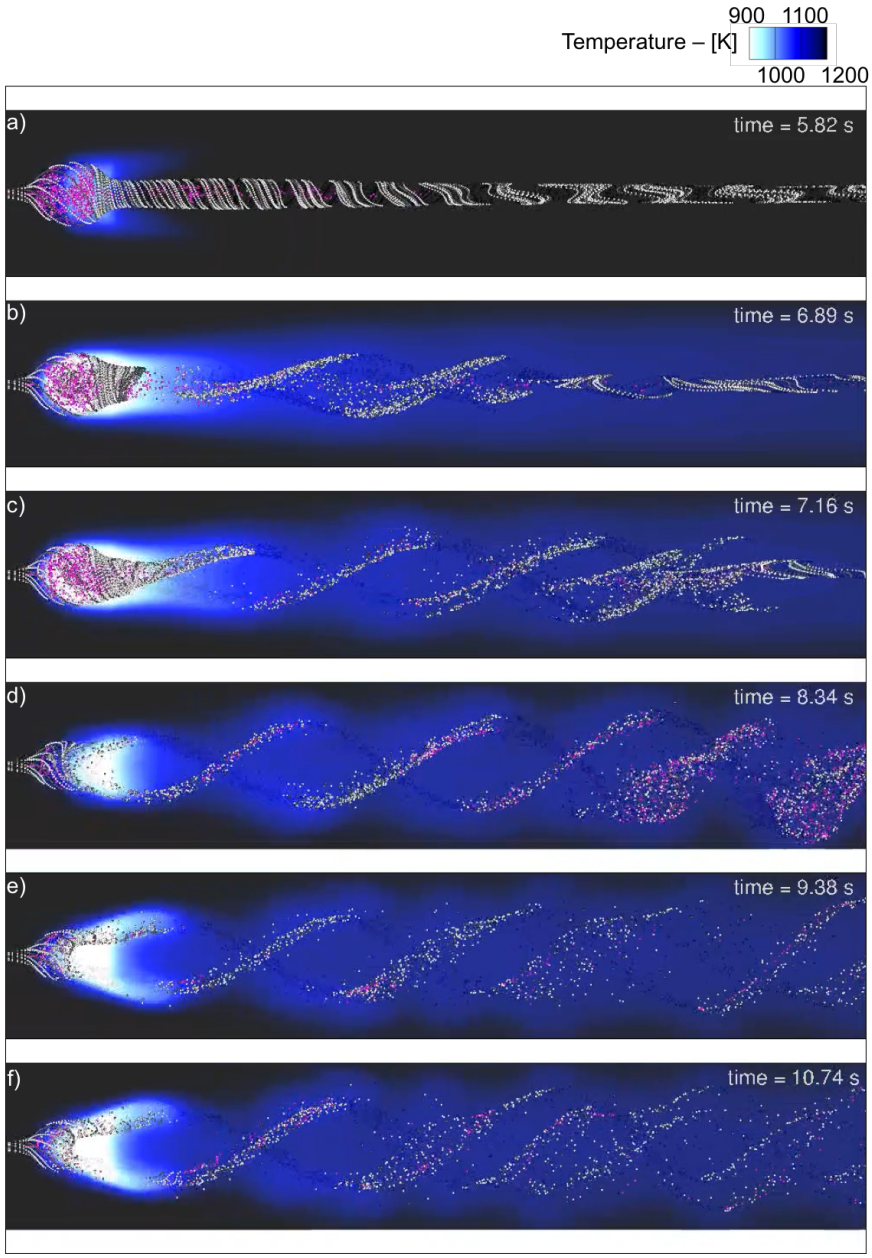

Figure 6.8: Streaklines overlaid on maps of temperature for the case with heat extraction rate $Q_4 = -1187.5$ kW/m^3. The dark region indicates higher temperature and the lighter regions indicates lower temperature.

6.5 Discussion

6.5.1 Mesh Resolution Study

We investigate the impact of the cell size on the solution by comparing the calculations of the heat extraction case with Q_4 using two different mesh resolutions: one with four levels of refinement, which is the mesh used for all calculations in the prior section, and the other with five levels. Both resolutions have the same course mesh and refine around the same region. We choose the case with the largest amount of heat extraction for the mesh resolution study because it is more unsteady and less laminar than the Q_1, Q_2, and Q_3 cases meaning the Q_4 case is most likely to benefit from the finer resolution.

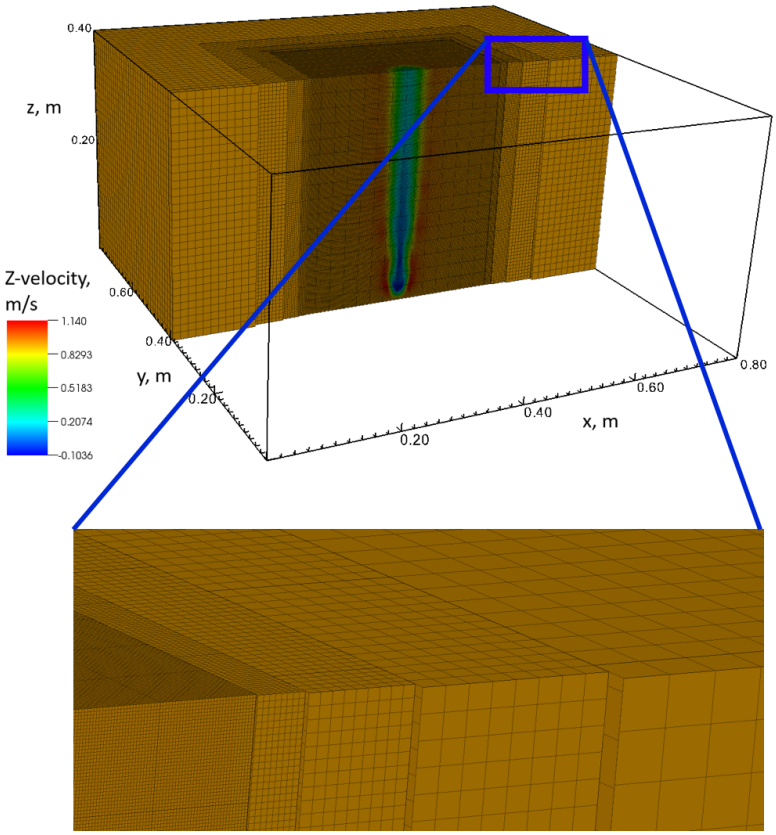

Figure 6.9: Computational domain and a finer mesh with superimposed initial velocity field. This mesh uses five levels of refinement. A zoomed in region in the upper portion of the mesh illustrates the mesh refinement.

Time history of the tangential and radial velocities is extracted at a point with a radial location $r = 0.02$ m and an axial location $z = 0.08$ m for both the coarse and fine mesh calculations. This point of measurement is downstream of the bifurcation point of the double-helix and within the double-helix structure in the radial direction. The extracted time history starts at 9.64 s and ends at 20.9 s for the coarse mesh case and ends at 12.9 s for the fine mesh case. The time history is extracted after the flow downstream develops the double-helix mode (as shown in Fig. 6.8e) and reaches a quasi-steady state. A fast Fourier transform is applied to

the time history and the frequency spectra of the tangential and radial velocities are shown in Fig. 6.10. Both the fine mesh and coarse mesh show dominant fluctuations at the same distinct frequencies for both the tangential and radial velocities. For example, in the frequency spectrum of the tangential velocity fluctuation, the distinct frequencies are at 8 Hz, 13 Hz, 22 Hz, and higher. This shows that the coarse mesh with four levels of refinement is able to predict the same dominant frequencies with similar magnitude as the fine mesh. Even though the coarse mesh predicts slightly lower or higher magnitude at some frequencies, the coarse mesh with four levels of refinement is sufficient to predict the major flow structure and the mode transitions of vortex breakdown that are of interest here.

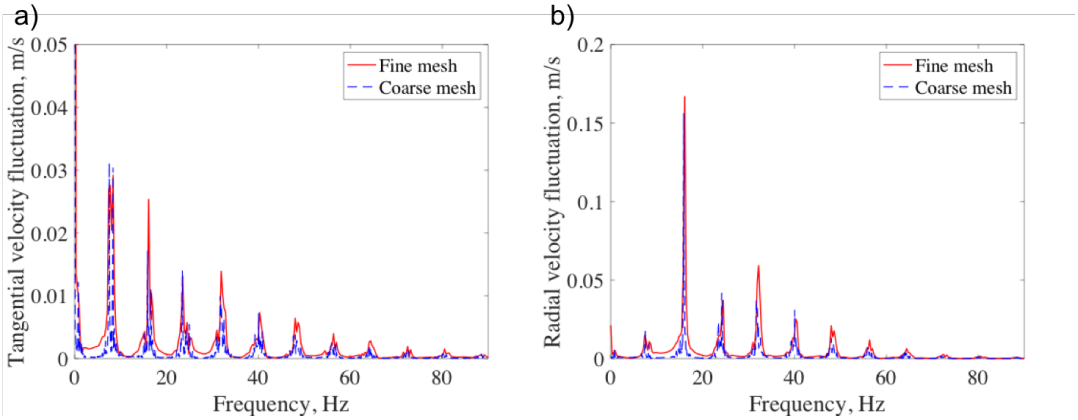

Figure 6.10: The frequency spectra for the velocity oscillations measured in the heat extraction case with $Q_4 = -1187.5$ kW/m^3 using both the baseline mesh and the finer mesh. (A) Frequency spectra of the tangential velocity. (B) Frequency spectra of the radial velocity. The time history of both tangential and radial velocity are measured at a point with a radial location $r = 0.02$ m and an axial location $z = 0.08$ m. The point of measurement is downstream of the bifurcation point of the double-helix and within the double-helix structure in the radial direction.

6.5.2 Effect of Viscosity and its Temperature Dependence

As shown in the results in Section 6.4, heat addition causes the double-helix mode to transition to a columnar vortex and heat extraction causes the columnar vortex to transition into a spiral or transition into a spiral followed by a double-helix mode. How heat inputs actually affect the mode transition of vortex breakdown, however, is not clear, and we look to further isolate the cause. Applying heat addition or heat extraction in the flow field causes the temperature to vary and therefore varies both the flow viscosity and density. When heat addition is applied, the flow temperature increases, increasing the local viscosity and decreasing the local density. Similarly, when heat extraction is applied, the flow temperature decreases locally, decreasing the local viscosity and increasing the local density.

The changes in viscosity, and thus changes in effective Re, can change which modes of vortex breakdown the flow develops, as shown in prior work [27]. For a vortex with a bubble mode of breakdown and a fixed circulation level, the flow downstream of the bubble will have a columnar vortex at a lower Re, a spiral mode of breakdown at a higher Re, and a double-helix mode of breakdown at an even higher Re. Therefore the changes in effective Re could be one potential explanation of the mode changes observed in the cases with heat addition and extraction effects.

The density gradients also can affect the dynamics of vortex breakdown. A prior analytical study [122] shows that a density decrease within the inner shear layer of the axial velocity can suppress the PVC, which is associated with the spiral mode. Therefore, the density gradients within the inner shear layer of the axial

velocity could also be a potential cause of the mode changes observed in the cases with heat release and extraction effects.

In order to isolate the effects of change in viscosity and density gradients on the cause of mode transition that is observed in the calculations with heat release and extraction, we perform the four cases with heat addition rates Q_1 and Q_2 and heat extraction rates Q_3 and Q_4 again, except now with a constant viscosity that is not dependent on temperature. This means all of the parameters and computational setup are the same as the cases in Section 6.4, except the temperature dependence in viscosity is turned off, that is the exponent 0.7 in Eq. 6.5 is set equal to zero. Therefore, the results should rule out the effect of change in viscosity and only have the effect of density gradients. We describe the results in the following section and compare them with the calculations in Section 6.4.

6.5.2.1 $Q_1 = 2500$ kW/m^{3}case with a constant viscosity

Similar to the case in Section 6.4.1.2, heat release with Q_1 is introduced into the quasi-steady baseline flow shown in Fig. 6.3e at time $t = 5.50$ s. The heat release is held constant through out the flow development. What is different from the case in Section 6.4.1.2 is that the the viscosity is forced to be constant and maintain its initial value, meaning the viscosity does not vary as a function of the local temperature. This means that the viscosity here is smaller than the viscosity in the case in Section 6.4.1.2.

Figure 6.11 shows the time series for the flow development after $t = 5.50$ s.

Figures 6.11a and b show the initial transient state and the flow eventually reaches a new quasi-steady state in Figs. 6.11c-f. Compared to the results in Section 6.4.1.2, the flow development is similar. The bubble upstream also becomes larger in size and the span of the double-helix structure is narrower after the flow reaches a quasi-steady state as shown in Figs. 6.11c-f. The bifurcation point of the double helix also moves further downstream, but not as far downstream as the case in Section 6.4.1.2. The oscillation of the bifurcation point that appears in the result in Fig. 6.4, however, no longer exists here. The bifurcation point remains at a relatively constant axial location, as indicated by the dashed line in Figs. 6.11c-f.

Although there is minor difference in the flow structure in both calculations with temperature-dependent viscosity and constant viscosity, the comparison shows that the changes in viscosity due to its temperature dependence, that is the changes in the effective Re, is not the dominant factor here that causes the major changes in flow structure under heat release effects. This indicates that the density gradient caused by the temperature variation should be the main dominant factor.

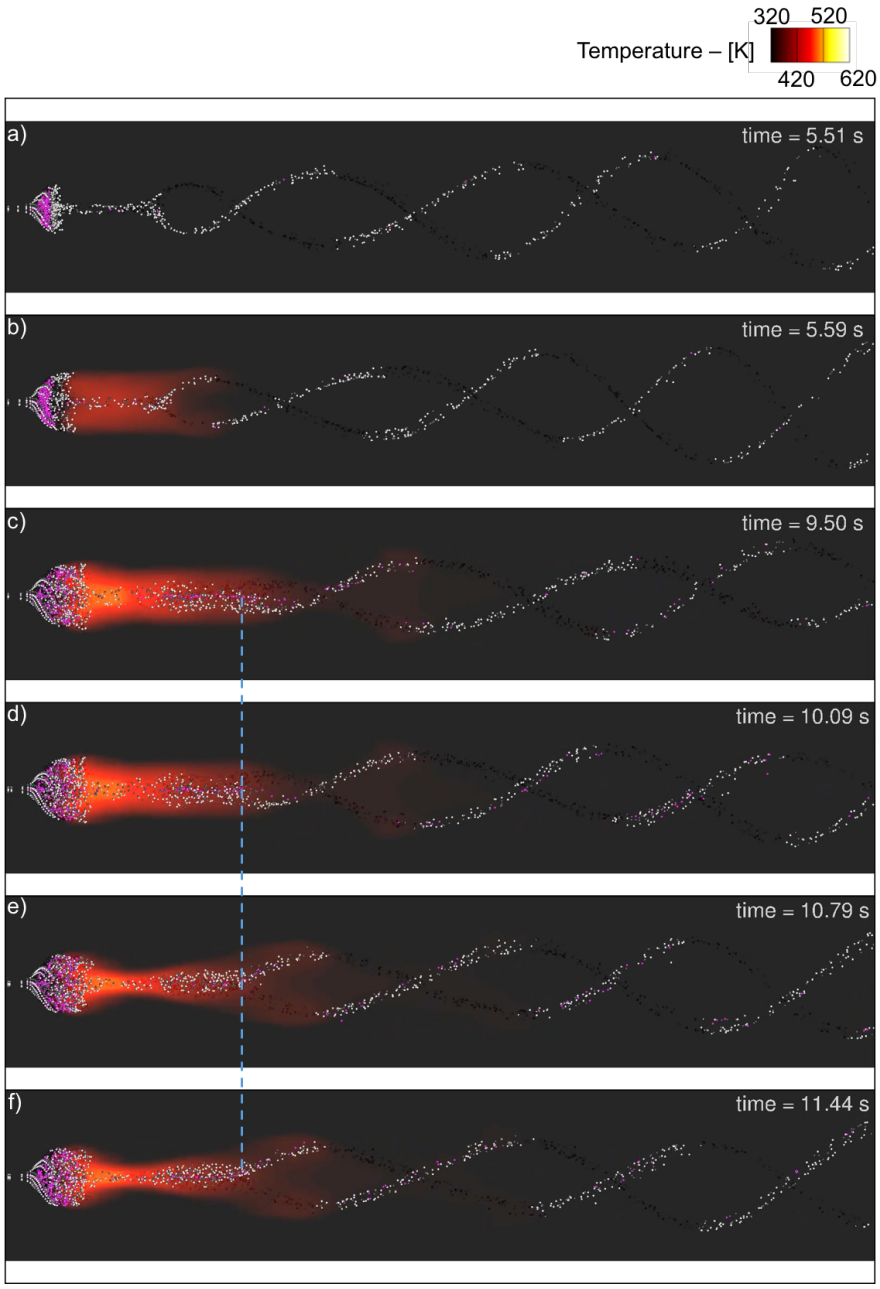

Figure 6.11: Streaklines imposed on contours of temperature for the case with heat release rate $Q_1 = 2500$ kW/m^3 and a constant viscosity (not a function of temperature). The dark region indicates lower temperature and the lighter regions indicates higher temperature.

A further comparison of the calculations with a temperature-dependent viscosity versus with a constant viscosity for heat addition Q_1 is then performed by

comparing the time history of the transient flow development. This is done by extracting line profiles of the axial velocity along the axial centerline for all of the computational time steps after heat addition is applied and presenting them as z-t diagrams, which are shown in Fig. 6.12. We discuss this figure from bottom to top as time develops and from left to right as from upstream to downstream.

Right before heat release is introduced at 5.50 s, there are two negative axial velocity regions in the baseline flow, which are indicated by the white dashed lines in both Figs. 6.12a and b. The reversed flow near the upstream inflow location corresponds to the bubble mode as indicated by the arrow with a 'B', and the reversed flow downstream corresponds to the bifurcation point of the double helix as indicated by the arrow with an 'H'. Shortly after the heat is applied to the flow, the downstream reversed flow region disappears in both cases as shown in Figs. 6.12a and b. This corresponds to the increase of the axial velocity at the bifurcation point of the double helix due to the heat release and as a result the bifurcation point moves further downstream.

In Fig. 6.12a, after heat release is introduced at 5.50 s, the region of reversed flow in the bubble upstream is relatively not affected by heat addition. This is shown by the white dashed line that covers the entire time period. The reversed flow in the bubble upstream in Fig. 6.12b, however, disappears shortly after the heat release. This indicates that the flow in the bubble mode has a larger negative axial velocity at the axial centerline for the case with varying viscosity than that for the case with constant viscosity.

In Fig. 6.12, we observe an oscillation with high frequencies in both cases

with varying viscosity and constant viscosity. This oscillation corresponds to the pulsating bubble and the rotation motion of the double-helix structure. The pulsating bubble refers to the bubble shrinking and growing in size at its downstream end periodically. An oscillation with a low frequency downstream, however, only appears in Fig. 6.12a. This oscillation corresponds to the oscillation of the bifurcation point of the double helix downstream and it only appears in the case with temperature-dependent viscosity. This is consistent with results in Figs. 6.4 and 6.11.

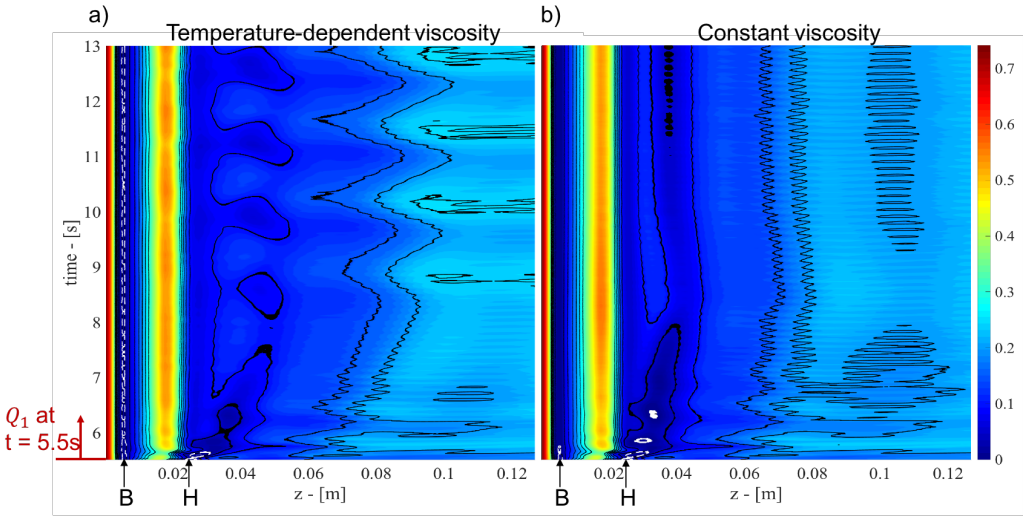

Figure 6.12: Time history of the axial velocity along the vortex axis ($r = 0$ m) for the calculations with heat release Q_1. (A) Calculation with a temperature-dependent viscosity.(B) Calculation with a constant viscosity that is not a function of temperature. The white dashed line marks the negative axial velocity region.

6.5.2.2 $Q_2 = 3200$ kW/m^{3}case with a constant viscosity

Similar to the case in Section 6.4.1.3, heat addition with Q_2 is applied to the quasi-steady baseline flow shown in Fig. 6.3e at time $t = 5.50$ s, except now, with

the temperature dependence of viscosity turned off.

Figure 6.13 shows the time series for the flow development after $t = 5.50$ s. Figures 6.13a-c show the initial transient state and the flow eventually reaches a new quasi-steady state in Figs. 6.11d-f. Compared to the results in Section 6.4.1.3, the flow development is similar. The bubble upstream also becomes larger in size and the downstream double helix eventually merges into a columnar vortex while retaining a helical structure after the flow reaches the quasi-steady state, as shown in Figs. 6.11d-f. A slight precession in the downstream columnar vortex, however, is observed here in Figs. 6.11d-f. This precession does not appear in the equivalent calculation with temperature-dependent viscosity.

Although there is some minor difference in the flow structure in both calculations with temperature-dependent viscosity and constant viscosity, the comparison shows that the changes in viscosity due to its temperature dependence, that is the changes in the effective Re, is not the dominant factor here that causes the mode transition of vortex breakdown under heat release effects. This indicates that the density decrease caused by the temperature increase should be the main dominant factor that suppresses the double-helix mode. This is consistent with the analytical study in [122], except they studied the spiral mode only and showed that a spiral mode is suppressed under density gradient effect.

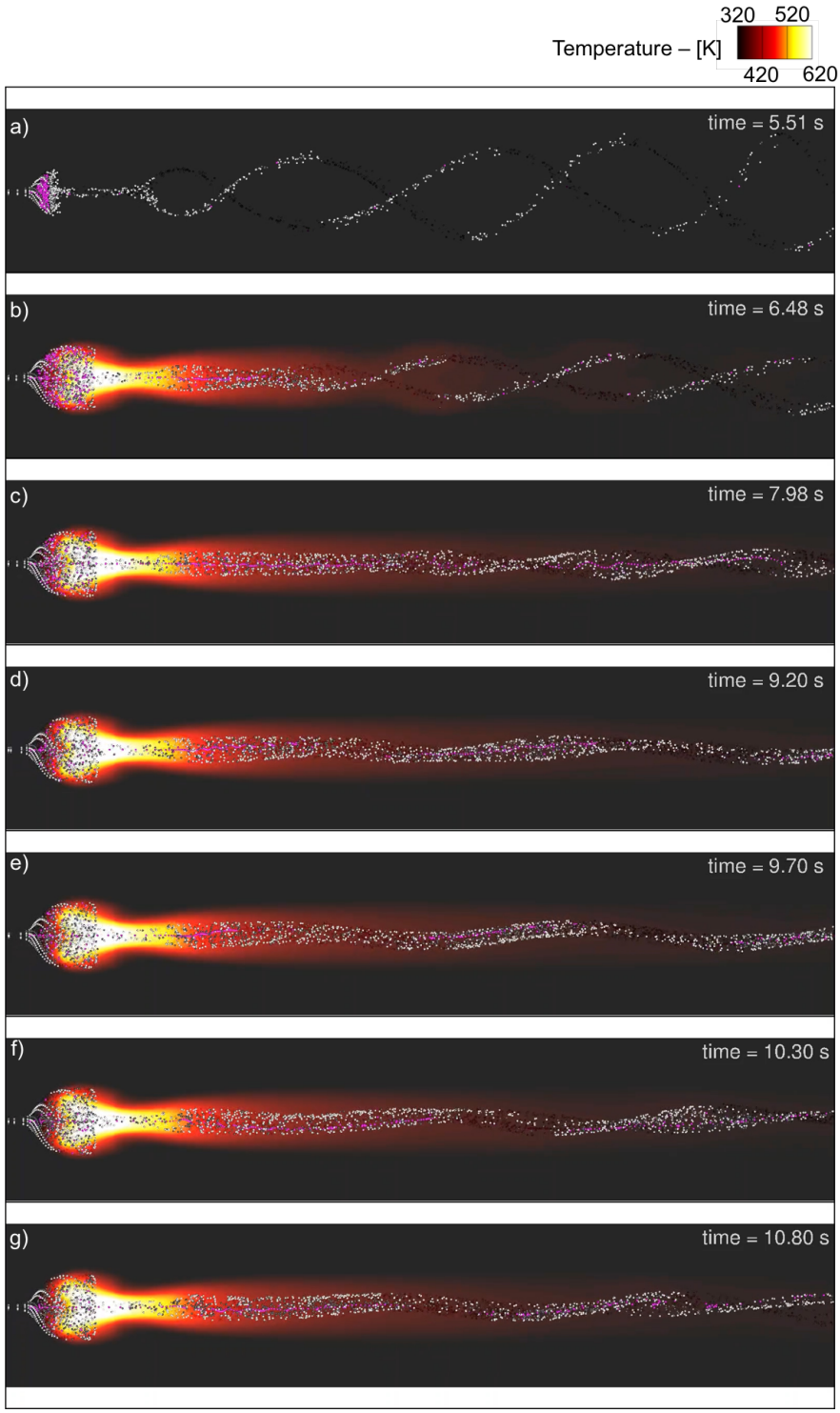

Figure 6.13: Streaklines imposed on contours of temperature for the case with heat release rate $Q_2 = 3200$ kW/m^3 and a constant viscosity. The dark region indicates lower temperature and the lighter regions indicates higher temperature.

6.5.2.3 $Q_3 = -475$ kW/m^{3}case with a constant viscosity

Similar to the case in Section 6.4.2.2, heat extraction with Q_3 is introduced into the quasi-steady baseline flow shown in Fig. 6.6d at time $t = 5.76$ s. In this calculation, the temperature dependence of viscosity is turned off.

Time series of the flow development after heat extraction is shown in Fig. 6.14. Figures 6.14a-e show the initial transient state and the flow eventually reaches a new quasi-steady state as shown in Figs. 6.7f and g. Compared to the results in Section 6.4.2.2, the flow development is similar. The bubble upstream also becomes smaller in size and the flow downstream initially develops a spiral mode, as shown in Figs. 6.7d and e, and eventually develops into a double helix as shown in Figs. 6.7f and g. A delay in time in mode transition is observed here compared with the calculation with temperature-dependent viscosity as shown in Fig. 6.7. In Fig. 6.7c, a precession downstream of the bubble already appears at time $t = 7.85$ s. Whereas here in Fig. 6.14c, there is no obvious sign of precession yet at time $t = 7.85$ s. This delay in time causes the double-helix mode to appear about 2.6 s later in the calculation with a constant viscosity than in the calculation with a temperature-dependent viscosity, which is shown in Fig. 6.7e and Fig. 6.14e.

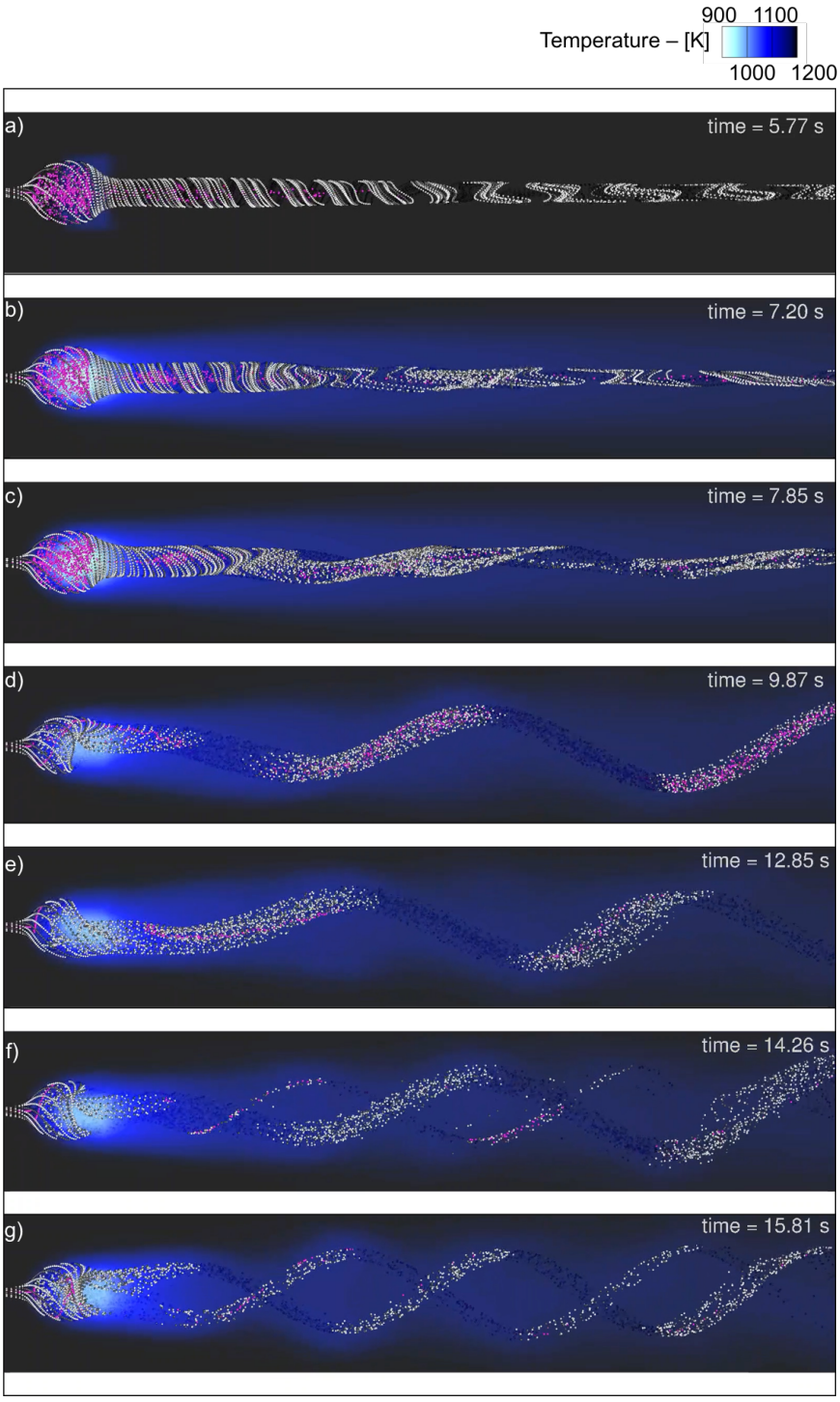

Figure 6.14: Streaklines imposed on contours of temperature for the case with heat extraction rate $Q_3 = -475$ kW/m^3 and a constant viscosity. The dark region indicates higher temperature and the lighter regions indicates lower temperature.

The time difference in mode transition between the calculations with temperature-dependent viscosity and constant viscosity can be seen more clearly in the development of the pressure field. We extracted line profiles of pressure along the axial centerline for all of the computational time steps after heat extraction is applied and present them as z-t diagrams, shown in Fig. 6.12. Shortly after heat extraction is applied, the disturbance from the heat extraction propagates downstream in both cases, as indicated by the white dashed lines in Fig. 6.12a and b. After this initial disturbance, the pressure field in both cases is relatively smooth until a second disturbance appears as indicated by the white dots in Fig. 6.12a and b. This disturbance corresponds to the occurrence of the precession downstream which propagates upstream and downstream as indicated by the arrows. This disturbance eventually leads to the development of the spiral mode, causing oscillations in the pressure field shown in Fig. 6.12. We can see clearly in Fig. 6.12 that the disturbance from the precessing motion appears about 0.2 s earlier in Fig. 6.12a than in Fig. 6.12b.

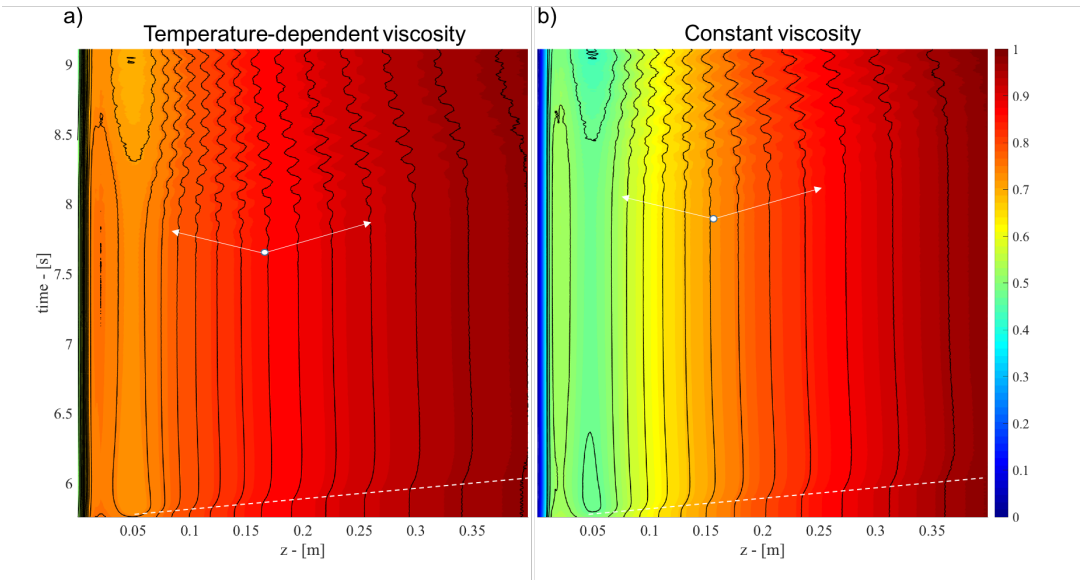

Figure 6.15: Time history of pressure along the vortex axis ($r = 0$ m) for the calculations with heat extraction Q_3. (A) Calculation with a temperature-dependent viscosity.(B) Calculation with a constant viscosity that is not a function of temperature. The dashed lines indicate the propagation of the initial disturbance caused by the introduction of heat extraction. The white dot indicates the appearance of a second disturbance downstream caused by the precession and the arrows indicate its propagation direction.

Although there is a time difference in mode transition between the calculations with temperature-dependent viscosity and constant viscosity, the comparison shows that the changes in viscosity due to its temperature dependence is not the dominant factor here that causes the mode transition of vortex breakdown undergoing heat extraction. This indicates that the density increase caused by the temperature decrease should be the dominant factor that transitions the columnar vortex to the spiral mode first and then eventually to the double-helix mode. The change in viscosity, however, can promote the mode transition since it causes the transition to occur at an earlier time.

6.5.2.4 $Q_4 = -1187.5$ kW/m^{3}case with a constant viscosity

Similar to the case in Section 6.4.2.3, heat extraction with Q_4 is applied into the quasi-steady baseline flow shown in Fig. 6.6d at time $t = 5.76$ s. In this calculation, the temperature dependence of viscosity is turned off

Time series of the flow development after heat extraction is shown in Fig. 6.16. Figures 6.16a-d show the initial transient state and that the flow eventually reaches a new quasi-steady state as shown in Figs. 6.16e and f. Compared to the results in Section 6.4.2.3, the flow structure is similar. The bubble upstream also becomes smaller in size and the flow downstream develops a double-helix mode directly as shown in Fig. 6.16b, bypassing the spiral mode. Compared with the calculation with temperature-dependent viscosity in Fig. 6.8, the temporal evolution of the flow structure is also similar, meaning the transition of the downstream columnar vortex to the double-helix mode occur at a similar time and the flow reaches the quasi-steady state around a similar time. This indicates that when the heat extraction rate is high, the change in viscosity due to heat extraction has a very minor effect on the mode transitions of vortex breakdown, in terms of both timing and the final modes. In fact, it is the density increase caused by the temperature decrease that has the dominant effect on the mode transitions.

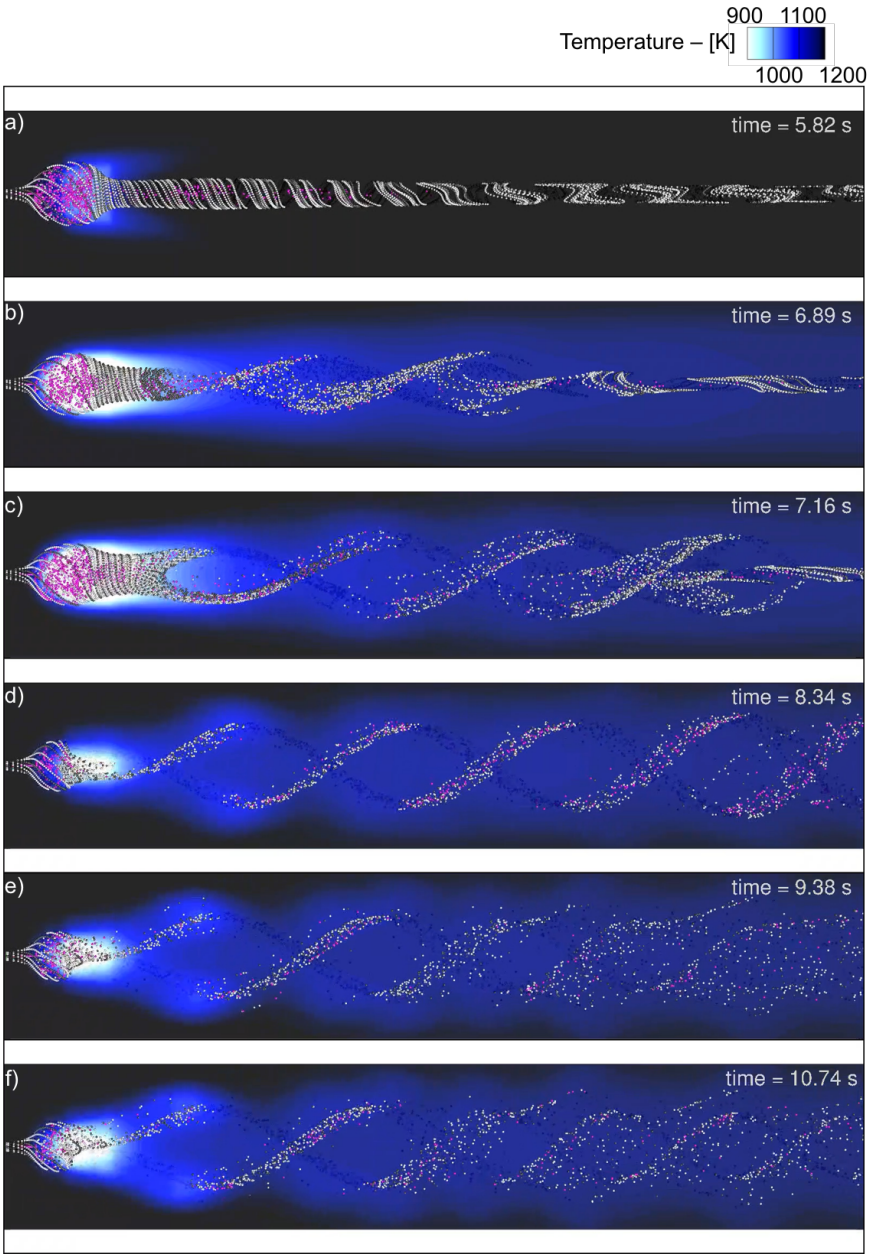

Figure 6.16: Streaklines imposed on contours of temperature for the case with heat extraction rate $Q_4 = -1187.5$ kW/m^3 and a constant viscosity. The dark region indicates higher temperature and the lighter regions indicates lower temperature.

6.6 Conclusions

Vortex breakdown subject to heat addition and heat extraction is studied in this work by solving the 3D, unsteady, compressible NS equations with an energy source term using the BICFCT algorithm. Four cases in total are studied with two heat addition rates $Q_1 = 2500$ kW/m^3 and $Q_2 = 3200$ kW/m^3 and two heat extraction rates $Q_3 = -475$ kW/m^3 and $Q_4 = -1187.5$ kW/m^3. Heat addition is introduced into a baseline flow with a bubble mode upstream and a double-helix mode downstream. The region of heat addition is a cylinder centered around the vortex axis starting from the downstream half of the bubble upstream and ending before the bifurcation point of the double helix downstream. Heat extraction is applied to a baseline flow with a bubble mode upstream and a columnar vortex downstream. The region of heat extraction is also a cylinder centered around the vortex axis starting from the downstream half of the bubble and ending before the columnar vortex downstream. Both heat release and extraction are introduced into regions within the inner shear layer of the axial velocity.

Results of the case with heat addition rate $Q_1 = 2500$ kW/m^3 show that the temperature peaks in the region of heat addition with a maximum temperature around 500 K. The bubble mode upstream becomes larger in size as a result of an increase of the negative axial velocity due to the heat addition. The location of the bubble is not affected by the heat addition downstream. The span of the downstream double-helix structure in the radial direction becomes smaller at the new quasi-steady state. The bifurcation point of the double helix moves further

downstream with a periodic oscillation in the axial direction.

Results of the case with heat addition rate $Q_2 = 3200$ kW/m^3 show that the temperature peaks in the region of heat addition with a maximum temperature around 630 K. The bubble mode upstream also becomes larger in size and the location of the bubble is relatively unaffected by the heat addition from downstream. Different from the case with Q_1, a higher heat addition rate Q_2 causes the downstream double helix to merge into a columnar vortex at the quasi-steady state. A helical structure appears and disappears periodically in the columnar vortex downstream.

In the case with heat extraction rate $Q_3 = -475$ kW/m^3, the temperature decreases around the region of heat extraction with a minimum temperature of 900 K near the rear end of the bubble. The bubble becomes smaller in size as a result of a decrease of the negative axial velocity due to the heat extraction effects. The location of the bubble is unaffected by the heat extraction. The downstream columnar vortex initially develops a precessing motion which leads to the development of a spiral mode. The spiral mode eventually transitions into a double-helix mode at the quasi-steady state. The bifurcation point of the double helix impinges onto the bubble and merges with the bubble from its downstream end.

In the case with a higher heat extraction rate $Q_4 = -1187.5$ kW/m^3, the minimum temperature is around 370 K. Similar to the case with Q_3, the bubble mode becomes smaller in size and the location of the bubble remains unaffected by heat extraction. The downstream columnar vortex, however, transitions directly into a double-helix mode by skipping the spiral mode.

A further investigation is performed to isolate the cause of mode transitions of vortex breakdown subject to heat addition and extraction. The changes in viscosity due to its temperature dependence and the density gradient created by the temperature variation are the two factors considered that have potential influence on the mode transition. To isolate these two effects, four cases with heat addition rates Q_1 and Q_2 and heat extraction rates Q_3 and Q_4 are computed again, except with viscosity forced to be constant and maintain its initial value. We then compare these results with only the density gradient effect against the previous calculations.

The comparisons show that the density gradient is the dominant effect causing the mode transitions of vortex breakdown subject to heat addition and extraction. Density decrease (due to heat addition) within the inner shear layer suppresses the double-helix mode. This is consistent with prior analytical analysis describing the density gradient effects on vortex breakdown [122], except this analysis only investigated a spiral mode and found the spiral mode to be suppressed by a density decrease. In this study, we are first to show that a density increase (due to heat extraction) enhances vortex breakdown. A smaller density increase causes a columnar vortex to transition to a spiral mode initially and eventually into a double helix. A higher density increase causes a columnar vortex to transition directly into a double helix.

Changes in viscosity, that is the effective Re, is not the dominant effect causing the mode transitions of vortex breakdown subject to heat addition and extraction. This is consistent with the wave theory that attempts to explain the breakdown mechanism, that the breakdown dynamics are essentially inviscid. The viscosity

change, however, can promote the transition when heat addition and extraction rates are relatively small. This is shown in the case with Q_1 that the viscosity increase due to temperature increase suppresses the double helix more by pushing it further downstream. In the case with Q_3, the viscosity decrease due to temperature decrease causes a faster transition from a columnar vortex to a spiral mode and a spiral mode to a double helix. When the heat addition and extraction rates are high, for example in cases with Q_2 and Q_4, changes in viscosity have minor influence on the temporal development of the flow structures.

This fundamental study of the heat addition and extraction effects on the dynamics and transition of modes of vortex breakdown can serve as a base for understanding the dynamics of PVC and thereby understand how to control the oscillatory modes in swirl combustors. This study suggests that mode transition could occur under certain heat addition conditions and the oscillatory amplitude and frequency can therefore be affected. This study also suggests that heat addition and extraction could be a potential way of controlling vortex breakdown in aeronautical applications. This study can also help understand the transition from a fire whirl to a blue whirl. During the dynamic transitional stage, the initial fire whirl decreases in size and wanders in location. This causes changes in density gradient and therefore could promote the mode transition of vortex breakdown. This potentially could be one of the mechanisms that leads to the formation of the blue whirl.

Chapter 7: Summary

7.1 New Solution Procedure for Flux-Correct Transport and Barely Implicit Correction Algorithms for 3D Flows

This thesis has presented a new BIC algorithm for the computation of 3D, low-Mach-number flows with physical diffusion processes. The algorithm uses FCT to explicitly integrate the convective processes and solves one elliptic equation to remove the acoustic limit on the integration time step. This work modified the solution procedures of FCT and BIC to stabilize these algorithms for 3D computations. First, we found that the low-order solution of the original FCT algorithm is numerically unstable in 3D due to excessive numerical diffusion. FCT was stabilized in 3D by reducing the amount of numerical diffusion in the low-order solution while still maintaining the accuracy of the original FCT algorithm. Then, the solution procedure for the BIC algorithm was modified and outlined to include physical diffusion processes. A new filter was introduced that removes any numerical oscillations that may arise in the solution due to the pressure correction in the BIC integration procedure.

The accuracy and robustness of this new BIC algorithm was examined through

four test problems. First, a sinusoidal density profile was convected in 1D and the solution was compared against an exact solution to assess BIC's spatial and temporal accuracy. The error analysis showed that BIC is second-order convergent in space and it is not convergent in time. The errors from smaller time steps are larger than errors from larger time steps. Further analysis showed that the reason for the non-convergence in time comes from the residual numerical diffusion at certain locations which does not vanish to zero as time-step size decreases. This residual numerical diffusion comes from the flux-limiting step of FCT and it is introduced into the solution where there is monotonicity change in the local solution profile. The errors from smaller time steps, however, are not expected to be an issue because larger time steps are preferable when using BICFCT to take advantage of its computational efficiency for low-Mach-number flows.

Second, flow in a 2D enclosed cavity with a moving upper wall was simulated using different time-step sizes. This case was used to assess the ability of BIC on solving steady-state, swirling flows. The solutions showed that a CFL_{wave} number as large as 100 can be used and show good agreement with prior calculations.

The third test problem was the the evolution of two shear layers into vorticies within a 2D, periodic domain. This problem examined the effects of the filter, varying CFL_{wave}, and changing grid size. The comparison of filtered and non-filtered solutions showed that the new filter used in this work can effectively prevent spurious oscillations that may arise in the solution. The tests with varying CFL_{wave} show that BIC is accurate and robust for CFL_{wave} near the explicit stability limit to hundreds of times larger. The solution from BIC for all cases showed good agreement

with solutions from other algorithms, showing that BIC is able to compute transient flows with strong vorticity gradients.

The final test problem simulated 3D vortex breakdown with inflow and outflow boundary conditions, testing the ability of BIC-FCT to predict instabilities that occur in swirling jet flows. Four implicit BIC calculations were performed, each using a different CFL_{wave} from 0.8 to 60. All the modes of vortex breakdown predicted by each of the implicit cases with different CFL_{wave} agreed closely with the modes predicted by explicit FCT, in terms of both structure and location. The calculations showed that BIC was able to predict the bubble mode, the downstream spiral mode, and the double-helix mode. Direct comparisons of the implicit and explicit calculations were made using the same CFL_{wave}. The results show a phase difference in the rotational motion of the downstream double helix. Further analysis of the pressure waves showed that differences in the flow occurred after the initial pressure wave reached the outflow boundary. This difference led to the phase difference of the double helix and it comes from how BIC and explicit FCT handle the outflow boundary differently.

All the test problems showed that the new BIC algorithm is able to efficiently and accurately compute a variety of swirling, low-Mach-number flows with time-step sizes that are hundreds of times larger than the explicit limit. The algorithm presented here could be used for the simulation of other low-Mach-number flows, especially when transient features are of interest.

7.2 Vortex Breakdown Undergoing Heat Addition and Extraction

Vortex breakdown subject to heat addition and extraction was studied using this new BIC algorithm. Two cases with heat addition were investigated, with each case applying a different amount of heat addition to a baseline flow. The baseline flow developed a bubble mode of breakdown with a double-helix mode downstream before the heat addition was applied. Similarly, two cases with heat extraction were investigated, with each case applying a different amount of heat extraction to a baseline flow. The baseline flow for the heat extraction cases had developed a bubble mode of breakdown with a columnar vortex downstream before heat extraction was applied.

In both heat addition cases, the size of the bubble increased and the width of the double-helix decreased compared to the baseline flow. In the case with the larger rate of heat addition, the double helix transitioned to a columnar vortex. In both heat extraction cases, the bubble decreased in size compared to the baseline flow. In the case with the lower rate of heat extraction, the initial columnar vortex downstream of the bubble developed a precessing motion and transitioned to the spiral mode of breakdown. The spiral mode then eventually transitioned to the double-helix mode. In the case with the larger rate of heat extraction, the columnar vortex transitioned directly to the double-helix mode, bypassing the spiral mode.

The cause of the mode transitions in the heat addition and extraction cases was investigated by isolating the effects of the viscosity changes and the density gradients due to temperature changes. This was done by recomputing the cases

described above, except with the temperature dependence of the viscosity turned off. The results showed that the primary cause was the density gradients formed by the heat inputs and that the changes in viscosity had minimal influence on the final states of the transitions. The change in viscosity due to the temperature change can, however, promote the transition process.

7.3 Summary of Key Contributions

The key contributions of this work are summarized below.

- Developed a new, stable algorithm to compute low-Mach-number flows with physical diffusion processes.
  - Identified the root cause of instability in FCT when implemented in 3D. This instability was caused by excessive amount of numerical diffusion in the low-order fluxes. Repaired this instability by reducing the numerical diffusion and changing the high-order fluxes to maintain the accuracy of the original algorithm.
  - Modified the solution procedure for BIC to increase its stability and clarified when and how to update the solution variables during the integration process with physical diffusion processes.
  - Introduced a new filtering procedure which passes the solution variables through the FCT algorithm with no pressure gradients and convection, effectively adding numerical diffusion to cells which have spurious oscillations.

  - Demonstrated that the new BIC algorithm is stable with time-step sizes that are hundreds of times larger than the explicit stability limit. This was done by computing a series of test problems that showed BIC can accurately compute multidimensional, swirling flows.

- Studied how heat addition and extraction affects the modes of vortex breakdown.

  - Demonstrated that a simplified, numerical configuration where the modes of vortex breakdown are determined by just two parameters, Reynolds number and swirl number, can be used for a fundamental study on how heat addition and extraction can affect vortex breakdown.

  - Showed that heat addition suppresses the double helix mode of vortex breakdown while heat extraction can enhance the double helix and spiral modes.

  - This study showed that the response of vortex breakdown to changes in heat input is primarily driven by the formation of density gradients.

  - The computations in this work show that viscosity changes arising from changes in temperature are not the dominant effect causing the vortex breakdown mode transitions. Viscosity changes can, however, promote the transitions.

7.4 Recommendations for Future Work

This work has demonstrated the ability of BIC and FCT to provide stable and robust calculations in the range of low-Mach-number flows. The algorithm has been tested on flows with Mach number as low as 0.003. As the Mach number increases, acoustic waves can become significant and must be considered in the algorithm design. One advantage of the BIC algorithm is that it can either preserve or dampen acoustic waves in the solution by varying the implicitness parameter ω from 0.5 to 1. When its value is 0.5, BIC maximizes the preservation of acoustic waves. When the value is 1, BIC maximizes the damping. In this work, the parameter ω was fixed with a value of 1 and its effect on the solution was not investigated. Therefore, to explore the possibility of using BIC for low-Mach-number *and* high-Mach-number calculations, this work recommends exploring different values of ω in future work. Many of the test problems shown in this thesis could be repeated with difference values of ω, along with different test problems which are sensitive to acoustic waves.

The BIC algorithm in this paper is derived for ideal gases. Future work should consider other types of equation of state for non-ideal gasses. To do this, the pressure correction equation should be re-derived by finding the corresponding relation of changes of pressure and energy, and then substituting the relation into the implicit forms of the conservation of momentum and energy equations. This derivation should follow the original procedure in [20].

This work has shown how vortex breakdown responds when heat is added or extracted to the flow in the downstream portion of the bubble region of breakdown.

In swirl combustors and other reactive swirling flows, heat changes can occur at the upstream portion of the bubble, or perhaps even at other locations away from the bubble. Therefore, future work should use the numerical configuration described in this thesis and apply the heat addition or extraction to different locations to better understand how vortex breakdown will respond.

This work recommends that future studies explore adding or extracting heat from different baseline flows which have developed modes of breakdown different from the ones shown here. Some examples might be to add or extract heat to a flow with a spiral mode or a cone mode.

Bibliography

[1] X. Zhang, J. D. Chung, C. R. Kaplan, and E. S. Oran, "The barely implicit correction algorithm for low-Mach-number flows," *Computers & Fluids*, vol. 175, pp. 230–245, 2018.

[2] X. Zhang, J. D. Chung, C. R. Kaplan, and E. S. Oran, "A comparison of implicit and explicit simulations of vortex breakdown," in *AIAA Scitech 2019 Forum*, p. 1144, 2019.

[3] J. D. Chung, *Numerical Simulation of the Blue Whirl: A Reacting Vortex Breakdown Phenomenon*. PhD thesis, 2019.

[4] H. Xiao, M. J. Gollner, and E. S. Oran, "From fire whirls to blue whirls and combustion with reduced pollution," *Proceedings of the National Academy of Sciences*, vol. 113, no. 34, pp. 9457–9462, 2016.

[5] A. Tohidi, M. J. Gollner, and H. Xiao, "Fire whirls," *Annual Review of Fluid Mechanics*, vol. 50, pp. 187–213, 2018.

[6] R. I. Emori and K. Saito, "Model experiment of hazardous forest fire whirl," *Fire Technology*, vol. 18, no. 4, pp. 319–327, 1982.

[7] J. Lei, N. Liu, and K. Satoh, "Buoyant pool fires under imposed circulations before the formation of fire whirls," *Proceedings of the Combustion Institute*, vol. 35, no. 3, pp. 2503–2510, 2015.

[8] S. Soma and K. Saito, "Reconstruction of fire whirls using scale models," *Combustion and Flame*, vol. 86, no. 3, pp. 269–284, 1991.

[9] S. B. Hariharan, E. T. Sluder, M. J. Gollner, and E. S. Oran, "Thermal structure of the blue whirl," *Proceedings of the Combustion Institute*, vol. 37, no. 3, pp. 4285–4293, 2019.

[10] R. E. Spall, T. B. Gatski, and C. E. Grosch, "A criterion for vortex breakdown," *The Physics of fluids*, vol. 30, no. 11, pp. 3434–3440, 1987.

[11] M. Day, S. Tachibana, J. Bell, M. Lijewski, V. Beckner, and R. K. Cheng, "A combined computational and experimental characterization of lean premixed turbulent low swirl laboratory flames: I. methane flames," *Combustion and Flame*, vol. 159, no. 1, pp. 275–290, 2012.

[12] A. K. Gupta, D. G. Lilley, and N. Syred, "Swirl flows," *Tunbridge Wells, Kent, England, Abacus Press, 1984, 488 p.*, 1984.

[13] N. Syred and J. Beer, "Combustion in swirling flows: a review," *Combustion and flame*, vol. 23, no. 2, pp. 143–201, 1974.

[14] L. Rayleigh, "The explanation of certain acoustical phenomena," *Roy. Inst. Proc.*, vol. 8, pp. 536–542, 1878.

[15] N. Syred, "A review of oscillation mechanisms and the role of the precessing vortex core (pvc) in swirl combustion systems," *Progress in Energy and Combustion Science*, vol. 32, no. 2, pp. 93–161, 2006.

[16] C. Duwig and L. Fuchs, "Large eddy simulation of vortex breakdown/flame interaction," *Physics of Fluids*, vol. 19, no. 7, p. 075103, 2007.

[17] J. P. Boris and D. L. Book, "Flux-corrected transport. i. SHASTA, a fluid transport algorithm that works," *Journal of computational physics*, vol. 11, no. 1, pp. 38–69, 1973.

[18] S. T. Zalesak, "Fully multidimensional flux-corrected transport algorithms for fluids," *Journal of computational physics*, vol. 31, no. 3, pp. 335–362, 1979.

[19] C. R. DeVore, "An improved limiter for multidimensional flux-corrected transport," tech. rep., NAVAL RESEARCH LAB WASHINGTON DC, 1998.

[20] G. Patnaik, R. Guirguis, J. Boris, and E. Oran, "A barely implicit correction for flux-corrected transport," *Journal of Computational Physics*, vol. 71, no. 1, pp. 1–20, 1987.

[21] G. Patnaik, K. Kailasanath, E. Oran, and K. Laskey, "Detailed numerical simulations of cellular flames," in *Symposium (International) on Combustion*, vol. 22, pp. 1517–1526, Elsevier, 1989.

[22] C. R. Kaplan, C. R. Shaddix, and K. C. Smyth, "Computations of enhanced soot production in time-varying CH4/air diffusion flames," *Combustion and Flame*, vol. 106, no. 4, pp. 392IN3399–398IN4405, 1996.

[23] G. Patnaik, K. Laskey, K. Kailasanath, E. Oran, and T. Brun, "FLIC - A detailed, two-dimensional flame model," *NRL Memorandum report*, vol. 6555, 1989.

[24] U. Ghia, K. N. Ghia, and C. Shin, "High-Re solutions for incompressible flow using the navier-stokes equations and a multigrid method," *Journal of computational physics*, vol. 48, no. 3, pp. 387–411, 1982.

[25] R. Nourgaliev, T.-N. Dinh, and T. Theofanous, "A pseudocompressibility method for the numerical simulation of incompressible multifluid flows," *International Journal of Multiphase Flow*, vol. 30, no. 7, pp. 901–937, 2004.

[26] M. L. Minion and D. L. Brown, "Performance of under-resolved two-dimensional incompressible flow simulations, II," *Journal of Computational Physics*, vol. 138, no. 2, pp. 734–765, 1997.

[27] M. Ruith, P. Chen, E. Meiburg, and T. Maxworthy, "Three-dimensional vortex breakdown in swirling jets and wakes: Direct numerical simulation," *Journal of Fluid Mechanics*, vol. 486, pp. 331–378, 2003.

[28] W. J. Grabowski and S. Berger, "Solutions of the Navier-Stokes equations for vortex breakdown," *Journal of Fluid Mechanics*, vol. 75, no. 3, pp. 525–544, 1976.

[29] S. B. Hariharan, "The structure of the blue whirl: a soot-free reacting vortex phenomenon," 2017.

[30] S. B. Hariharan, P. M. Anderson, H. Xiao, M. J. Gollner, and E. S. Oran, "The blue whirl: Boundary layer effects, temperature and oh* measurements," *Combustion and Flame*, vol. 203, pp. 352–361, 2019.

[31] Y. Hu, S. B. Hariharan, H. Qi, M. J. Gollner, and E. S. Oran, "Conditions for formation of the blue whirl," *Combustion and Flame*, vol. 205, pp. 147–153, 2019.

[32] W. Coenen, E. J. Kolb, A. L. Sánchez, and F. A. Williams, "Observed dependence of characteristics of liquid-pool fires on swirl magnitude," *Combustion and Flame*, vol. 205, pp. 1–6, 2019.

[33] T. Sarpkaya, "On stationary and travelling vortex breakdowns," *Journal of Fluid Mechanics*, vol. 45, no. 3, pp. 545–559, 1971.

[34] T. Sarpkaya, "Vortex breakdown in swirling conical flows," *AIAA J*, vol. 9, no. 9, pp. 1792–1799, 1971.

[35] P. Billant, J.-M. Chomaz, and P. Huerre, "Experimental study of vortex breakdown in swirling jets," *Journal of Fluid Mechanics*, vol. 376, pp. 183–219, 1998.

[36] J. H. Faler and S. Leibovich, "Disrupted states of vortex flow and vortex breakdown," *The Physics of Fluids*, vol. 20, no. 9, pp. 1385–1400, 1977.

[37] M. Escudier and N. Zehnder, "Vortex-flow regimes," *Journal of Fluid Mechanics*, vol. 115, pp. 105–121, 1982.

[38] C. Brücker, "Study of vortex breakdown by particle tracking velocimetry (ptv)," *Experiments in fluids*, vol. 14, no. 1-2, pp. 133–139, 1993.

[39] S. Leibovich, "The structure of vortex breakdown," *Annual Review of Fluid Mechanics*, vol. 10, no. 1, pp. 221–246, 1978.

[40] D. Peckham and S. Atkinson, *Preliminary results of low speed wind tunnel tests on a gothic wing of aspect ratio 1.0*. HM Stationery Office, 1960.

[41] N. Lambourne, "The bursting of leading-edge vortices-some observations and discussion of the phenomenon.," *ARCR & M.*, vol. 3282, pp. 1–36, 1962.

[42] J. Harvey, "Some observations of the vortex breakdown phenomenon," *Journal of Fluid Mechanics*, vol. 14, no. 4, pp. 585–592, 1962.

[43] T. Sarpkaya, "Effect of the adverse pressure gradient on vortex breakdown," *AIAA Journal*, vol. 12, no. 5, pp. 602–607, 1974.

[44] T. Sarpkaya, "Turbulent vortex breakdown," *Physics of Fluids*, vol. 7, no. 10, pp. 2301–2303, 1995.

[45] M. Escudier, "Observations of the flow produced in a cylindrical container by a rotating endwall," *Experiments in fluids*, vol. 2, no. 4, pp. 189–196, 1984.

[46] S. Farokhi, R. Taghavi, and E. Rice, "Effect of initial swirl distribution on the evolution of a turbulent jet," *AIAA J*, vol. 27, no. 6, pp. 700–706, 1989.

[47] E. Krause, X.-G. Shi, and P.-M. Hartwich, "Computation of leading edge vortices," in *6th Computational Fluid Dynamics Conference Danvers*, p. 1907, 1983.

[48] R. Spall, T. Gatski, and R. Ash, "The structure and dynamics of bubble-type vortex breakdown," in *Proceedings of the Royal Society of London A: Mathematical, Physical and Engineering Sciences*, vol. 429, pp. 613–637, The Royal Society, 1990.

[49] J. H. Faler and S. Leibovich, "An experimental map of the internal structure of a vortex breakdown," *Journal of Fluid Mechanics*, vol. 86, no. 2, pp. 313–335, 1978.

[50] S. Uchida, Y. Nakamura, and M. Ohsawa, "Experiments on the axisymmetric vortex breakdown in a swirling air flow," *Japan Society of Aeronautical Space Sciences Transactions*, vol. 27, pp. 206–216, 1985.

[51] H. Squire, *Analysis of the Vortex Breakdown Phenomenon.* Imperial College of Science and Technology, Aeronautics Department, 1960.

[52] T. B. Benjamin, "Theory of the vortex breakdown phenomenon," *Journal of Fluid Mechanics*, vol. 14, no. 4, pp. 593–629, 1962.

[53] M. Hall, "A new approach to vortex breakdown," in *Proc. Heat Transfer Fluid Mech. Inst*, pp. 319–340, 1967.

[54] I. S. Gartshore, "Recent work in swirling incompressible flow," tech. rep., National Research Council Canada, 1962.

[55] J. Jones, *The Breakdown of Vortices in Separated Flow.* University of Southampton, Department of Aeronautics & Astronautics, 1960.

[56] L. N. Howard and A. Gupta, "On the hydrodynamic and hydromagnetic stability of swirling flows," *Journal of Fluid Mechanics*, vol. 14, no. 3, pp. 463–476, 1962.

[57] S. Leibovich and K. Stewartson, "A sufficient condition for the instability of columnar vortices," *Journal of Fluid Mechanics*, vol. 126, pp. 335–356, 1983.

[58] H. H. Bossel, "Vortex breakdown flowfield," *The Physics of Fluids*, vol. 12, no. 3, pp. 498–508, 1969.

[59] M. Breuer, *Numerische Lösung der navier-Stokes-Gleichungen für dreidimensionale inkompressible instationäre Strömungen zur Simulation des Wirbelaufplatzens.* PhD thesis, Rheinisch-Westfälische Technische Hochschule Aachen, 1991.

[60] M. Hall, "Vortex breakdown," *Annual review of fluid mechanics*, vol. 4, no. 1, pp. 195–218, 1972.

[61] E. Krause, "A contribution to the problem of vortex breakdown," *Computers & fluids*, vol. 13, no. 3, pp. 375–381, 1985.

[62] S. Xungang and S. Xiaowen, "Relation between the quasi-cylindrical approximation and the critical classification for swirling flow," *Acta Mechanica Sinica*, vol. 3, no. 4, pp. 304–314, 1987.

[63] O. Lucca-Negro and T. O'doherty, "Vortex breakdown: a review," *Progress in energy and combustion science*, vol. 27, no. 4, pp. 431–481, 2001.

[64] L. Rayleigh, "On the stability of stratified flow," *Proc R Soc London*, vol. 93, pp. 148–58, 1916.

[65] H. Ludwieg, *Zur Erklärung der Instabilität der über angestellten Deltaflügeln auftretenden freien Wirbelkerne.* Aerodynamische Versuchsanstalt, 1962.

[66] M. Lessen, P. J. Singh, and F. Paillet, "The stability of a trailing line vortex. part 1. inviscid theory," *Journal of Fluid Mechanics*, vol. 63, no. 4, pp. 753–763, 1974.

[67] A. Garg and S. Leibovich, "Spectral characteristics of vortex breakdown flowfields," *The Physics of Fluids*, vol. 22, no. 11, pp. 2053–2064, 1979.

[68] M. Escudier, "Vortex breakdown: observations and explanations," *Progress in Aerospace Sciences*, vol. 25, no. 2, pp. 189–229, 1988.

[69] F. Kiesewetter, M. Konle, and T. Sattelmayer, "Analysis of combustion induced vortex breakdown driven flame flashback in a premix burner with cylindrical mixing zone," *Journal of Engineering for Gas Turbines and Power*, vol. 129, no. 4, pp. 929–936, 2007.

[70] M. Kro¨ ner, J. Fritz, and T. Sattelmayer, "Flashback limits for combustion induced vortex breakdown in a swirl burner," *J. Eng. Gas Turbines Power*, vol. 125, no. 3, pp. 693–700, 2003.

[71] M. Konle and T. Sattelmayer, "Interaction of heat release and vortex breakdown during flame flashback driven by combustion induced vortex breakdown," *Experiments in fluids*, vol. 47, no. 4-5, p. 627, 2009.

[72] K. Oberleithner, S. Terhaar, L. Rukes, and C. Oliver Paschereit, "Why nonuniform density suppresses the precessing vortex core," *Journal of Engineering for Gas Turbines and Power*, vol. 135, no. 12, 2013.

[73] J. Fritz, M. Kro¨ ner, and T. Sattelmayer, "Flashback in a swirl burner with cylindrical premixing zone," *J. Eng. Gas Turbines Power*, vol. 126, no. 2, pp. 276–283, 2004.

[74] F. Kiesewetter, C. Hirsch, J. Fritz, T. Sattelmayer, *et al.*, "Two-dimensional flashback simulation in strongly swirling flows," in *ASME Turbo Expo 2003, collocated with the 2003 International Joint Power Generation Conference*, pp. 293–300, American Society of Mechanical Engineers Digital Collection, 2003.

[75] J. Fritz, M. Kröner, and T. Sattelmayer, "Flashback in a swirl burner with cylindrical premixing zone," in *ASME Turbo Expo 2001: Power for Land, Sea, and Air*, American Society of Mechanical Engineers Digital Collection, 2001.

[76] M. Kröner, T. Sattelmayer, J. Fritz, F. Kiesewetter, and C. Hirsch, "Flame propagation in swirling flowseffect of local extinction on the combustion induced vortex breakdown," *Combustion Science and Technology*, vol. 179, no. 7, pp. 1385–1416, 2007.

[77] E. Fernandes, M. Heitor, and S. Shtork, "An analysis of unsteady highly turbulent swirling flow in a model vortex combustor," *Experiments in Fluids*, vol. 40, no. 2, pp. 177–187, 2006.

[78] Y. Huang and V. Yang, "Dynamics and stability of lean-premixed swirl-stabilized combustion," *Progress in energy and combustion science*, vol. 35, no. 4, pp. 293–364, 2009.

[79] M. Vigueras-Zuñiga, A. Valera-Medina, and N. Syred, "Studies of the precessing vortex core in swirling flows," *Journal of applied research and technology*, vol. 10, no. 5, pp. 755–765, 2012.

[80] T. ODoherty and R. Gardner, "Turbulent length scales in an isothermal swirling flow," in *The 8th Symposium on Fluid Control, Measurement and Visualization*, p. 6, 2005.

[81] Y. Huang and V. Yang, "Effect of swirl on combustion dynamics in a lean-premixed swirl-stabilized combustor," *Proceedings of the Combustion Institute*, vol. 30, no. 2, pp. 1775–1782, 2005.

[82] T. Sengupta and T. Poinsot, *Instabilities of flows: With and without heat transfer and chemical reaction*, vol. 517. Springer Science & Business Media, 2010.

[83] T. Claypole, C. TC, *et al.*, "The precessing vortex core in swirl stabilized combustors," 1980.

[84] B. Guo, T. A. Langrish, and D. F. Fletcher, "Simulation of turbulent swirl flow in an axisymmetric sudden expansion," *AIAA journal*, vol. 39, no. 1, pp. 96–102, 2001.

[85] S. Shtork, N. Vieira, and E. Fernandes, "On the identification of helical instabilities in a reacting swirling flow," *Fuel*, vol. 87, no. 10-11, pp. 2314–2321, 2008.

[86] C. Schneider, A. Dreizler, and J. Janicka, "Fluid dynamical analysis of atmospheric reacting and isothermal swirling flows," *Flow, turbulence and combustion*, vol. 74, no. 1, pp. 103–127, 2005.

[87] S. Terhaar, T. G. Reichel, C. Schrödinger, L. Rukes, C. O. Paschereit, and K. Oberleithner, "Vortex breakdown types and global modes in swirling combustor flows with axial injection," *Journal of Propulsion and Power*, vol. 31, no. 1, pp. 219–229, 2015.

[88] K. Oberleithner, M. Stöhr, S. H. Im, C. M. Arndt, and A. M. Steinberg, "Formation and flame-induced suppression of the precessing vortex core in a swirl combustor: experiments and linear stability analysis," *Combustion and Flame*, vol. 162, no. 8, pp. 3100–3114, 2015.

[89] L. Rukes, M. Sieber, C. O. Paschereit, and K. Oberleithner, "The impact of heating the breakdown bubble on the global mode of a swirling jet: Experiments and linear stability analysis," *Physics of Fluids*, vol. 28, no. 10, p. 104102, 2016.

[90] L. Rukes, M. Sieber, C. O. Paschereit, and K. Oberleithner, "Methods for the extraction and analysis of the global mode in swirling jets undergoing vortex breakdown," in *ASME Turbo Expo 2016: Turbomachinery Technical Conference and Exposition*, American Society of Mechanical Engineers Digital Collection, 2016.

[91] A. Gorbunova, A. Klimov, N. Molevich, I. Moralev, D. Porfiriev, S. Sugak, and I. Zavershinskii, "Precessing vortex core in a swirling wake with heat release," *International Journal of Heat and Fluid Flow*, vol. 59, pp. 100–108, 2016.

[92] M. Vanierschot, M. Percin, and B. van Oudheusden, "Visualization of the structure of vortex breakdown in free swirling jet flow," in *18th international symposium on the application of laser and imaging techniques to fluid mechanics, Lisbon, Portugal*, 2016.

[93] R. W. MacCormack, "A numerical method for solving the equations of compressible viscous flow," *AIAA journal*, vol. 20, no. 9, pp. 1275–1281, 1982.

[94] F. H. Harlow and A. A. Amsden, "Numerical calculation of multiphase fluid flow," *Journal of Computational Physics*, vol. 17, no. 1, pp. 19–52, 1975.

[95] B. A. Fryxell, P. R. Woodward, P. Colella, and K.-H. Winkler, "An implicit-explicit hybrid method for lagrangian hydrodynamics," *Journal of Computational Physics*, vol. 63, no. 2, pp. 283–310, 1986.

[96] H. Yee and A. Harten, "Implicit TVD schemes for hyperbolic conservation laws in curvilinear coordinates," *AIAA journal*, vol. 25, no. 2, pp. 266–274, 1987.

[97] C. Wall, C. D. Pierce, and P. Moin, "A semi-implicit method for resolution of acoustic waves in low Mach number flows," *Journal of Computational Physics*, vol. 181, no. 2, pp. 545–563, 2002.

[98] P. Degond and M. Tang, "All speed scheme for the low Mach number limit of the isentropic Euler equations," *Communications in Computational Physics*, vol. 10, no. 1, pp. 1–31, 2011.

[99] W. W. Jones and J. P. Boris, "Flame and reactive jet studies using a self-consistent two-dimensional hydrocode," *The Journal of Physical Chemistry*, vol. 81, no. 25, pp. 2532–2534, 1977.

[100] R. Rehm and H. Baum, "The equations of motion for thermally driven, buoyant flows," *Journal of Research of the NBS*, vol. 83, pp. 297–308, 1978.

[101] S. Paolucci, *Filtering of Sound from the Navier-Stokes Equations*. Sandia National Laboratories Livermore, CA, 1982.

[102] R. B. Pember, L. H. Howell, J. B. Bell, P. Colella, W. Y. Crutchfield, W. Fiveland, and J. Jessee, "An adaptive projection method for unsteady, low-Mach number combustion," *Combustion Science and Technology*, vol. 140, no. 1-6, pp. 123–168, 1998.

[103] F. Nicoud, "Conservative high-order finite-difference schemes for low-Mach number flows," *Journal of Computational Physics*, vol. 158, no. 1, pp. 71–97, 2000.

[104] B. Thornber, A. Mosedale, D. Drikakis, D. Youngs, and R. J. Williams, "An improved reconstruction method for compressible flows with low Mach number features," *Journal of computational Physics*, vol. 227, no. 10, pp. 4873–4894, 2008.

[105] J. P. Boris, "A fluid transport algorithm that works.," tech. rep., NAVAL RESEARCH LAB WASHINGTON DC, 1971.

[106] J. P. Boris, A. M. Landsberg, E. S. Oran, and J. H. Gardner, "LCPFCT- a flux-corrected transport algorithm for solving generalized continuity equations," tech. rep., NAVAL RESEARCH LAB WASHINGTON DC, 1993.

[107] E. S. Oran and J. P. Boris, *Numerical simulation of reactive flow*. Cambridge University Press, 2005.

[108] J. P. Boris and D. Book, "Solution of continuity equations by the method of flux-corrected transport," in *Methods in computational physics. Advances in research and applications. Vol. 16*, 1976.

[109] V. Casulli and D. Greenspan, "Pressure method for the numerical solution of transient, compressible fluid flows," *International Journal for Numerical Methods in Fluids*, vol. 4, no. 11, pp. 1001–1012, 1984.

[110] J. L. Steger, "Implicit finite-difference simulation of flow about arbitrary two-dimensional geometries," *AiAA Journal*, vol. 16, no. 7, pp. 679–686, 1978.

[111] A. Jameson, W. Schmidt, and E. Turkel, "Numerical solution of the euler equations by finite volume methods using runge kutta time stepping schemes," in *14th fluid and plasma dynamics conference*, p. 1259, 1981.

[112] M. R. Visbal and D. V. Gaitonde, "High-order-accurate methods for complex unsteady subsonic flows," *AIAA journal*, vol. 37, no. 10, pp. 1231–1239, 1999.

[113] D. V. Gaitonde, J. Shang, and J. L. Young, "Practical aspects of higher-order numerical schemes for wave propagation phenomena," *International Journal for Numerical Methods in Engineering*, vol. 45, no. 12, pp. 1849–1869, 1999.

[114] C. Bogey and C. Bailly, "A family of low dispersive and low dissipative explicit schemes for flow and noise computations," *Journal of Computational physics*, vol. 194, no. 1, pp. 194–214, 2004.

[115] F. Falissard, "Genuinely multi-dimensional explicit and implicit generalized shapiro filters for weather forecasting, computational fluid dynamics and aeroacoustics," *Journal of Computational Physics*, vol. 253, pp. 344–367, 2013.

[116] C. R. Kaplan and E. S. Oran, "Nonlinear filtering for low-velocity gaseous microflows," *AIAA journal*, vol. 40, no. 1, pp. 82–90, 2002.

[117] "Boxlib users's guide website."

[118] T. A. AbdelMigid, K. M. Saqr, M. A. Kotb, and A. A. Aboelfarag, "Revisiting the lid-driven cavity flow problem: Review and new steady state benchmarking results using GPU accelerated code," *Alexandria Engineering Journal*, vol. 56, no. 1, pp. 123–135, 2017.

[119] J. B. Bell, P. Colella, and H. M. Glaz, "A second-order projection method for the incompressible navier-stokes equations," *Journal of Computational Physics*, vol. 85, no. 2, pp. 257–283, 1989.

[120] C. R. Kaplan, E. Oran, and U. Aggarwal, "Reducing statistical scatter in DSMC solutions of hypersonic ionizing flows," in *46th AIAA Thermophysics Conference*, p. 3843, 2016.

[121] D. L. Book, C. Li, G. Patnaik, and F. F. Grinstein, "Quantifying residual numerical diffusion in flux-corrected transport algorithms," *Journal of scientific computing*, vol. 6, no. 3, pp. 323–343, 1991.

[122] K. Manoharan, S. Hansford, J. OConnor, and S. Hemchandra, "Instability mechanism in a swirl flow combustor: precession of vortex core and influence of density gradient," in *ASME Turbo Expo 2015: Turbine Technical Conference and Exposition*, American Society of Mechanical Engineers Digital Collection, 2015.